Institute of Physics

Polish Academy of Sciences

The investigations of superconducting state properties of selected cuprates and iron chalcogenides, including those intercalated with organic compounds

by

Artem Lynnyk

Phd Thesis Performed in the Division of Physics of Magnetism

Supervisor: Prof. dr hab. Roman Puźniak

Warsaw 2023

Abstract

The determination of superconducting state parameters – the upper critical field H_{c2}, the lower critical field H_{c1}, the irreversibility field H_{irr}, and related coherence length ξ and field penetration depth λ – remains as an extremely important task, since they well enough describe the macroscopic and microscopic properties of superconductors and the limits of materials applicability. In presented thesis the superconducting state properties of copper-based $CuBa_2Ca_3Cu_4O_{10+\delta}$ and iron-based $Li_x(C_2H_8N_2)(Fe_ySe_zS_{1-z})$ systems are studied by means of SQUID magnetometry using both dc and ac measurement technique.

It is established that $CuBa_2Ca_3Cu_4O_{10+\delta}$ synthesized by high-pressure and high-temperature method possesses the upper critical field H_{c2} as high as 91 T at the liquid nitrogen boiling temperature (77 K), meanwhile the irreversibility field of about 21 T at the same temperature pronounces the existence of vortex liquid state over the wide range of fields. There is considered the influence of granularity on the ratio of intragranular and intergranular critical current density. Apart from strongly inhomogeneous nature of the material, its very big zero-temperature H_{c2} and related small zero-temperature ξ of about 186 T and 1.33 nm, respectively, indicate high possible pinning abilities and the efficiency of intentionally introduced point defects.

The $Li_x(C_2H_8N_2)(Fe_ySe_zS_{1-z})$ materials of different stoichiometric ratio obtained within the three approaches of solvothermal method reveals weak crystallinity, big amount of magnetic impurity phases and inhomogeneity of superconducting phase. There is observed the tending to mask screening abilities of the material by magnetic phases presence. That leads to impossibility of dc magnetometry technique utilizing. Uniquely proposed using of ac susceptibility measurements realized in external dc bias field is applied in order to study the $H_{c2}(T)$ phase diagram.

Streszczenie

Wyznaczenie parametrów stanu nadprzewodzącego – górnego pola krytycznego H_{c2}, dolnego pola krytycznego H_{c1}, pola nieodwracalności H_{irr} i związanych z nimi długości koherencji ξ oraz głębokości wnikania pola magnetycznego λ – pozostaje niezwykle ważnym zadaniem, gdyż wystarczająco dobrze opisują one właściwości makroskopowe i mikroskopowe nadprzewodników i granice stosowalności materiałów. W niniejszej pracy badane są właściwości stanu nadprzewodzącego układów na bazie miedzi $CuBa_2Ca_3Cu_4O_{10+\delta}$ i żelaza $Li_x(C_2H_8N_2)(Fe_ySe_zS_{1-z})$ za pomocą magnetometrii SQUIDowej z wykorzystaniem zarówno techniki pomiaru dc jak i ac.

Stwierdzono, że zsyntezowany metodą wysokociśnieniową i wysokotemperaturową układ $CuBa_2Ca_3Cu_4O_{10+\delta}$ posiada górne pole krytyczne H_{c2} sięgające 91 T w temperaturze wrzenia ciekłego azotu (77 K), natomiast pole nieodwracalności około 21 T w tej samej temperaturze wskazuje na istnienie stanu cieczy wirów w szerokim zakresie pól. Rozważany jest wpływ granularności na stosunek gęstości prądu krytycznego wewnątrzziarnowego i międzyziarnowego. Poza silnie niejednorodnym charakterem materiału, jego duże zero-temperaturowe H_{c2} i związana z nim mała zero-temperaturowa ξ, wynoszące odpowiednio około 186 T i 1.33 nm, wskazują na potencjalną zdolność do kotwiczenia wirów i skuteczność celowo wprowadzanych defektów punktowych.

Materiały $Li_x(C_2H_8N_2)(Fe_ySe_zS_{1-z})$ o różnej stechiometrii otrzymane według trzech różnych schematów metody solwotermalnej wykazują słabą krystaliczność, dużą ilość faz domieszek magnetycznych oraz niejednorodność fazy nadprzewodzącej. Obserwuje się tendencję do maskowania właściwości nadprzewodzących materiału przez obecność faz magnetycznych. Prowadzi to do niemożliwości wykorzystania techniki pomiarowej dc. Do badania diagramu fazowego $H_{c2}(T)$ unikatowo proponuje się stosować wykorzystanie pomiarów podatności ac realizowanych w zewnętrznym polu dc.

Acknowledgements

I would like to thank my supervisor, Professor Roman Puźniak, for sharing of his time, knowledge, for guidence and constant support during PhD studies.

I am grateful to:

group of Professor Anna Krzton-Maziopa from Warsaw Technical University, group of Professor Changqing Jin from the Institute of Physics CAS for synthesis of superconducting materials;

Doctor Ryszard Diduszko for express XRD analysis of obtained samples;

my collegues, teachers in fact, from the Division of Magnetism, especially to Professor Andrzej Szewczyk, Doctor Pavlo Aleshkevych, Doctor Tatiana Zajarniuk for the lectures on understanding of experimental techniques and how science works in general.

Special thanks to Professor Henryk Szymczak for the powerful boost during the initial period of time in the IP PAS.

Those who surround me – my family and friends – you inspire me and make me better. Thank You all ☺

Table of contents

List of acronyms

H_{c1} – lower critical field

H_{c2} – upper critical field

H_{irr} – irreversibility field

λ – magnetic field penetration depth

ξ – coherence length

SC – superconducting

HTSCs – high-temperature superconductors

IBSCs – iron-based superconductors

YBaCuO (also in the text is marked as YBCO and Y-123) – $YBa_2Cu_3O_{7-\delta}$ material

BiSrCaCuO (also in the text is marked as BSCCO and Bi-22(n-1)n) – $Bi_2Sr_2Ca_{n-1}Cu_nO_{2n+4+x}$ material

Cu-1234 – $CuBa_2Ca_3Cu_4O_{10+\delta}$ material

GL – Ginzburg-Landau (theory)

BCS – Bardeen-Cooper-Schrieffer (theory)

WHH – Werthamer-Helfand-Hohenberg (theory)

SQUID – Superconducting Quantum Interference Device

dc – direct current

ac – alternative current

ZFC – zero-field cooling

FCC – field-cooled cooling

XRD – X-ray diffraction

SI – international system of units

CGS – centimeter-gram-second system of units

Topic Presentation

The phenomenon of superconductivity is a mystery that puzzled scientists for decades. Its discovery is a story that begins over a century ago in 1911, when Dutch physicist Heike Kamerlingh Onnes revealed that the electrical resistance of mercury (Hg) dropped to zero when cooled to liquid helium temperatures, i.e. lower than 4.2 K (–268.95 ºC) [1]. Firstly the elemental materials but later also some of alloys exhibited same extraordinary feature [2]. It was established the ability of such materials to carry non-attenuating current for long enough time (10^5 – 10^{10} years) [3], i. e. to transfer the energy without dissipation. Besides, being the perfect conductors after cooling below certain temperature, superconductors manifested ideal diamagnetism, i. e. complete expelling of magnetic field from the volume. The effect was called the Meissner-Ochsenfeld effect, named after German physicists, which discovered it in 1933 [4]. In fact, the above written meant the attaining of absolutely new and specific thermodynamic state.

As soon as the family of superconductors was filled with newbies quite fast, there happened the necessity of elucidation of the phenomenon as well as of determining of superconducting state parameters. In the next three decades several theories, which tried to describe the superconducting state, appeared. They were developed by utilizing totally different approaches: electrodynamic London's theory (1935) [5], macroscopic Ginzburg-Landau theory (1950) [6], microscopic Bardeen-Cooper-Schrieffer theory (1957) [7]. Those theories were supposed as the basic ones, which well enough explained the behavior of the main thermodynamic parameters of superconducting state: transition temperature T_c, lower H_{c1} and upper H_{c2} critical fields as well as the critical current density J_c of very first discovered superconductors, which were considered as conventional, i.e. in which electron pairing was mediated by electron-phonon interaction [8]. Basically, abovementioned parameters are specifying the phase diagrams of the materials, i.e. the limits of their possible practical utilization.

At those times a common paradigm of new SC materials searching was constructed. Within that framework American physicist Matthias formulated next empirical rules [9]:

- high symmetry is good, cubic symmetry is the best
- high density of electronic states is good
- stay away from oxygen
- stay away from magnetism
- stay away from insulators

– stay away from theorists.

Remarkably, the discoveries which were done within the subsequent years destroyed almost all of them. Only the last is still under debates [10].

In 1986, an era of high-temperature superconductors began, as soon as superconductivity was found in perovskite ceramic – by Bednorz and Müller in La-Ba-Cu-O system with T_c of about 35 K [11] and a half-year later by team of University of Alabama and University of Houston in $YBa_2Cu_3O_{7-\delta}$ (YBaCuO, Y-123) with T_c as high as 93 K [12]. Such a breakthrough showed that copper-based superconductors, or simply cuprates, could operate at much higher temperatures – higher than liquid nitrogen boiling point (77 K) and opened up new opportunities for the practical application of superconductivity, as it was no longer necessary to cool materials to near absolute zero temperatures. Moreover, the unusual crystal layered structure together with inherent antiferromagnetic properties of undoped cuprates provoked a great interest of physical society to the topic as well as the extensive studies toward the characterization of superconducting ground state and possibility of improvement of superconducting state parameters. As a consequence of intensive investigations a huge bunch of copper-based superconductors was synthesized with T_c up to around 138 K at the ambient pressure conditions (for Tl-doped $HgBa_2Ca_2Cu_3O_{7+\delta}$) [13], [14]. Its worth mentioning that T_c as a parameter of classification of superconductors is quite illustrative itself since it points out the transition to superconducting state, nonetheless equally important are the values of critical fields and critical current density J_c, which also bound the practical utilizing. In case of cuprates there was identified a strong anisotropy of those parameters with regard to direction of crystallographic axes, which with the requirement for real conductors to be polycrystalline put the additional limitations on their usage [15], [16]. A set of different synthesis techniques were implemented to improve properties of SC state of cuprates.

Quite outstanding here seems high-pressure synthesized $CuBa_2Ca_3Cu_4O_{10+\delta}$ (Cu-1234). Previously, for Cu-1234 system there was established T_c of about 116 K and J_c of the order of 10^4 A/m^2 at 77 K – which is comparably to YBaCuO and $Bi_2Sr_2Ca_{n-1}Cu_nO_{2n+4+x}$ (BiSrCaCuO, Bi-22(n-1)n) materials and rather advantageous from the anisotropy perspective with regards to Hg-based cuprates [17]–[19]. However, the structural inhomogeneities considering remains highly important, as far as their influence on SC state properties seems undoubted.

Twenty years after the cuprates discovering, in 2006, the investigations of well-known at that point of time oxypnictide LaOFeP [20] resulted in the revealing of brand new family of superconductors – iron-based, by Hosono group [21]. Later, superconductivity with T_c of

about 26 K was detected in $LaFeAsO_{1-x}F_x$ [22]. It's worth noting that new branch of HTSCs possessed similar to cuprates layered structure as well as the presence of magnetic ordering [23], [24]. For now, the highest T_c among the plenty of iron-based superconductors were obtained for bulk $SmO_{1-x}F_xFeAs$ (55 K) and monolayered FeSe on $SrTiO_3$ substrate (65 K) [25]. There was defined unambiguous correlation between superconducting state parameters and crystal lattice regularity in iron-based superconductors (IBSCs) [26]–[28], which among others can be mediated by chemical composition as well [29]–[32]. The idea of chemical modification led to appearing of alkali metal – organic molecules intercalated iron chalcogenide materials: $A_x(O)(Fe_{2-z}Se_2)$, where A – alkali metal, O – organic molecules [33], [34]. Being the rightful heir of $A_xFe_{2-y}Se_2$ 122-group ideologically, the organic intercalated one has T_c of the order of 40–45 K depending on synthesis technique and type of intercalant. The essential peculiarity of $A_x(O)$ intercalated iron selenides is the magnetic inhomogeneities presence. Besides, the volatility of organic molecules introduces the instability of whole compound. Those facts make the exploring of superconducting properties quite challenging.

The investigations aiming at superconducting state parameters defining and corresponding phase diagrams constructing were conducted with the regard to copper-based $CuBa_2Ca_3Cu_4O_{10+\delta}$ and iron-based $Li_x(C_2H_8N_2)(Fe_ySe_zS_{1-z})$ systems ($C_2H_8N_2$ – ethylenediamine). Besides, the scope of the dissertation embraces overview of applied synthesis techniques, determining of explored materials structure, description of utilized methods of thermodynamic parameters defining.

I. Theoretical background: basic concepts and phase diagrams constructing

I.1. *Superconducting state parameters and their determination*

The essence of the superconducting state lays in disappearing of the electric resistance of a material on cooling lower than a certain temperature, which was called critical temperature – T_c. Comparatively to ideal conductors, it was turned out that superconductors exhibit also perfect diamagnetism, which is explained by expelling of magnetic field from the interior of a material – Meissner effect (fig. 1.1). In terms of physical values that means the equality to zero of magnetic field $\boldsymbol{B}$ (*thereafter vector physical values in the equations, where it is important to emphasize, are depicted by bold italic font*).

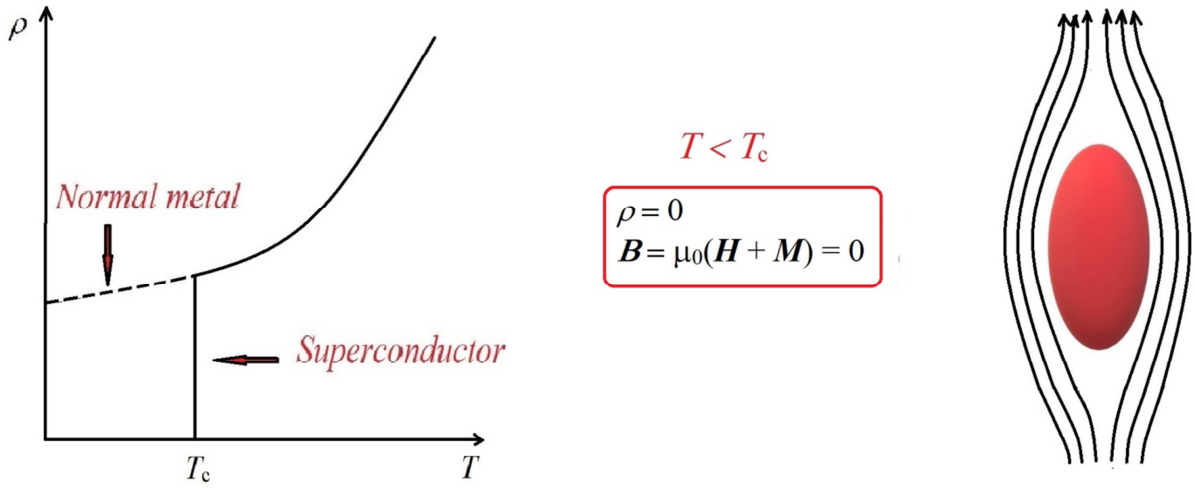

Figure 1.1. The processes, which are accompanying the superconducting state appearance: left side graph – electric resistance behavior, right side image – Meissner effect. The values inside the red frame: ρ – electric resistance, $\boldsymbol{B}$, $\boldsymbol{H}$ – magnetic field, $\boldsymbol{M}$ – magnetization, μ_0 – vacuum permeability.

Concurrently, there was established the vulnerability of superconductivity to influence of external magnetic field. The exposure of „too high" magnetic field, which is called critical field H_c, completely destroys the superconducting state. Thermodynamically, that leads to difference between the free energy densities of normal and superconducting states [3]:

$$F_n(T) - F_s(T) = (\mu_0 H_c^2)/2. \qquad (1.1)$$

Remarkably, thermodynamic critical field H_c depends on temperature and obeys the parabolic law dependence:

$$H_c(T) \approx H_c(0)[1 - (T/T_c)^2]. \quad (1.2)$$

Above written concerns those materials, which exhibit simultaneous occurrence of infinite conductivity and Meissner effect presence – for now known as type I superconductors. Nevertheless, the investigations of Shubnikov's group in the second half of 1930th revealed, that some of materials turned out to have two critical fields: lower H_{c1} – below which superconductors behave as regular type I, upper H_{c2} – above which superconductors fully transform into normal metal. Such superconductors are known as type II superconductors. Phase diagrams of both types of superconductors are shown on fig. 1.2(a, b). The region between $H_{c1}(T)$ and $H_{c2}(T)$ (fig. 1.2b) no longer fulfills the conditions of both perfect diamagnetism and ideal conductivity and later was called the mixed state.

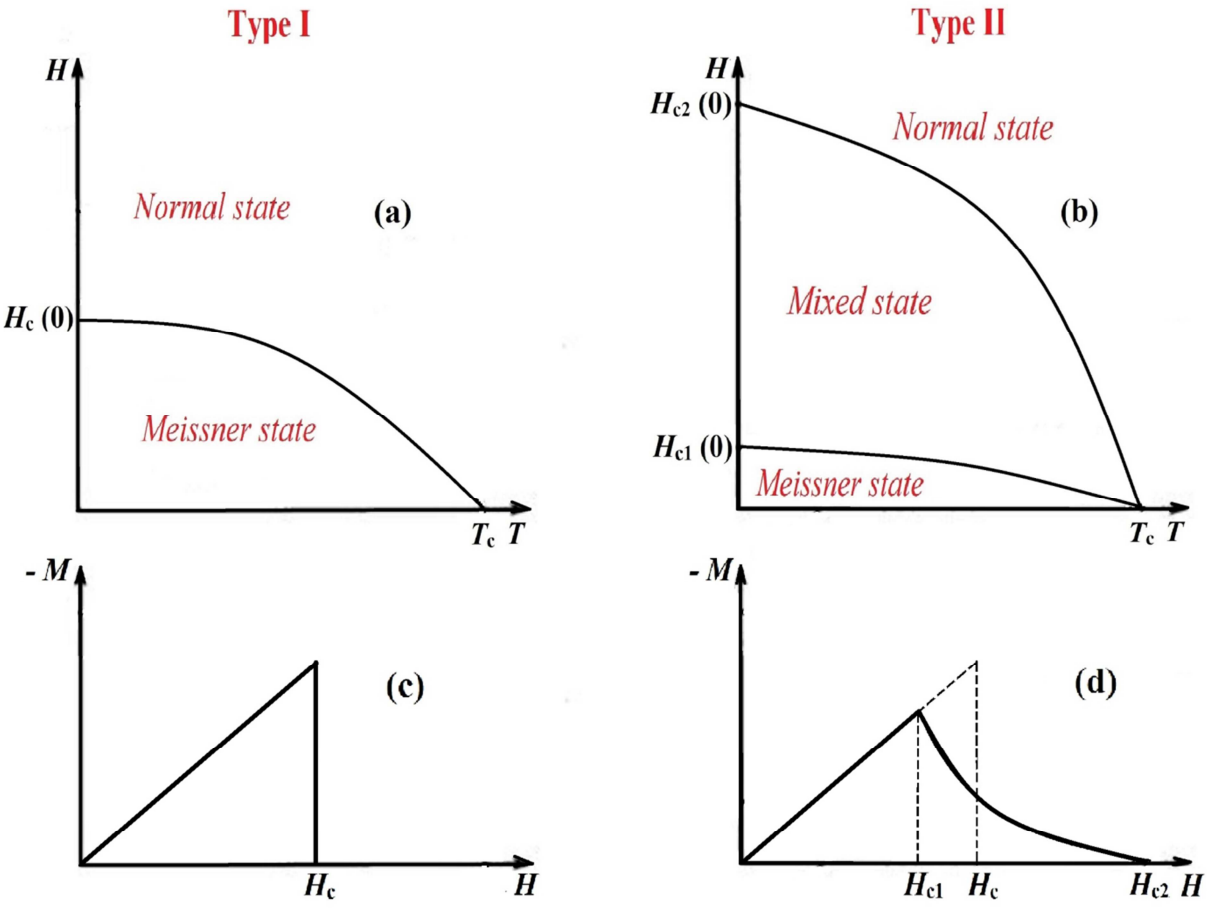

Figure 1.2. Schematic representation of phase diagrams – (a), (b) and magnetization dependences – (c), (d) with regard to type of superconductors: (a), (c) – type I; (b), (d) – type II.

Synchronically, the magnetization dependence, which is for type I materials linearly proportional to the magnetic field, i.e. $\boldsymbol{M} = -\boldsymbol{H}$, in the Meissner state and abruptly disappears on transition to the normal one, in the case of type II decisively deviates from the straight line in the fields, lower than thermodynamic critical field H_c, further steadily approaches the field axis (fig. 1.2(c,d)). While the point of deviation of magnetization from the straight line complies with reaching of H_{c1} field, crossing of the field axis corresponds to H_{c2} field reaching and superconducting state destroying.

Electrodynamic approach of London brothers' gave the general vision on the description of Meissner state existence. It was proposed to use next equations:

$$\boldsymbol{E} = -\frac{\partial}{\partial t}(\Lambda \boldsymbol{j_s}), \tag{1.3}$$

(***E*** *– non-local electric field,* $\boldsymbol{j_s}$ *– density of supercurrent*),

$$\boldsymbol{B} = -\nabla \times (\Lambda \boldsymbol{j_s}), \tag{1.4}$$

(***B*** *– local magnetic field*),

where phenomenological parameter $\Lambda = \mu_0 \lambda_L^2 = m^*/n_s q^2$ (μ_0 – *vacuum permeability*, m^* – *effective mass of superconducting carriers, q – charge of superconducting carriers,* n_s – *density of superconducting carriers*).

In fact, it was postulated the proportionality of a supercurrent density to magnetic vector potential ***A***:

$$\boldsymbol{j_s} = -\boldsymbol{A}/\Lambda, \tag{1.5}$$

since both (1.3) and (1.4) can be obtained either by differentiation of (1.5) in the case of (1.3) or by applying operator *curl* in the case of (1.4). Meanwhile (1.3) expresses the non-dissipative nature of considered system, (1.4) by combining with Maxwell equation in occurrence of stationary distribution of currents and charges – $\nabla \times \boldsymbol{B} = \mu_0 \boldsymbol{J}$ – yields in:

$$\nabla^2 \boldsymbol{B} = \boldsymbol{B}/\lambda_L^2 . \tag{1.6}$$

The solution of (1.6) has the form of exponentially decreasing function: $B_z(x) = B_a e^{-x/\lambda_L}$ (B_a – applied external magnetic field, x – coordinate) and describes the diminishing of applied magnetic field inside the material caused by circulation of screening supercurrent within the

near-surface layer. Apparently, parameter λ_L possesses the dimension of length and points out the distance from surface of material where external magnetic field attenuates by e-times. Parameter λ_L is called London penetration depth and can be expressed as:

$$\lambda_L = \sqrt{m^*/\mu_0 n_s q^2}. \quad (1.7)$$

Later, Pippard generalized Londons' equations for non-local case by introducing parameter – coherence length ξ_0, which was supposed to be inversely proportional to the transition temperature T_c and depended on type of material. Besides, it defined the least size of wave packet, i. e. the distance where the superconducting charge carriers effectively correlate.

The wave function, which describes the dynamics of superconducting carrier transfer was involved in the macroscopic approach. The macroscopic theory was formalized by Ginzburg and Landau and appeared as an extension of Landau theory of phase transitions. Within that frame the existence of superconducting – normal metal transition should be explained as an ordered – disordered transition, meanwhile the wave function of superconducting charge carriers, which is expressed as a complex function: $\psi(\boldsymbol{r}) = |\psi(\boldsymbol{r})|e^{i\theta(\boldsymbol{r})} = \sqrt{\tilde{n}_s(r)}e^{i\theta(\boldsymbol{r})}$ plays the role of an order parameter. $\tilde{n}_s = n_s/2$ – density of superconducting carriers [35]. Here it is necessary to emphasize, that:

1) $\psi = 0$, if $T > T_c$ – in the normal state;
2) $\psi \neq 0$, if $T < T_c$ – in the superconducting state.

The short representation of the theory can be outlined by means of two equations [6]:

$$(1/2m^*)\,(-i\hbar\nabla - e^*\boldsymbol{A})^2\psi + a(T - T_c)\psi + 2b|\psi|^2\psi = 0, \quad (1.8)$$

(ħ – *Planck constant*, m^* – *effective mass of superconducting carriers*, e^* – *effective charge, coefficients a and b – phenomenological parameters came directly from Landau phase transitions theory*),

$$\boldsymbol{j} = (-i\hbar q/2m^*)(\psi^*\nabla\psi - \psi\nabla\psi^*) - (e^{*2}/m^*)|\psi|^2\boldsymbol{A}. \quad (1.9)$$

The (1.9) claimed the direct relation between the order parameter, vector potential of magnetic field and supercurrent density. Assuming that the order parameter is uniform in terms of space coordinates changing and its magnitudes are small in the vicinity of T_c, two

characteristic values can be estimated – field penetration depth from (1.9) and coherence length from (1.8):

$$\lambda_L(T) = \sqrt{\frac{2b}{\mu_0 a(T_c - T)} \frac{m^*_e}{2e^2}}, \tag{1.10}$$

$$\xi(T) = \sqrt{\frac{\hbar^2}{4m^*_e a(T_c - T)}}, \tag{1.11}$$

(e – *the electron charge,* m^*_e *– the effective mass of electron in the material – practically varies with regard to type of the material*).

Their ratio is called Ginzburg-Landau parameter κ. It apparently doesn't depend on temperature and appears to be strictly material feature:

$$\kappa = \frac{\lambda_L(T)}{\xi(T)} = \frac{m^*_e}{e\hbar} \sqrt{\frac{4b}{\mu_0}}. \tag{1.12}$$

It should be mentioned, that Pippard's and Ginzburg-Landau coherence lengths are equal to each other in case of pure metals, that's why the basic physical sence of $\xi(T)$ is as same as for ξ_0.

Besides, Abrikosov showed that κ values clearly correlate with the type of superconductors:

1) $\kappa < 1/\sqrt{2}$, i. e. $\xi > \sqrt{2}\lambda_L$ – corresponds to type I materials;
2) $\kappa > 1/\sqrt{2}$, i. e. $\xi < \sqrt{2}\lambda_L$ – type II materials.

While the first case provides positive surface energy at the border of normal and superconducting phases, the second one ensures negative surface energy [36]. The content of Shubnikov phase (mixed state) was explained then by means of co-existence of superconducting and normal areas. The last ones are performed by threads of magnetic flux and embraced by supercurrent vortices, which are often called Abrikosov vortices (fig. 1.3).

Each vortex keeps inside a unit of magnetic flux quantum Φ_0, where the magnetic flux quantum $\Phi_0 = h/2e = 2.067 \times 10^{-15}$ T·m^2 ($\Phi_0 = 2.067 \times 10^{-7}$ Gs·cm^2 in CGS system). Along the phase diagram representation mixed state is limited by temperature dependent critical field

lines – lower $H_{c1}(T)$ and upper $H_{c2}(T)$. The GL theory predicts values of critical magnetic fields as [3]:

$$H_{c1} = \frac{\Phi_0}{4\pi\lambda^2}(\ln\kappa + 0.5), \tag{1.13}$$

$$H_{c2} = \frac{\Phi_0}{2\pi\xi^2}. \tag{1.14}$$

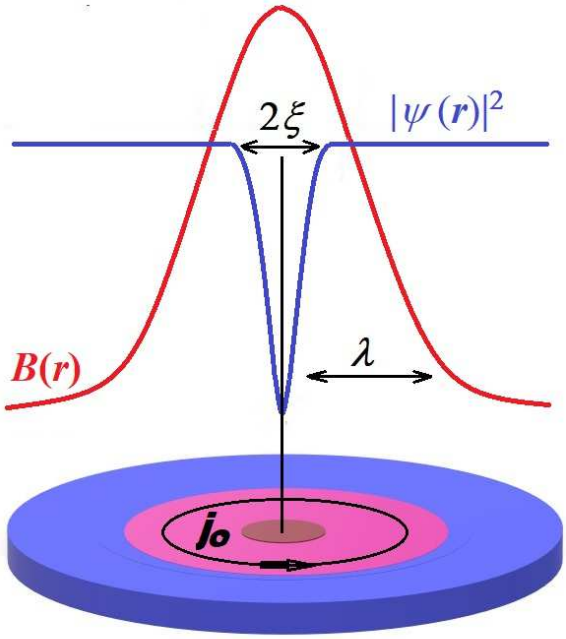

Figure 1.3. Schematic structure of an Abrikosov vortex in cross section view. Blue region corresponds to superconducting area, pink – the area of circulating supercurrents $\boldsymbol{j_o}$ of the size of penetration depth, red – vortex core of 2ξ diameter. $\boldsymbol{B}(\boldsymbol{r})$ – magnetic field, $|\psi(\boldsymbol{r})|^2 = \tilde{n}_s$ – density of superconducting carriers.

Nevertheless, there should be emphasized, that:

1) The GL theory is not a microscopic theory and does not provide any information about the underlying mechanism of superconductivity, but rather gives the vision from thermodynamic point.
2) The theory is only valid near the critical temperature, and its predictions become less accurate as the temperature deviates from the critical temperature.
3) The GL theory assumes that the superconducting state is described by a single complex order parameter, which is not necessarily the case in all superconductors.
4) The theory does not take into account the effects of disorder and impurities, which can have a significant impact on the properties of superconductors.

Proposed by J. Bardeen, L. Cooper and R. Schrieffer in 1957 microscopic approach (BCS theory) describes superconductivity as a result of the formation of Cooper pairs, i.e. the pairs of electrons that are strongly correlated and move in unison through the material [7], [37]. Cooper pairs are bound by an attractive interaction, which is mediated by lattice vibrations (phonons). This interaction leads to a condensation of the Cooper pairs into a single quantum state, known as a Bose-Einstein condensate, and results in the superconducting state. It was established the presence of characteristic energy $\Delta(T)$, which defines the range of wavevectors involved in Cooper pairs formation – energetically preferable only those states, which lay within the range of $\pm\ \Delta$ near the Fermi level E_F. In fact, there was stated the existence of the gap of 2Δ magnitude in electronic spectrum of metals in superconducting state. Another important aspect of the BCS theory is its ability to describe the T_c of a superconductor – it predicts that T_c is proportional to $\Delta(0)$ as: $\Delta(0) = 1.764\ kT_c$ (k – Boltzmann constant). Coherence length in the theory plays role of the space size of Cooper pair and is equaled to: $\xi = \hbar v_F / \Delta(T)$ (v_F – Fermi velocity).

The theory developed by L. P. Gor'kov bounds both microscopic BCS and macroscopic GL approaches by defining the relation between the superconducting energy gap $\Delta(T)$ and the order parameter $\psi(\boldsymbol{r})$ [38]. Besides, Gor'kov extended microscopic approach for critical magnetic fields estimation of pure superconductors of both types [39]–[41]. Later, N. R. Werthamer, E. Helfand and P. C. Hohenberg considered impurity scattering and spin-orbit coupling and used linearized Gor'kov equations for upper critical field estimation [42]–[44]. Along the Werthamer-Helfand-Hohenberg (WHH) theory zero – temperature upper critical field can be calculated as:

$$H_{c2}(0) = -0.726 \frac{dH_{c2}}{dT}|_{T_c} \times T_c \quad (case\ of\ clean-\ limit, i.e.\ \xi \ll\ l-\ mean\ free\ path),$$

$$H_{c2}(0) = -0.693 \frac{dH_{c2}}{dT}|_{T_c} \times T_c \quad (case\ of\ dirty-\ limit, i.e.\ \xi \gg\ l). \qquad (1.15)$$

I.2. *The origin and role of magnetization hysteresis loop*

If we consider arbitrarily massive superconductors under the fields of $H_{c1} < H_a < H_{c2}$, there should be taken into account global penetration of the material by Abrikosov vortices. After getting inside, vortices tend to form regular structures of triangular lattice symmetry (fig. 1.4a) due to intervortex interaction. Nevertheless, flowing through the

superconductor currents can easily move the vortices by the Lorentz force influence, which results in resistive state appearance. Meanwhile, due to interaction with crystal imperfections of the material, e.g. – vacancies, impurities etc., vortices may literally pin to them creating stable distribution of the magnetic field inside the superconductor. That leads to existence of field dependent magnetization hysteresis (fig. 1.4b).

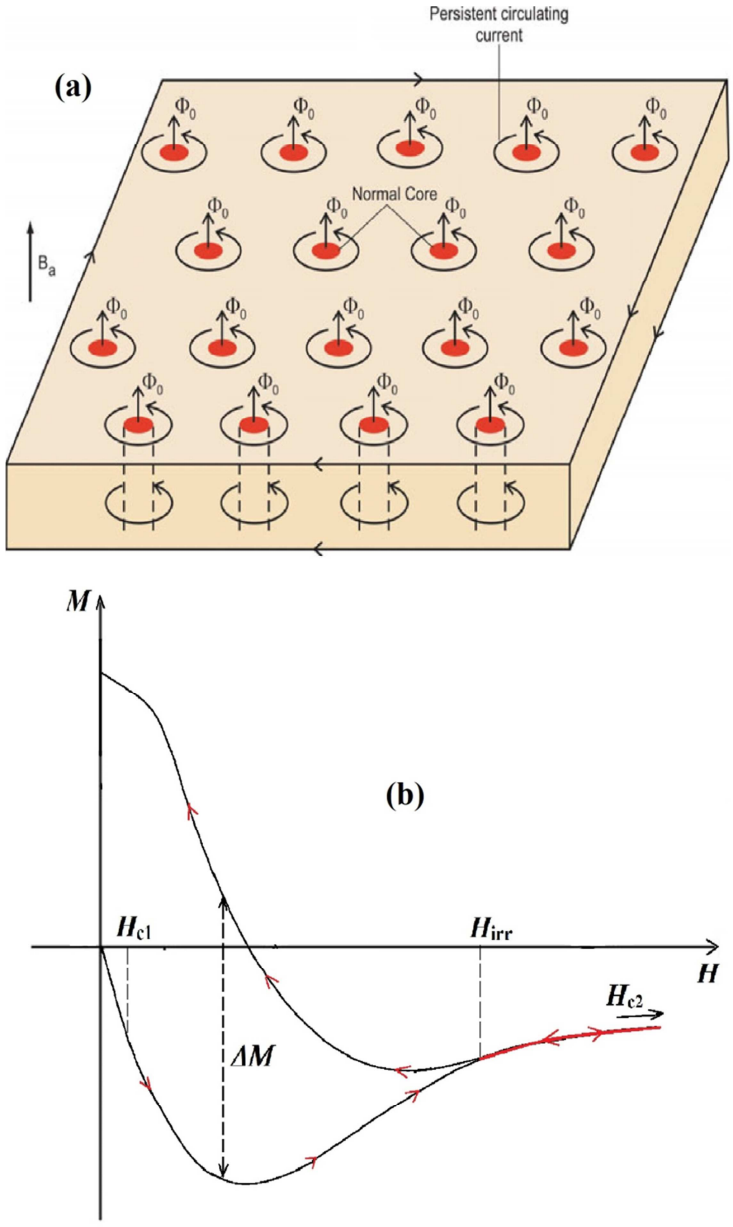

Figure 1.4. (a) – regular arrangement of vortices inside the superconductor; (b) – a half of hysteresis loop, where the magnetization M represented as a function of magnetic field B. ΔM – width of magnetization hysteresis loop. H_{c1}, H_{c2} – lower and upper critical fields, H_{irr} – irreversibility field. Red part of curve depicts the reversible region. Red arrows show the course of magnetization recording. Image (a) was taken from [45]. Reproduced with permission from Springer Nature.

Then, the shape of hysteresis loop strongly correlates with pinning abilities of the material. In turn, as it was mentioned above, the pinning properties influence on the value of critical current, i.e. the current, which can be effectively transferred through the superconductor without turning it into the resistive state. Bean's critical state model [46], [47] revealed the relation between the critical current density j_c and width of magnetization hysteresis loop ΔM as [45]:

$$j_c = \frac{2\Delta M}{d}. \tag{1.16}$$

Since d is a space in the material, which is practically embraced by circulating supercurrent, critical current thus is proportional to the size of structural units, which form a specific sample of the material and hence should be treated as a geometry dependent critical value. Importantly, Bean's model is derived assuming absence of field gradient in magnetized state. Rather applicable in case of more sophisticated systems (e.g. granular materials) is Kim-Anderson approach [48], which considers field-dependent critical current:

$$j_c\,(H_i) = \frac{k}{(H_0 + H_i)}\,, \tag{1.17}$$

(k, H_0 – *constants*, H_i – *internal magnetic field*).

According to (1.16) j_c becomes equal to zero if ΔM disappears, i.e. if the hysteresis loop collapses (fig. 1.4b). Hence, the reversible region corresponds to zero critical current values. Then, the arbitrarily low currents can activate the depinning of vortices, which leads to resistive state appearance [49]. Point (magnetic field), which separates „pinned" and „unpinned" regions is called the irreversibility field H_{irr}. As soon as a shape and a width of hysteresis loop depend on temperature where it's being recorded, H_{irr} can be represented as a function of temperature. There have been developed and practically approved two main approaches for $H_{irr}(T)$:

$$H_{irr}(T) \approx H_{irr}(0)[1 - (T/T_c)]^{\alpha}, \tag{1.18}$$

$$H_{irr}(T) \propto [1 - (T/T_c)^2]^{\alpha}. \tag{1.19}$$

The relation (1.18) was applied initially for superconductive glass state in copper-based material by Bednorz and Müller [50] and later extended for the case of flux creep in general

[51]–[53]. Relation (1.19) was proposed by T. Matsushita [49]. Power α correlates with the anisotropy of carriers' effective masses and hence is a feature of a specific material, e.g. its equal to 1.5 for Y-123 material or 2 for Bi-2212 [54].

The reversible region on fig. 1.4b characterizes unpinned region (already resistive regime of superconductor) and is separated from normal state by H_{c2} field. According to London approach to type II superconductors magnetizing scheme [3]:

$$H \approx B + H_{c1}\left(\ln\frac{H_{c2}}{B}\right)/\ln\kappa. \tag{1.20}$$

Then, by taking into account relation – $B = \mu_0(H+M)$, magnetization can be expressed as [55]:

$$M(H) = -\frac{\Phi_0}{8\pi\mu_0\lambda^2}\left(\ln\frac{\eta H_{c2}}{H}\right), \tag{1.21}$$

(η – *parameter of the order of unity*) [56], [57].

The phase diagram on fig. 1.2b with regard to $H_{irr}(T)$ considering can be schematically redrawn as:

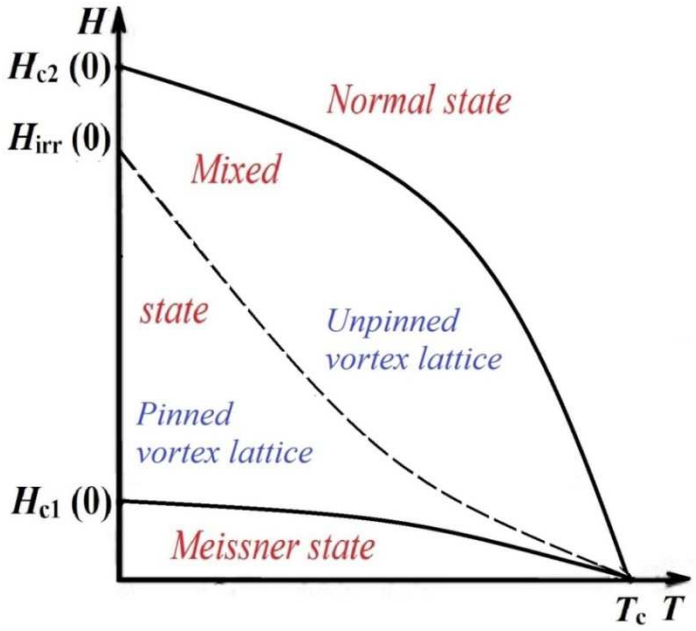

Figure 1.5. Phase diagram of type II superconductor with taking into account different vortex lattice states – pinned and unpinned, which are divided by irreversibility field line $H_{irr}(T)$.

II. Measurement techniques and data analysis

As soon as thermodynamic parameters described above can provide important information about superconducting state of specific material, there should arise a reasonable question: how to determine them? Since fundamental macroscopic SC state properties include special reaction on magnetic field applying as well as the ideal conductivity presence, experimental techniques which can fully describe the SC state are mainly divided on two categories: transport/magnetotransport measurements and magnetization measurements.

II.1. *Transport measurements*

The first category relates to measurements of resistivity as a function of temperature. Classical H. Kamerlingh Onnes experiment on Hg sample is classified exactly to such group. The basic sense of this method lays in recording of current-voltage dependence during temperature sweeping. Technically, it is usually realised within the four-probe configuration. The fall of resistivity to zero values corresponds to transition to SC state occurence. Depending on width of transition, onset of SC state can be defined with regard to temperature axis as a point on $\rho(T)$ curve, where the resistivity starts to fall – T_c^{onset}, if we track the curve from high temperatures to low. Although, there widespread and accepted also to take into account the transition temperature T_c, where the resistivity is equaled to zero already (fig. 2.1). In fact, those points approximately coincide if the transition is sharp and/or if the measurements are performed with low current in the absence of magnetic field. Importantly, the measurements can be conducted at the external magnetic field as well (magnetotransport measurements), which shifts the onset to SC state and smears the width of transition. Pair of temperature and field where the transition emerges corresponds to critical temperature T_c and thermodynamic critical field H_c respectively, if we deal with type I superconductor, or to T_c and upper critical field H_{c2}, if we measure a sample of type II superconductor. However, insofar as the width of transition grows with the increase of applied magnetic field magnitude, different criteria of determination of T_c and corresponding $H_{c2}(T)$ can be used, i.e. at 90%, 50% (midpoint) or 10 % of normal state resistivity on $\rho(T)$ curve or at completely superconducting state [58], [59]. Using the relation (1.14) coherence length $\xi(T)$ can be evaluated then. All described above is related to constant current-voltage technique. Moreover, there is a possibility to evaluate field penetration depth $\lambda(T)$ from impedance spectroscopy measurements. It utilizes alternative current to probe the material, but also lays in a same basket of transport methods. Since $\lambda(T)$ and $\xi(T)$ can be recalculated in lower

critical field (1.13), we obtain complete magnetic phase diagram, which contains both $H_{c1}(T)$ and $H_{c2}(T)$. But undoubtedly, the highest advantage of the transport measurements is an opportunity of direct estimation of critical current density j_c, which outlines practical limitations of applicability of specific superconducting material.

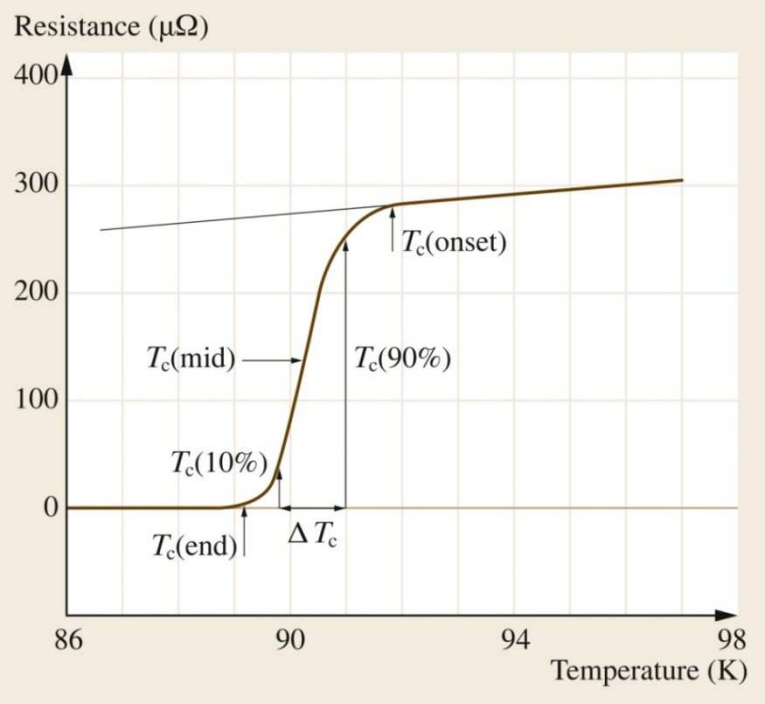

Figure 2.1. The example of different transition temperature definition. The results refer to measurements of $Bi_2Sr_2CaCu_2O_8$/Ag multicore wire. Image was taken from [60]. Reproduced with permission from Springer Nature.

Nonetheless, despite apparent strength and pros of transport measurement approach, there should be admit presence of weak points. One of the main challenges is that resistivity measurements can be affected by a variety of factors, such as sample quality, sample geometry, and contact resistance between the sample and the electrodes. This can make it difficult to obtain accurate and reproducible measurements, particularly for high-temperature superconductors or materials with complex microstructures. Another potential disadvantage of resistivity measurements is that they only provide information about the normal-state electrical properties of the material, rather than the superconducting properties. While resistivity measurements can be used to determine the critical temperature of the material, they may not provide a complete picture of the superconducting behavior of the material, particularly in the presence of magnetic fields or other external perturbations.

II.2 *Magnetization measurements*

To avoid those problems, utilizing of magnetization measurements is preferable. Why is it so? Firstly, those measurements are contactless, i.e. the sample doesn't need to be specially modified with the purpose of surface treatment. That's why samples of arbitrary shape, conditions and microcrystalline structure are fitted for such study. Exceptions are usually related to massive samples and limitations, which are bounded with the geometry of specific measuring device. Secondly, since the magnetization measurements probe the magnetic properties of material, phases below and above the T_c are investigated.

Technically, magnetization measurements are divided on two subclasses: direct current (dc) and alternative current (ac) measurements. Noteworthy, that devices, which are provided studies of the first subclass, measure the dc magnetic moment of specific sample at constant magnetic field. After that, the dc magnetic moment can be recalculated to magnetization during the data processing. In turn, ac measurements are focused on defining of magnetic moment with subsequent recalculation to ac susceptibility by applying alternative field of specific amplitude and frequency. It is the right moment here to remove the ambiguity in utilizing of magnetization/susceptibility units. The problem consists in utilizing of electromagnetic [emu] units for representation of measured dc magnetic moment or ac susceptibility, provided for example by frequently used instruments: MPMS (*Magnetic Property Measurements System*), PPMS (*Physical Property Measurements System*) with VSM or ACMS options, etc. Further calculations of dc magnetization lead to [emu/g] units for mass magnetization or [emu/cm^3] for volume magnetization. Those units are related to CGS system and it is commonly accepted to convert them to SI system, i.e. to [A/m] or [T] units. In the case of ac measurements [emu] of susceptibility are converted to dimensionless values as it is demanded with regard to SI system. Nevertheless, both CGS and SI systems are widespread used in scientific publications and still treated as interchangeable especially in the area of magnetic measurements.

II.2.1. dc regime

Within the dc regime there can be obtained straightforwardly – T_c, $H_{c1}(T)$, $H_{c2}(T)$, derived from corresponding relations – $\lambda(T)$ and $\xi(T)$ or estimated by applying different models of critical state – j_c. In order to identify the transition temperature T_c of the material, magnetic moment is recorded as a function of temperature, usually at non-zero fixed dc magnetic field. Importantly, dependent on structural and magnetic peculiarities of probed

superconducting materials such perturbed dc field has to be small, usually it is taken as high as 10^{-4} – 10^{-2} T (1 – 100 Oe in CGS system). Although a magnitude of applied dc magnetic field should be sufficient to obtain more or less adequate response for sequential processing, it is more favourable not to exceed lower critical field H_{c1}, since it would violate the correctness of estimation of the Meissner phase percentage. Typically, two modes are utilized during the measuring of temperature dependences of magnetic moment – zero-field cooling (ZFC) and field-cooled cooling (FCC). Very often, the last one is called simply field-cooled (FC). The ZFC mode consists in realization of two steps: cooling of the investigated material at zero magnetic field with subsequent recording of magnetic moment at fixed dc field on heating until the desired temperature. In turn, FCC is aiming at the recording of magnetic moment at switched on dc field on cooling. Usually, both ZFC and FCC modes are implemented during one measuring cycle and executed one after another. Generally, superconducting materials without magnetic inclusions are revealed merged ZFC and FCC curves above the T_c and diverged below. Visually, the transition looks like a kink on ZFC-FCC dependence, where the magnetic moment changes a sign, i.e. it becomes diamagnetic and negative if we track the ZFC-FCC from higher temperatures to lower. In the most simple case, T_c is defined from ZFC curve as a point of intersection of linearly extrapolated signal of normal state region and linearly extrapolated slope of superconducting state region (fig. 2.2).

Nevertheless, often it is useful to characterize the transition with onset point T_c^{onset}, especially if we have to deal with mix of superconducting phases or paramagnetic/ferromagnetic inclusions presence. Signal from magnetic inhomogeneities can superimpose on the response from superconducting ground state modifying it. In that case T_c^{onset} is defined as a point of deviation of ZFC temperature dependence from the straight line, Straight line is fitted to points, which are supposed to correspond to normal state region. With regard to bifurcation between ZFC and FCC curve, it qualitatively indicates the presence of flux lines pinning. If we deal with relatively pure superconductor, point of bifurcation lays below the T_c, meanwhile the influence of magnetic inclusions shifts this point to the region above the T_c (fig. 2.3).

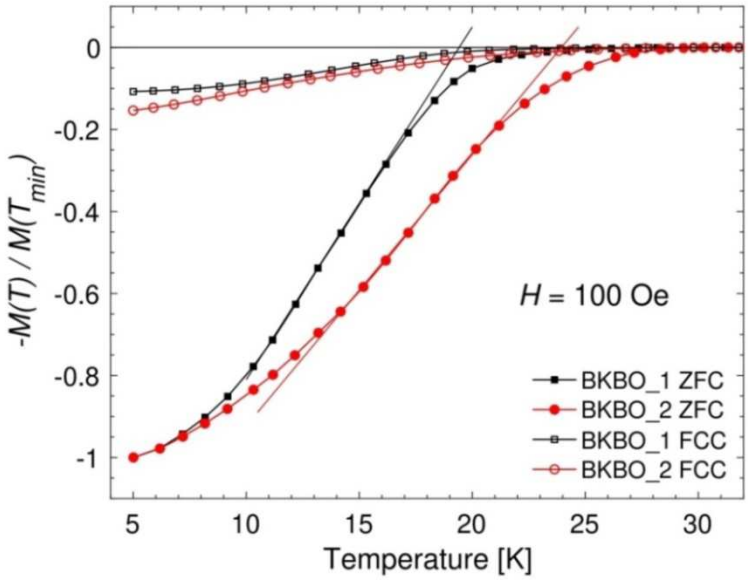

Figure 2.2. The example of transition temperature T_c defining from magnetization measurements of $Ba_{1-x}K_xBiO_3$ superconductor, obtained along ZFC-FCC protocol at fixed dc field of 100 Oe (10 mT in SI units) [61]. The figure was reprinted from: Wojciech R. Pudelko, Anna Krzton-Maziopa, Artem Lynnyk, Roman Puzniak, Krystyna Lawniczak-Jablonska, Dariusz J. Gawryluk, Dorota Moszczynska, Jaroslaw Mizera, „Bismuth and oxygen valencies and superconducting state properties in $Ba_{1-x}K_xBiO_3$ superconductor," *Phys. B Condens. Matter*, vol. 591, p. 412226, Aug. 2020, Copyright 2023, with permission from Elsevier.

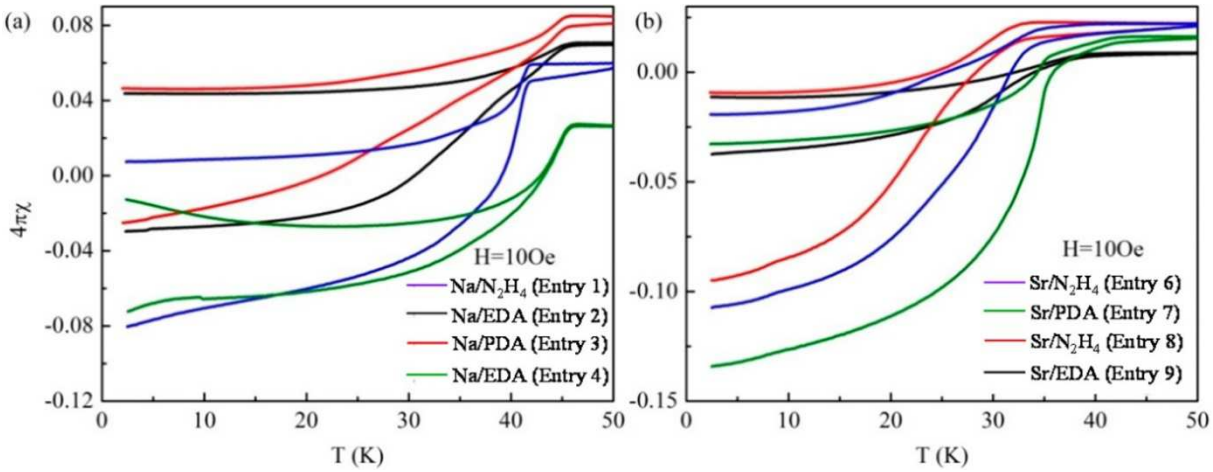

Figure 2.3. The example of broad transitions and developed bifurcation character of ZFC-FCC dependence measured at 10 Oe (1 mT in SI units) of dc field. The results were obtained for metal/organic intercalated systems, based on FeSe matrix. Reprinted (adapted) with permission from [62]. Copyright 2023 American Chemical Society.

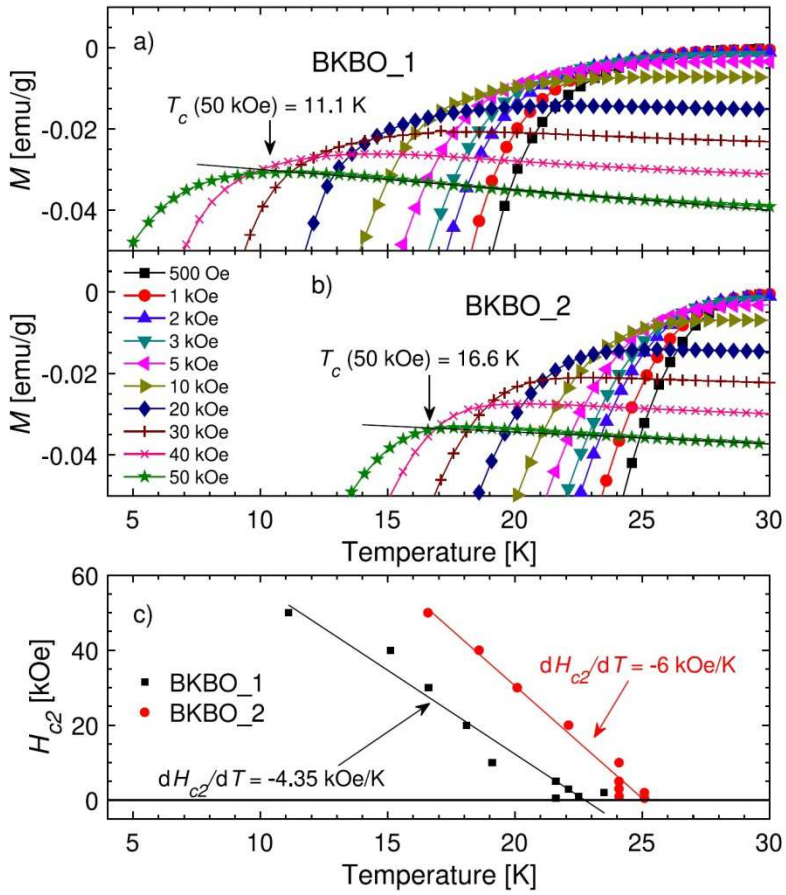

Figure 2.4. The utilizing of temperature dependences of magnetization for upper critical field H_{c2} defining. The results were obtained for $Ba_{1-x}K_xBiO_3$ superconductor and taken from [61]. The figure was reprinted from: Wojciech R. Pudelko, Anna Krzton-Maziopa, Artem Lynnyk, Roman Puzniak, Krystyna Lawniczak Jablonska, Dariusz J. Gawryluk, Dorota Moszczynska, Jaroslaw Mizera, „Bismuth and oxygen valencies and superconducting state properties in $Ba_{1-x}K_xBiO_3$ superconductor," *Phys. B Condens. Matter*, vol. 591, p. 412226, Aug. 2020, Copyright 2023, with permission from Elsevier.

To complete the introduction to analysis of temperature dependences of magnetization, there should be noticed, that the value of magnetization and hence of dc susceptibility on ZFC curve refers to the evolution of shielding fraction content. As a consequence, by comparing measured values of susceptibility below the T_c with the susceptibility of ideal superconductor (equals to –1) percentage of shielding fraction can be calculated. Nevertheless, it is important to verify the validity of obtained results by conducting the correction on demagnetizing field influence.

Besides, since the transition to superconducting state is described by pair of physical values on phase diagram (see fig. 2.4a) – (field, temperature), the value of applied dc magnetic field during ZFC-FCC measurements corresponds to upper critical field H_{c2}. Hence,

set of such pairs forms $H_{c2}(T)$ diagram. Methodologically, several ZFC temperature dependences of magnetization are usually measured. Gradually increased magnetic field leads to shifting of the transition toward the lower temperatures (fig. 2.4b).

Apart from ZFC-FCC temperature dependences analysis, useful information about SC state can be extracted from the isothermal field dependences of magnetization as well. Since the majority of studied superconducting materials relates to type II, which means the existence of magnetization remanence, ZFC measurement protocol typically is applied in order to eliminate the influence of remanence and to provide purity of experiment. Concepts of isothermal magnetization loops analysis allow to estimate $H_{c1}(T)$, $H_{irr}(T)$ and $H_{c2}(T)$ (see sub-section I.2). With respect to H_{c2} determining that is particularly helpful, because of its high-values in the case of widespread copper-based systems. From a technical standpoint, H_{c2} is obtained by considering reversible tails of hysteresis loops as the London approach proposes. The superconducting material reach the H_{c2} at the point where the magnetization loses diamagnetic character, i.e. changes a sign from negative to positive. Hence, H_{c2} at specific temperature can be defined from the dependence $M(\ln H)$, where M – magnetization, H – applied dc external field (fig. 2.5). Moreover, the equation (1.21) points that the slope of $M(\ln H)$ is described with $(-\Phi_0/8\pi\mu_0\lambda^2)$ coefficient, therefore London penetration depth can be evaluated as well. Related ξ and H_{c1} are estimated from Ginzburg-Landau equations (1.13 – 1.14). Typically, $M(\ln H)$ are placed quite far from the field axis, which creates the need of extrapolation utilizing. With regard to applicability of that approach, there should be noticed the presence of uncertainty, which bounds with extrapolation. The example of utilizing of this approach was given here [63], [64].

The irreversibility field H_{irr} corresponds to moment of splitting of the reversible part of $M(H)$. Hence, it can be obtained by calculating difference between ascending and descending branches of $M(H)$, i.e. $\Delta M(H)$. As a consequence, $H_{irr}(T)$ line is unequivocally bounded with disappearance of critical current density, which is calculated within the Bean's critical state model, and experimentally from hysteresis loop width ΔM. That mutual correlation gives the opportunity to estimate H_{irr} from $j_c(H)$ dependences by applying criteria – values of j_c, which control the relevance of obtained H_{irr} values by cutting the $j_c(H)$ dependence at specific points. Such points of intersection of criterion line and $j_c(H)$ indicate the onset of H_{irr} and hence practical validity of applied criterion.

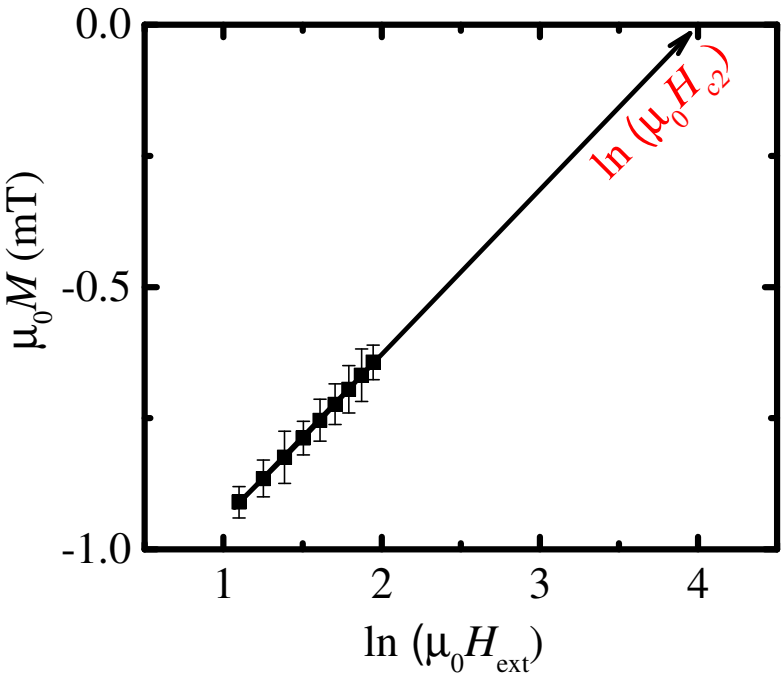

Figure 2.5. Semi-logaritmic dependence of magnetization via external dc field obtained from the reversible region of magnetization hysteresis loop. Parallel to vertical axis black bars indicate the standard error, which is obtained for each of point and dependent on precision of utilized measuring equipment and amount of measurement cycles. The measurements were performed for Cu-1234 material.

Finally, considering $M(H)$ hysteresis loop the initial region of curve with the slope of -1 is responsible for Meissner state. The Meissner state is limited with $H_{c1}(T)$ line on phase diagram and therefore reaching of H_{c1} would transfer the material to the mixed state. The moment of H_{c1} onset is standardly determined as a point on initial $M(H)$ dependence, where the slope starts to decrease in absolute values, which means the deviation of the dependence from the straight line. Obviously, to gather the points for $H_{c1}(T)$ diagram there is a necessity of series of isothermal $M(H)$ initial curves. But the most important task here to catch the point of deviation correctly. There are two main approaches for solution. The first – direct – to fit the points which correspond to perfect diamagnetism with straight line and simply track the curve. The second lays in further processing of obtained curves by applying square root to difference between the $M(H)$ dependence and fitted diamagnetic straight line which results in dependence of scattered $(M_{measured} - M_{dia})^{1/2}$ data via magnetic field. Theoretical baseline and argumentation of feasibility of this approach is given here [65]. It is worth noting, that in both approaches it is supposed to fit the straight line with an ideal slope of -1 for Meissner region. However, there is almost no chance to obtain perfect diamagnetism from raw experimental data, since the shape of specific sample generate an additional

demagnetizing field, that distorts the results. That's why there appears a need of correction for demagnetizing effect. Applied external dc field can be represented as a sum of internal field and demagnetizing field as: $H_{ext} = H_{int} + DM$, where D is a shape-dependent demagnetizing coefficient. Hence, for accurate H_{c1} defining in case of both approaches it is more fair to redraw the results as function of internal field after the subtraction of demagnetizing field.

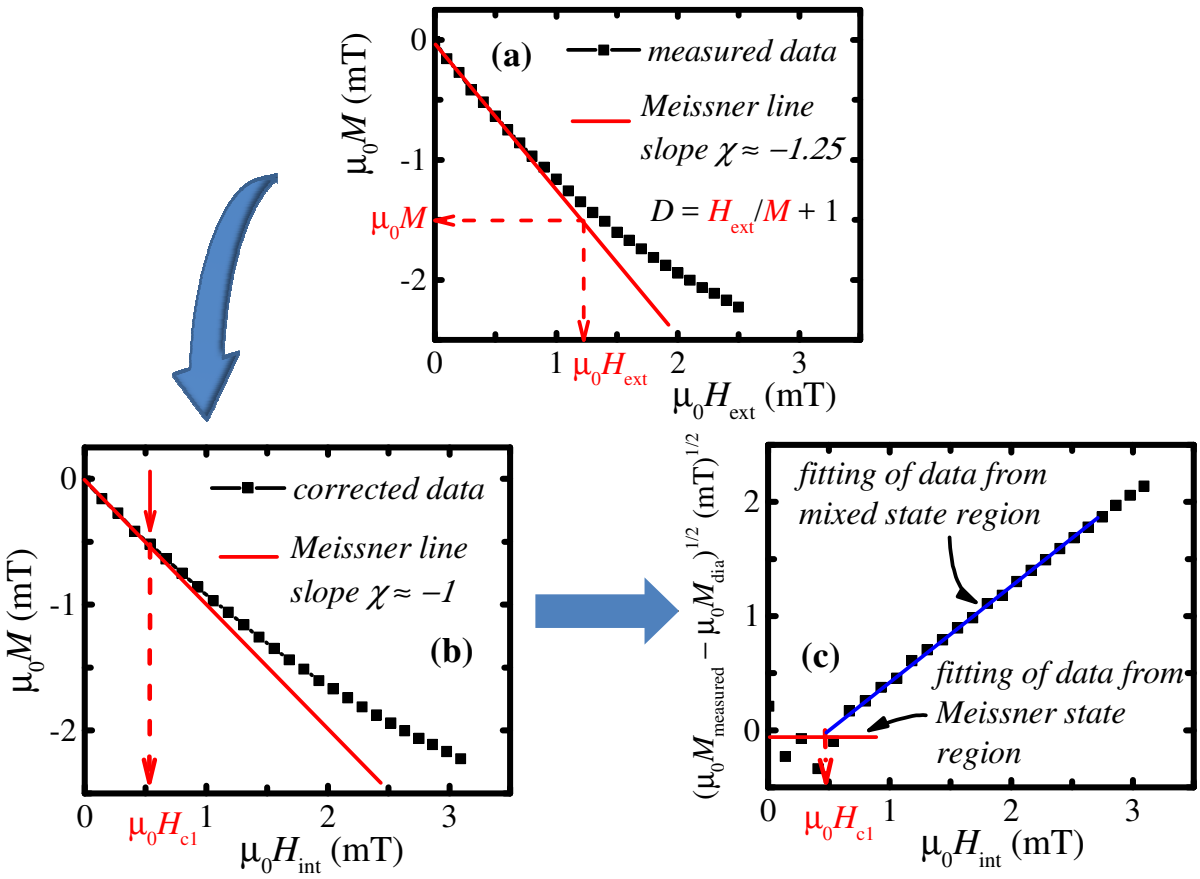

Figure 2.6. Processing of initial magnetization dependence $M(H)$ with the purpose of H_{c1} estimation. (a) Measured magnetization data, represented as a function of applied external dc field H_{ext}, solid red line – Meissner line fitting, dashed red arrows indicate values of M and H_{ext}, which are taken for correction procedure. (b) Magnetization values after correction – redrawn as a function of internal field H_{int}. The validity of correction is confirmed by fixed slope value of Meissner line, which now corresponds to ideal diamagnetism ($\chi = -1$). Point of deviation of magnetization values from straight line indicates the onset of lower critical field H_{c1}. (c) More sophisticated variant of H_{c1} defining, which includes linear approximation of scattered values of magnetization from Meissner region and linearization of bordering mixed state area. The experimental data were obtained for Cu-1234 material.

Often, the experiments are conducted for samples of regular shapes and demagnetizing field is easily calculated – coefficient D is tabulated for different geometries. In the same time, D can be estimated from experimental $M(H_{ext})$ curve directly (fig. 2.6a). That becomes possible by taking into account Meissner effect, formulated on fig. 1 as equality to 0 of magnetic field B inside the superconductor at the ideally diamagnetic state: $B = \mu_0(H + M) = \mu_0(H_{int} + M) = 0$. Then, it can be rewritten as: $\mu_0(H_{ext} - DM + M) = 0$. Finally, demagnetizing coefficient appears: $D = H_{ext}/M + 1$ (μ_0 is reduced). For computations, H_{ext} and M are come from experimental curve immediately as it is shown on fig. 2.6a. After correction procedure obtained values of internal field H_{int} are used for H_{c1} defining. Full scheme of above described is sketched on fig. 2.6 in details.

II.2.2. ac regime

Usually utilized in study of spin relaxation in glassy state, ac susceptibility measurements in turn allows to probe superconducting state as well. The approach helps to built general vision about investigated material from the perspective of vortex lattice dynamic, since it is exposed to alternative field $h_{ac}(t)$ impact. The formalized and slightly simplified representation of ac susceptibility appears as: $\chi_{ac} = \chi' + i\chi''$ [66], where χ' – real (or in-phase), χ'' – imaginary (or out-of-phase) parts. Phase-dependent response from investigated system can be recorded separately for both components. That creates additional advantages in SC materials exploring.

Generally, temperature dependence of real part $\chi'(T)$ resembles the dc $M(T)$ measurements (lower panel on fig. 2.7). The transition to SC state can be clearly seen from $\chi'(T)$ and T_c is defined in the way described for dc measurements. Importantly, ZFC and FCC curves coinside in case of ac susceptibility, which prevents the qualitative estimation of pinning degree. Nevertheless, the technique is quite sensitive for indication of minor phases presence, since the applied ac field can be really small, of the order of 10^{-2} mT (0.1 Oe in CGS). The traces of minor phases usually appear as additional step-like transition below the T_c. Such step-like behavior is also a sign of the existence of weak-links in granular superconductor. Thus, it is necessary to know the origin of investigated sample and syntesis methods, which were applied during the material obtaining.

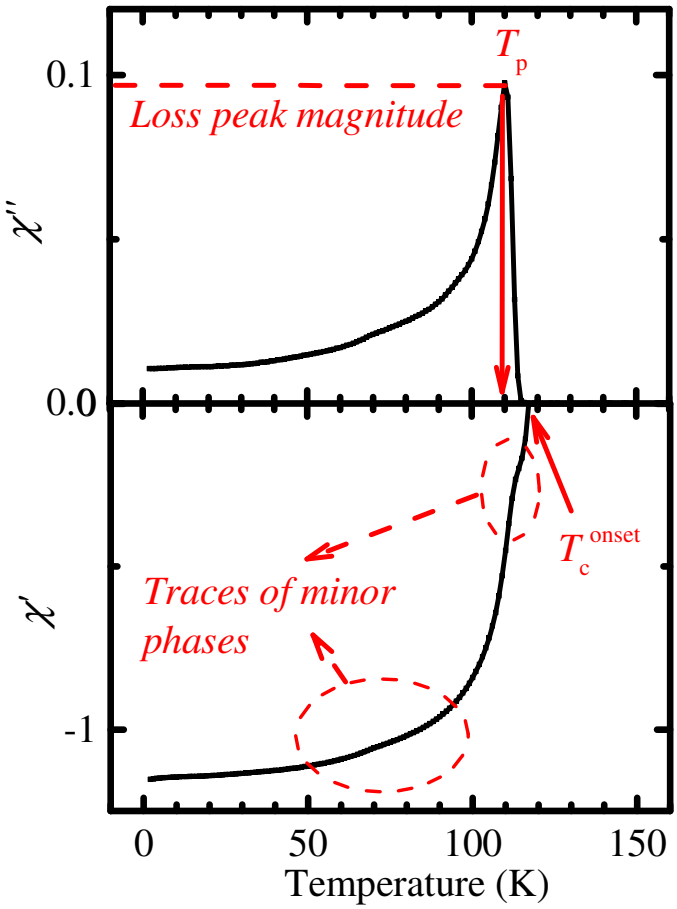

Figure 2.7. Temperature dependences of real $\chi'(T)$ and imaginary $\chi''(T)$ parts of ac susceptibility depicted on lower and upper panels respectively. The example reflects the defining of main parameters T_c^{onset}, temperature of peak position T_p, peak magnitude. The $\chi'(T)$ reveals the value of susceptibility more than –1, since the results weren't corrected for demagnetizing effect. The dependences were recorded for Cu-1234 material.

The imaginary part $\chi''(T)$ (upper panel on fig. 2.7) is recorded concurrently with $\chi'(T)$ and points the degree of energy dissipation in the material during the measurement cycle. Unlike to $\chi'(T)$, $\chi''(T)$ reveals peak behavior. Loss peak is characterized by the position (peak temperature T_p), width and magnitude. It is usually placed below the T_c and can move along the temperature axis with regard to variation of frequency f and amplitude of applied ac field H_{ac}. The occurrence of frequency dependent loss peak position is connected with flux creep process and indicates the activation of vortices movement – the process also known as *thermally activated flux creep* [67]–[69]. Besides, there are techniques, which allow to estimate critical current density j_c of granular material from the relation of T_p via H_{ac} by using critical state models [70]. The width and magnitude of loss peak correlate with ac field amplitude. Moreover, the presence of minor phases as well as the granularity of explored

material often split the loss peak such as double peak or two separate loss peaks may appear [71], [72]. Qualitatively, the ratio of their magnitudes points out the contribution of each subsystem to dissipation process.

Similarly to dc option, the ac susceptibility technique allows to obtain $H_{c2}(T)$ phase diagram. That is highly important if we have to deal with superconductors, which contain certain amount of magnetic inclusions, e.g. iron-based materials. The magnetic inhomogeneities are capable to mask the response from superconducting phase and standard dc measurements would reveal only the existence of ferromagnetic hysteresis. In that case cooperation of ac and dc fields is necessary.

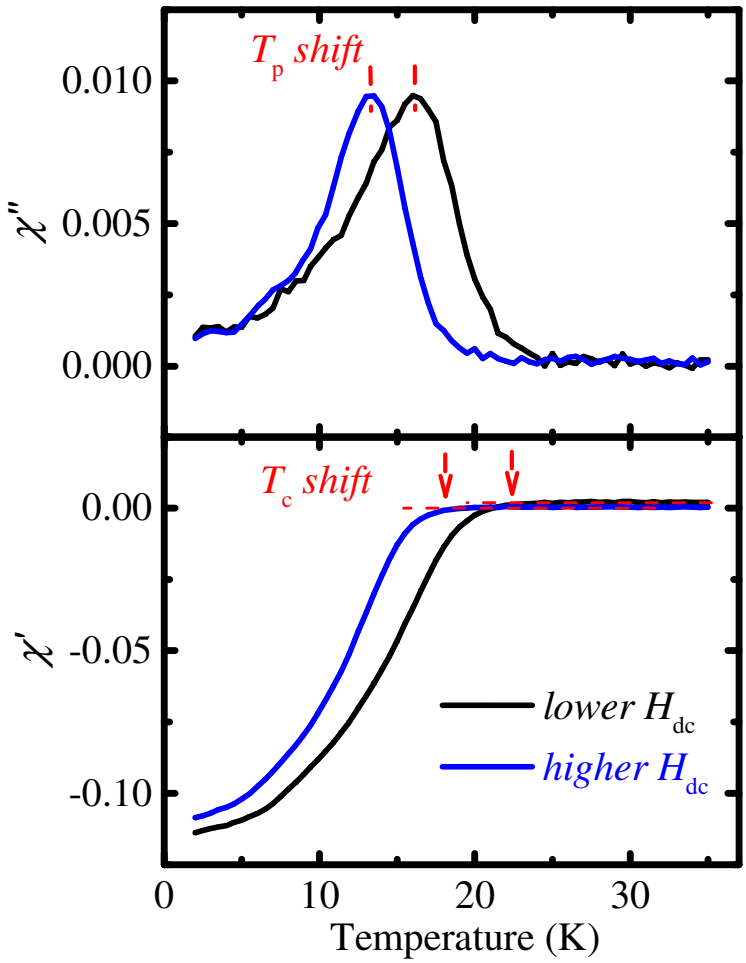

Figure 2.8. Temperature dependences of ac susceptibility, obtained in superimposed ac and dc field. H_{ac} and f are static. Black line measured at lower biased dc field H_{dc}, blue – at higher. The red dashed lines and arrows point out a shifting of T_p and T_c with increasing magnetic field, respectively. The results were obtained for intercalated $Li_x(C_2H_8N_2)(Fe_ySe_zS_{1-z})$ system.

The concept of H_{c2} determining consist in probing of the initial magnetization branch of type II superconductor with ac field of specific fixed amplitude. The movement along the branch is provided by sweeping of dc magnetic field. As soon as the probed state reveals diamagnetic character of the response, the system remains at superconducting state. It is supposed that change of the sign of response is accompanied to reaching of H_{c2}.

Visually, the influence of dc field is expressed in simultaneous shifting of $\chi'(T)$ transition and $\chi''(T)$ peaks to lower temperatures on field increasing (fig. 2.8). As a consequence, $H_{c2}(T)$ is constructed [73]–[75]. Besides, applied dc field leads to additional drift of the loss peak, which allows to estimate $H_{irr}(T)$ [75], [76]. Nevertheless, the validity of method is bounded by type of investigated material, which influences on internal magnetic field distribution.

Summarizing, magnetometry techniques which help to define parameters H_{c1} and H_{c2} and related ξ and λ are in essence based on study of vortex state: penetration of investigated material by first vortex pronounces the onset of H_{c1}, meanwhile the overlapping of vortex cores – onset of H_{c2} and destroying of superconducting state. With regard to well-studied superconducting materials, i.e. cuprates, dc magnetometry seems applicable for superconducting state parameters determining. However, the distribution of votices within the material is strongly influenced by the presence of magnetic inclusions and inhomogeneities, which is the case of organic intercalated iron-based systems. Those inhomogeneities introduce the competing non-superconducting fluctuations, which worsen the superconducting abilities of the material and hence decisively distort the results of magnetization measurements. The peculiar consequent distribution of magnetic field within the material makes field dependences of magnetization rather useless. In turn, proposed analysis of temperature dependences of ac susceptibility in superimposed ac and dc magnetic fields uniquely allowed to estimate the upper critical field H_{c2} and to construct $H_{c2}(T)$ phase diagrams of organic intercalated iron chalcogenides.

Strictly, deep and comprehensive investigations of superconducting state demand complex cooperation of measurement techniques. Apart from above described, there can be highlighted:

1) Specific heat measurements, which are realized by means of calorimetric techniques and based on recording of specific heat as a function of temperature $C(T)$ (fig. 2.9a). The analysis of $C(T)$ peak magnitude allow to define the entropy

change and related latent heat releasing during the transition to superconducting state, meanwhile its position indicates the value of T_c. Besides, the activational character of electronic contribution to specific heat $C_e(T)$, which can be expressed with the exponent function of $-2\Delta/k_B T$, defines the magnitude of superconducting band gap 2Δ. Moreover, gauging of $C(T)$ in the external magnetic field can be realized in order to $H_{c2}(T)$ phase diagram constructing.

2) Muon spectroscopy μSR (muon spin rotation and relaxation) (fig. 2.9b), where the positive charged and polarized muons of half-integer spin are implanted into the material with sequential exposing to external magnetic field. The direction of magnetic field with respect to initial spin-polarization defines the type of measurements: perpendicular for transverse field (TF) μSR, anti-parallel for longitudinal field (LF) μSR, without external magnetic field for zero-field (ZF) μSR. By analyzing μSR spectra it is possible to figure out the microscopic distribution of magnetic field inside the material and in the case of superconductors to estimate the field penetration depth λ.
3) Angle-resolved photoemission spectroscopy ARPES (fig. 2.9c), where the energy of photoelectrons is recorded with regard to emission angle, which allows to create a detailed map of electronic band structure of the material in the reciprocal space (or $\boldsymbol{k}$-space, $\boldsymbol{k}$ – wavevector) and as a consequence to evaluate the magnitude of superconducting band gap 2Δ strightforwardly.

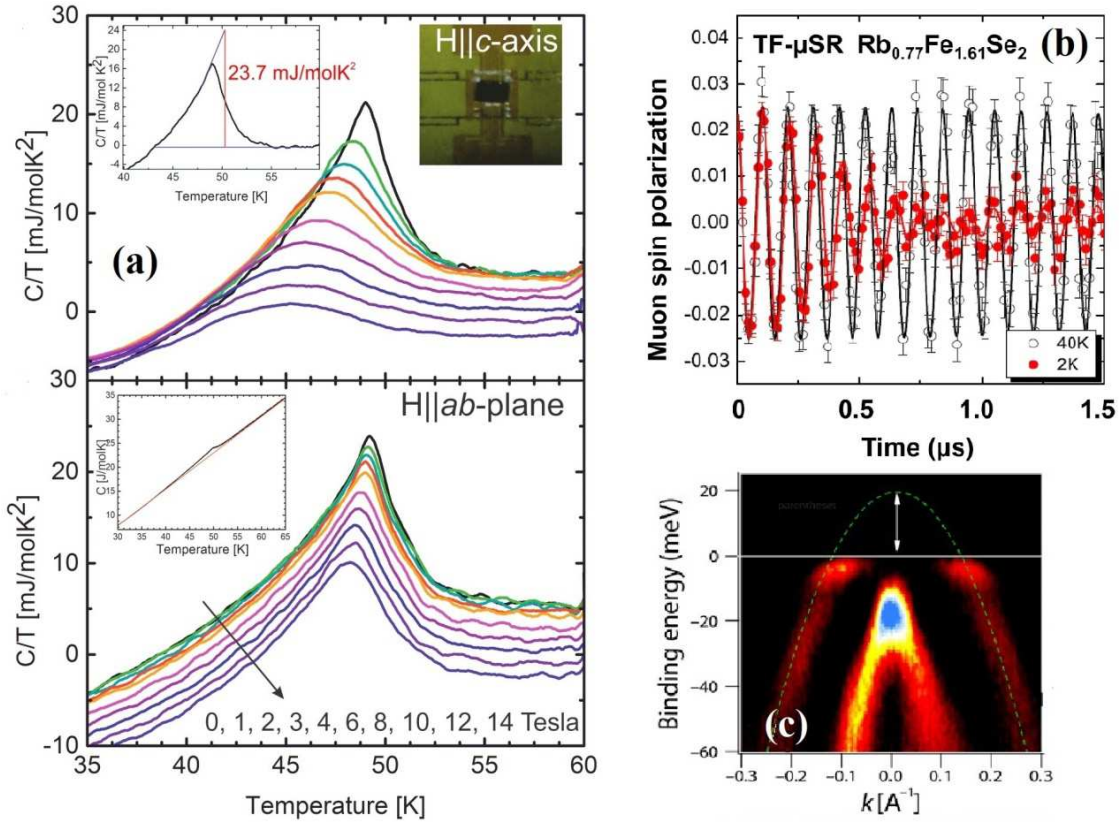

Figure 2.9. (a) Specific heat dependences recorded as a function of temperature $C(T)$ at several dc magnetic fields for SmFeAs(O,F) single crystal illustrates shifting of the peak with regard to field changing. Reprinted with permission from [77]. Copyright 2023 by the American Physical Society. (b) μSR spectrum measured above the T_c at 40 K and below at 2 K for $Rb_{0.77}Fe_{1.61}Se_2$ single crystal. The oscillations dumping on 2 K dependence is related to the existence of vortex phase in superconducting state. Reprinted with permission from [78]. Copyright 2023 by the American Physical Society. (c) ARPES spectrum obtained at 1 K for $Fe_{1+y}Se_xTe_{1-x}$. Estimated bandgap is of about 3 meV. Reprinted from [79]. © The Authors, some rights reserved; exclusive licensee AAAS. Distributed under a CC BY-NC 4.0 License.

Nevertheless, presented work is focused on exploring of superconducting state by applying magnetization measurements for specific superconducting materials – copper oxide and organic intercalated iron chalcogenide systems.

III. Equipment base and measurement techniques

Laboratory study of magnetization is usually provided with commercial magnetometers of two types: VSM (*Vibrating Sample Magnetometer*) and SQUID (*Superconducting Quantum Interference Device*). While the former one is more universal and used either as a separate tool or as an additional option within measurement systems (e.g. PPMS), SQUID is always incorporated in more sophisticated equipment. However, namely SQUID is treated as the most sensitive instrument for magnetic moment measurements. SQUID integrated with MPMS (*Magnetic Property Measurement System*) from Quantum Design allows to reach the precision of the order of 10^{-11} A·m^2 (10^{-8} emu in CGS) [35].

Principle of SQUID operation is based on Josephson effect [3]. General sense of the effect lays in tunneling of Cooper pairs through the insulating junction, which couples two superconducting regions. The width of junction should be less than coherence length. The value of current flowing freely through the junction is proportional to the difference of wave functions phases, which describe two SC areas. If then place the considered system into magnetic field, it turns out, that the maximal intensity of flowing current is modulated by the magnetic flux. embraced inside the junction. Phase difference of wave functions, or in fact order parameters, is described as follows [35]:

$$\frac{d\theta}{dt} = \frac{2eU}{\hbar} = \frac{2\pi U}{\Phi_0}, \tag{3.1}$$

where Φ_0 – magnetic flux quantum, U – voltage, generated on junction as a consequence of exceeding of critical current value. Noteworthy, ratio $2eU/\hbar$ determines the frequency of flowing through the junction current.

In turn, if the system would look like a ring with two junctions, penetrating through the ring plane magnetic flux results in creating of phase difference on junctions. The effect resembles optical interference and gave the name to the device, which uses it [80]. Two junctions' device was called dc (*direct current*) SQUID. Maximal current I_{max} flowing through the ring is represented as periodical function of magnetic flux Φ [35]:

$$I_{max} = 2I_c \left|\cos\left(\frac{\pi\Phi}{\Phi_0}\right)\right|. \tag{3.2}$$

Since the exceeding of critical current I_c leads to transition to the resistive state, voltage drop evolves periodically with regard to value of quantized magnetic flux. Practically, that relation

provide the feasability of recalculating of measured voltage to magnetic flux, and hence to magnetic moment. Historically, dc-SQUID appeared as first and was burdened with additional wires to link it up with measurement system.

Nevertheless, modern systems (e.g. MPMS) are equipped with contactless single junction device – rf (*radio frequency*) SQUID, sometimes also called ac (*alternative current*) SQUID. Here, the detector is inductively coupled to the circuit. The intensity of flowing current in the SQUID coil appears as [80]:

$$I = -I_c \sin\left(2\pi \frac{\Phi + LI}{\Phi_0}\right), \tag{3.3}$$

where the additional term LI is related to circuit inductance L, Φ describes the flux, which is inderectly generated by external magnetic field $B_{ext} = \mu_0 H_{ext}$ [80].

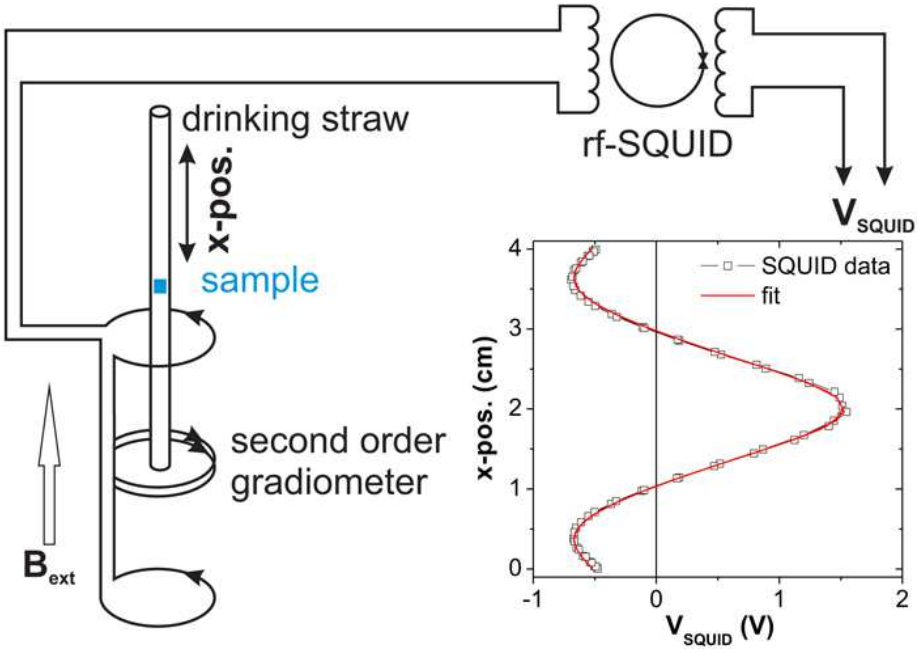

Figure 3.1. The realisation of magnetic measurements by means of rf-SQUID within the dc regime. Picture was taken from [81].

The rf-SQUID allows to measure the magnetic moment by utilizing of both dc and ac regime.

Technically, either dc or ac measurements are started from centering of the sample within superconducting pick-up coils, which are designed as a second-order gradiometer (fig. 3.1). Sources of either dc or ac fields are corresponding superconducting magnets, which are arranged coaxially with pick-up coils and sample chamber. Applied external field B_{ext} magnetizes the sample that moves through the gradiometer. It is supposed that B_{ext} is

uniformly distributed along the sample path. Induced response is detected by SQUID, which is located quite distantly from the sample chamber – at thermally stable and protected from electromagnetic noises place. Since SQUID works as a flux-voltage transformer, output data appear as a function of voltage via position of the sample. Next, the raw measured points are fitted with following relations supposing dipole approximation:

$$V(z) = C\left\{\frac{2}{[\mathrm{r}^2 + (z - z_0)^2]^{\frac{3}{2}}} - \frac{1}{[\mathrm{r}^2 + (z - z_0 - \mathrm{D})^2]^{\frac{3}{2}}} - \frac{1}{[\mathrm{r}^2 + (z - z_0 + \mathrm{D})^2]^{\frac{3}{2}}}\right\}, \quad (3.4)$$

where z_0 – central position within pick-up coils, D – distance between coils, r – radius of the coil, C – calibration coefficient [82], [83]. Fitted voltage dependence (also called *scan*) is converted to magnetic moment value. During the dc measurements, procedure is executed several times to obtain averaged signal.

Within the ac regime centered sample is exposed to oscillating alternative field:

$$h_{\mathrm{ac}}(\omega t) = H_{\mathrm{ac}} \cos(\omega t). \quad (3.5)$$

Measured time-dependent magnetic moment from voltage response (fig. 3.2) is described with periodic sinusoidal function:

$$m_{\mathrm{ac}}(\omega t) = \left(\frac{dM}{dH}\right) H_{\mathrm{ac}} \cos(\omega t), \quad (3.6)$$

where $\omega = 2\pi f$ – angular frequency of the drive field, t – measurement time. dM/dH – slope of magnetization curve $M(H)$ at specific temperature and the target purpose of ac measurements, i.e. χ_{ac} [66], [84]. Comprising components of ac susceptibility – $\chi'(\omega)$ in-phase (real) and $\chi''(\omega)$ out-of-phase (imaginary) – are usually measured separately and represented as:

$$\chi'(\omega t) = \chi_{\mathrm{ac}} \cos(\omega t), \quad (3.7)$$

$$\chi''(\omega t) = \chi_{\mathrm{ac}} \sin(\omega t), \quad (3.8)$$

$$\chi_{\mathrm{ac}} = \sqrt{\chi'^2 + \chi''^2}. \quad (3.9)$$

If the measurement is conducted in superimposed ac and dc fields, the applied field can be represented as a sum of bias dc field H_{dc} and oscillating ac field:

$$h(\omega t) = H_{\mathrm{dc}} + H_{\mathrm{ac}} \cos(\omega t). \quad (3.10)$$

As soon as the superconducting materials of type II express non-linear behavior in superimposed ac and dc fields above the lower critical field H_{c1}, measured time-dependent magnetic moment can be rewritten as [85]:

$$m(\omega t) = M_0 + H_{ac} \sum_{n=1}^{\infty} [\chi'_n(\cos(n\omega t) + \chi''_n \sin(n\omega t)]. \quad (3.11)$$

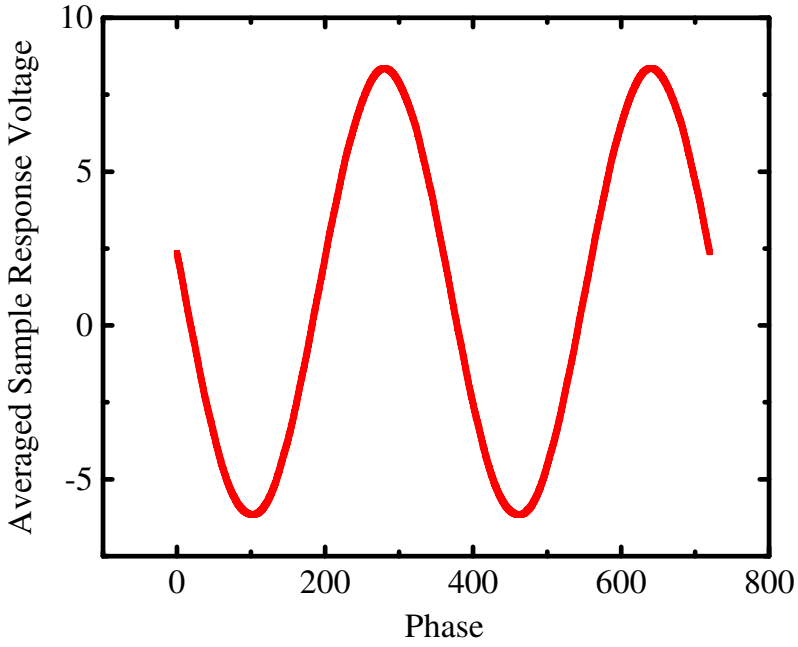

Figure 3.2. Phase-dependent voltage response – ac scan, which is used for ac susceptibility calculation.

The above-described techniques are completely available in Quantum Design MPMS *XL*7, which was the main investigating instrument in presented work. Specific feature of measurements, which were performed by utilizing of the equipment was the feasibility of measurements only of longitudinal component of magnetic moment, i.e. which is parallel to applied external field. Meanwhile, the reciprocating sample option (*RSO*), which was utilized in the case of dc measurements implementing, allowes to gather the voltage-position response from the sample by high-frequency oscillating movement within the pick-up coils with automatical conversion of the response to magnetic moment values with 10^{-11} A·m^2 precision. Writing of measurement algorithm (*sequence*) as well as the subsequent results recording were realized by utilizing standard software *MultiVu* from Quantum Design.

IV. Superconducting state properties of $CuBa_2Ca_3Cu_4O_{10+\delta}$ (Cu-1234) system

IV.1. *Motivation*

IV.1.1. What are cuprates?

Breakthrough of Bednorz and Müller gave tremendous boost for investigations of not only newly discovered class of materials, i.e. cuprates, but in fact opened a black box of high-temperature unconventional superconductivity. Importantly, the clue basement of conventional superconductivity lays in phonon-mediated character of Cooper pairs coupling, which is experimentally expressed in isotope effect existence. Noteworthy, unconventional or non-BCS behavior was known from 1979 after the discover of heavy-fermion $CeCu_2Si_2$ with the T_c of about 0.5 K [86]. High-temperature cuprates violate the BCS scenario as well, but remain the Cooper pairs as charge carriers though [8]. Although, pairing mechanism in cuprates is still under the debates, some of their general features were defined relatively precisely and can be highlighted.

1) Complex crystal structure. Copper-based materials are typically layered compounds, which crystallize in perovskite structure and consist of an arranged stack of copper-oxide layers CuO_2 separated by layers of different atoms: Y, Ba, Bi, La, Hg, etc – also called charge reservoir layers. The CuO_2 layers are where the superconductivity originates, while the charge reservoir layers provide carriers to the superconducting layers. The specific arrangement of atoms and the structure of the copper-oxide layers influence the electronic properties of cuprates [87], [88].
2) Quasi-two-dimensionality of their systems. The electronic motion is restricted within the superconducting CuO_2 layers, leading to highly anisotropic behavior, where the properties can vary significantly in different crystallographic directions.
3) Pseudogap existence. Cuprate superconductors exhibit a pseudogap phase in their normal state above the superconducting transition temperature [89]–[91]. The pseudogap phase is characterized by a partial suppression of electronic density of states at the Fermi level. The origin and nature of the pseudogap phase are still under investigation, and it is considered one of the challenging aspects of cuprate superconductivity.
4) Strong electron-electron interactions. These interactions arise from the electronic configuration of the copper ions in the copper-oxide layers and the arrangement of

oxygen ions. The strong interactions play a crucial role in the emergence of superconductivity and give rise to other phenomena such as the Mott insulating state and the pseudogap phase.

5) Dopability. The superconducting properties of cuprate compounds can be modified by chemical doping, which involves introducing impurities or changing the stoichiometry. Doping can enhance or suppress superconductivity and alter the phase diagram of the materials. Hole-doping (removing oxygen or adding electron acceptors) or electron-doping (adding oxygen or adding electron donors) is commonly used to control the carrier concentration and tune the superconducting properties of cuprates [92]–[94].

Unusual complex properties of perovskite copper-based ceramics led to its intensive exploring. As a consequence, numerous family of high-temperature materials arose, which contain members with T_c of about 130 K – $HgBa_2Ca_2Cu_3O_{7+\delta}$ system. Over the course of more than three decades since their discovery, cuprate superconductors, particularly YBaCuO (Y-123) and BiSrCaCuO (Bi-2223), have emerged as highly promising materials with significant scientific and practical potential. YBaCuO and BiSrCaCuO have already demonstrated their applicability in high-power applications such as superconducting magnetic energy storage (SMES) and power cables. However, it should be noted that YBCO's critical temperature (T_c) of approximately 93 K is only slightly higher than the boiling temperature of liquid nitrogen (77 K), which limits its operational range. On the other hand, BSCCO exhibits complex superconducting parameters with high anisotropy, making its mass production and utilization more challenging [15]. System with highest T_c among cuprates – Tl-doped $HgBa_2Ca_2Cu_3O_{7+\delta}$ – contains toxic elements.

IV.1.2. Why Cu-1234 ?

Against that background the intensive investigation of the $CuBa_2Ca_3Cu_4O_{x+\delta}$ (Cu-1234) system is motivated by several key factors. Firstly, it exhibits a relatively high T_c of approximately 116 K under ambient pressure conditions. Furthermore, this system demonstrates low crystallographic anisotropy and lacks toxic elements, which are crucial considerations for its practical utilization in devices [17], [18], [95]. These features position the Cu-1234 system favorably compared to other cuprate high-temperature superconductors (HTSCs) in terms of device production. Additionally, the Cu-1234 system displays a significantly high critical current density (j_c) on the order of 10^4 A/cm^2 at 77 K [19].

However, the nature of real-world conductors, such as wires and cables, being polycrystalline, introduces a notable significance in the analysis of structural imperfections, notably grain boundaries. The presence of such imperfections strongly influences the superconducting state parameters of the material [16], [96]. Moreover, the irreversibility field ($H_{irr}(T)$) plays a crucial role in determining the limitations of the critical current. It indicates the point at which the material transitions into the flux creep regime. Hence, it is essential to acknowledge the influence of the irreversibility field in the pursuit of enhancing superconducting parameters.

Consequently, the improvement of superconducting parameters necessitates the establishment of phase diagrams for $H_{c2}(T)$, $H_{irr}(T)$, and $H_{c1}(T)$. These phase diagrams, along with microscopic parameters such as the coherence length (ξ) and penetration depth (λ), offer a comprehensive description of the superconducting behavior exhibited by the investigated system.

IV.2. *Synthesis and Measurements description*

IV.2.1. Synthesis

Polycrystalline sample of nominal chemical composition of $CuBa_2Ca_3Cu_4O_{10+\delta}$ was synthesized by utilizing combined high-pressure and high-temperature method. The details of the metod are quite deeply described already [97]. The precursors – BaO_2, CuO, CaO powders – are mixed in proper amounts so that the proportion Ba:Ca:Cu = 2:3:4 would remain. After the calcination treatment the material is pressed into a pellet and exposed to subsequent high-pressure processing up to 6 GPa by means of cubic anvil cell utilizing and heating up to 1273 K. Such conditions are maintained for 30 minutes. Before reducing of the pressure, resulted sample is cooled down to room temperature. Importantly, graphite sleeve was used as a heater, meanwhile gold container as a form for the pellet.

IV.2.2. XRD measurements

X-ray diffraction (XRD) measurements were conducted by means 3kW-Rigaku X-Ray Powder Diffractometer, which is equipped with D/teX Ultra 250 detector. The room temperature measurements were realized by applying Cu K_α (1.54060 Å of wavelength) radiation in $\theta - 2\theta$ focusing conditions within the scan range of angles of 5 – 100 degrees. XRD spectrum was recorded with the step of 0.01 degree.

IV.2.3. Magnetic measurements

The Quantum Design Magnetic Property Measurement System (MPMS) *XL*7 SQUID was employed for the magnetic characterization of the investigated material. The selection of either direct current (dc) or alternating current (ac) methods depended on the specific research objectives. To ensure the integrity of the experimental setup and enhance result clarity, the sample was securely placed within a non-magnetic standard plastic straw. This choice of sample enclosure effectively provided a homogeneous background throughout the measurement process, as depicted in fig. 4.1.

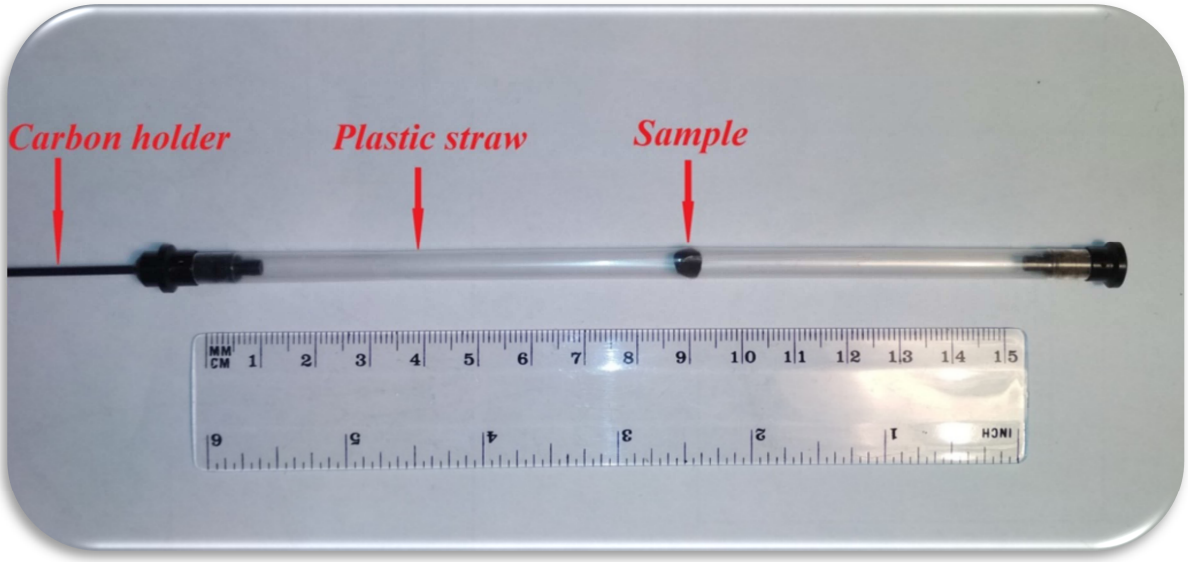

Figure 4.1. Mounting of $CuBa_2Ca_3Cu_4O_{10+\delta}$ sample for magnetic measurements.

The temperature and field dependences of the magnetic moment were investigated using the dc method. Temperature variations of the magnetic moment were determined through the implementation of both the zero-field cooling (ZFC) and field-cooled cooling (FCC) protocols. Field dependences were recorded after cooling at zero dc field always. To assess the ac susceptibility, the real component (χ') and imaginary component (χ'') were simultaneously measured. This was achieved by employing the ZFC protocol at a fixed frequency of the oscillating ac field, without the application of any superimposed dc magnetic field.

IV.3. *Results and discussion*

IV.3.1. XRD results

The results of XRD qualitative phase analysis revealed presence of several phases in investigated sample (fig. 4.2 upper panel). Apart from dominating phase of target cuprate material Cu-1234, it turned out that the sample contained also CaO (*lime*), CuO (*tenorite*), C (*graphite*) phases. Besides, Cu-1234 phase showed slight deviation of nominal composition, namely there was indicated the stoichiometry of $Cu_{0.68}Ba_2Ca_3Cu_4O_{10.4}$, which means the existence of partially occupied state with regard to copper (Cu) and oxygen (O) atoms positions. Tetragonal crystal system of *P4*/*mmm* space group which inherent to the main phase and obtained lattice parameters are in a good agreement with literature data [18], [98], [99]. Analytically calculated density of the material of about 5.52 g/cm^3 is utilized in magnetometry data processing. Averaged size of major phase crystallites was assessed and reached the value of 496 Å.

IV.3.2a. Magnetometry results – preliminary measurements

Preliminary magnetometry studies were undertaken to gather initial results concerning the temperature dependence of the magnetic moment. These measurements were conducted at a constant dc field of 1 mT (fig. 4.3a). The analysis of the acquired curves revealed the initiation of a transition to the superconducting state at a comparatively high temperature, denoted as T_c^{onset}, reaching 117.5 K. This value demonstrates similarity to existing literature data for materials belonging to the Cu-1234 group, albeit with differing oxygen content [18], [19].

The assessment of the superconducting volume fraction, based on magnetization measurements under zero-field cooling conditions at 2 K, resulted in an estimated value of approximately 100%. This estimation considered the influence of demagnetizing effect. The observed divergent behavior of the ZFC–FCC curves is frequently associated with the presence of vortex matter pinning [100]–[102]. Moreover, an additional phase transition was observed in the ZFC dependence near 100 K. This phenomenon can be ascribed to either the coexistence of a secondary superconducting phase [97], [103], or the manifestation of step-like behavior of weak links [104], [105]. Such occurrences are commonly encountered in comparable granular materials.

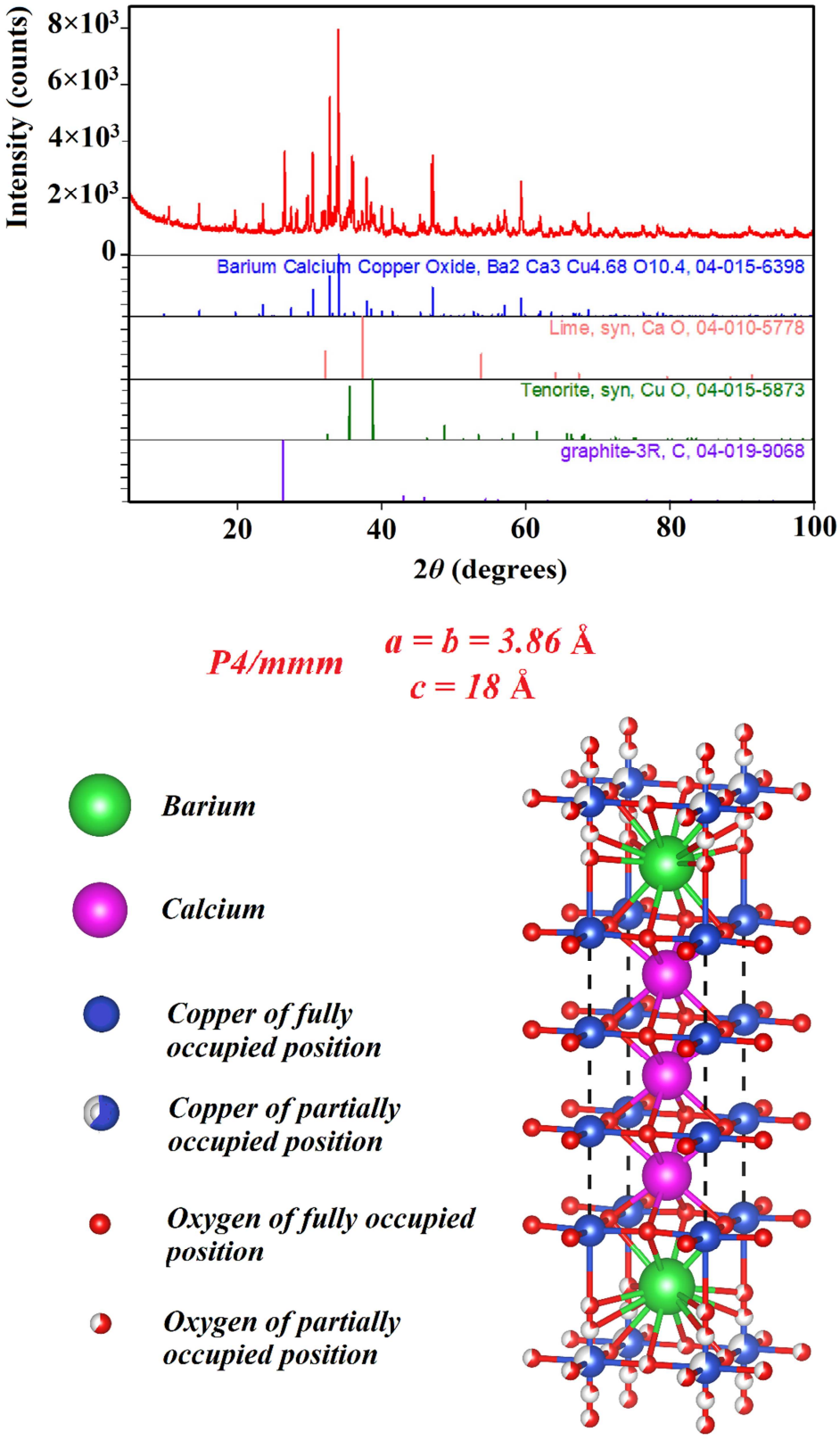

Figure 4.2. Upper panel – results of XRD measurements; lower panel – structure of crystal lattice of explored material, which is reproduced by using crystallography materials database. The occupancy of the position is a direct consequence of considered stoichiometry.

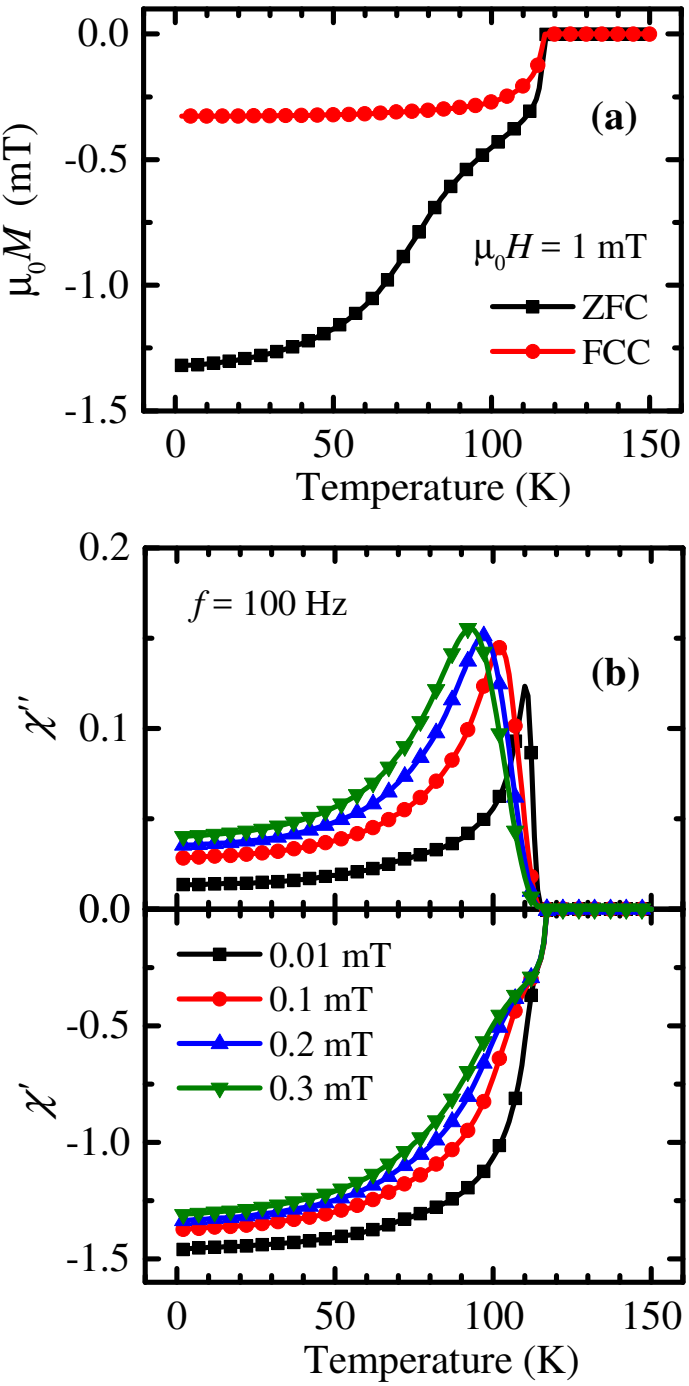

Figure 4.3. (a) Temperature dependences of magnetization recorded at 1 mT of external dc field in zero-field cooling (ZFC) and field cooling (FCC) modes. (b) An imaginary part χ'' and a real part χ' of ac susceptibility measured as functions of temperature by applying ac field of 100 Hz of frequency with different amplitudes: black squares – for 0.01 mT, red circles – 0.1 mT, blue triangles – 0.2 mT, green inverted triangles – 0.3 mT. Each of ac susceptibility curves was normalized by corresponding ac field value. The results were published already [106].

To thoroughly investigate the superconducting state of the system, ac susceptibility measurements were conducted. Technically, these measurements involved sequentially applying oscillating fields with amplitudes of 0.01, 0.1, 0.2, and 0.3 mT, with each curve corresponding to a specific ac field. A common frequency of 100 Hz was employed for all ac susceptibility experiments. The results depicted in fig. 4.3b validated the findings from the dc investigations, confirming the accuracy of the estimated T_c^{onset} value and the occurrence of the second transition.

The onset of diamagnetic behavior, observed in the in-phase component χ', remained consistent, unaffected by the strength of the applied ac field (fig. 4.3b). However, the step-like transition became more pronounced with increasing of ac field amplitude and shifted towards lower temperatures. It is noteworthy that the saturation values of χ' at low temperatures progressively increased, indicating an improved response from the shielding phase. Concurrently, the amplitude of the corresponding out-of-phase loss peak χ'' (fig. 4.3b) increased, following the movement of the bend in the real part component. The observed pattern in the ac curves resembles the results reported for YBaCuO in previous studies [107], [108] indicative of weak link behavior.

According to the weak links theory, granular systems are regarded as assemblies of grains interconnected by grain boundaries, specific Josephson junctions [109]. It is established that defective grain boundaries possess inferior superconducting properties and are less effective in transferring of supercurrent compared to the grains themselves [103]–[105]. Hence, the presence of such weak junctions results in a non-simultaneous response to an applied external magnetic field.

As per the aforementioned discussion, the onset of superconducting behavior observed in $\chi'(T)$ is attributed to the circulation of screening currents on the surfaces of the grains (intragranular currents), while the contribution of the current through weak intergranular connections to the overall screening of the material becomes significant only upon cooling below the step-like transition. Against this backdrop, the singular loss peak character of $\chi''(T)$ substantiates the strongly inhomogeneous nature of the investigated sample, as it correlates with the intergranular step-like transition.

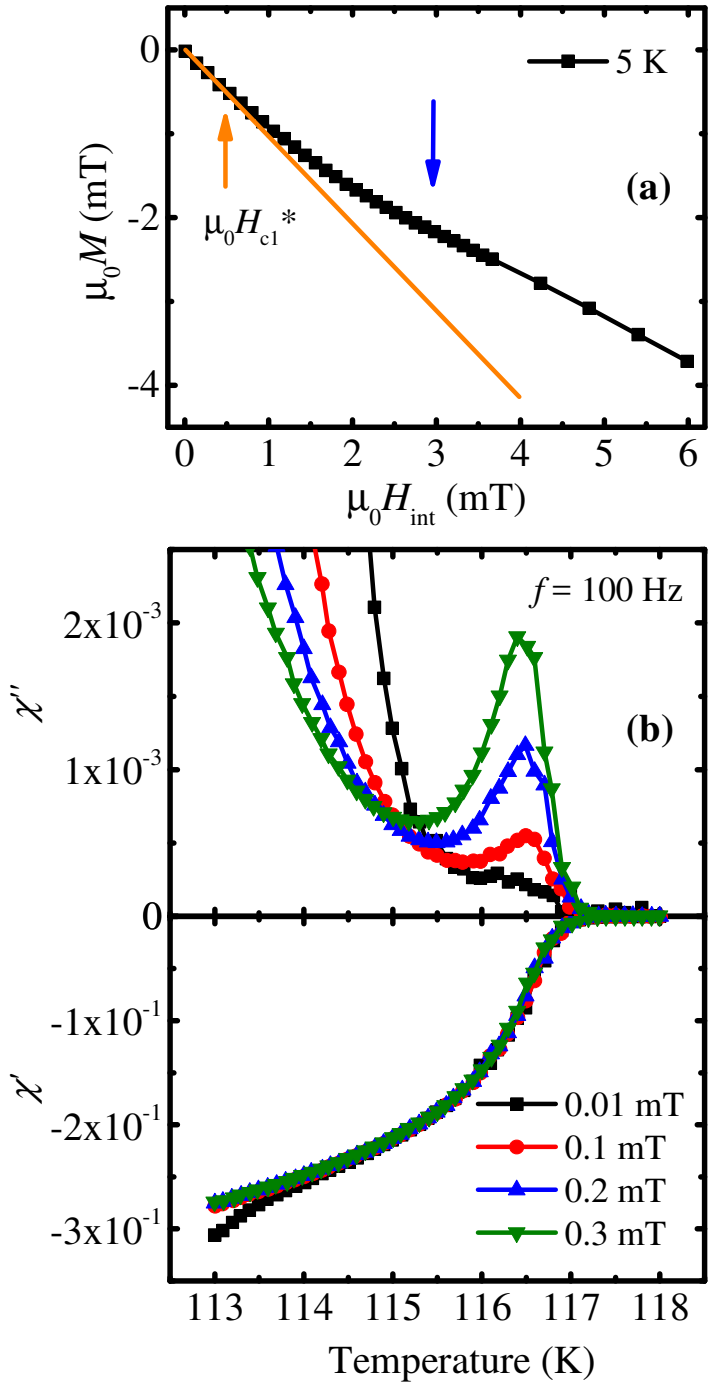

Figure 4.4. (a) The initial magnetization curve, which is represented as a function of $\mu_0 H_{int}$ magnetic field at the temperature of 5 K. The blue arrow points out the bend, which reflects the transition from lower-field intergranular to higher-field intragranular regime. Orange arrow indicates the penetration of the material with supercurrent vortices within the intergranular regime. (b) illustrate the scaling up of the imaginary and the real parts of ac susceptibility respectively, which were redrawn in the narrow range of temperature, i.e. in the vicinity of transition to superconducting state; $\chi''(T)$ depicts the dynamic of intragranular loss peak change. Each of ac susceptibility curves was normalized by corresponding ac field value. The results were published already [106].

More careful ac susceptibility measurements detected the presence of secondary loss peak right in close proximity to the onset of the superconducting state (fig. 4.4b). This peak arises due to the penetration of the magnetic field into the grains [71], [108], [110]. Hence, the substantial loss peak observed in fig. 4.3b is entirely attributed to dissipation associated with the circulation of screening current through weak connections.

The initial magnetization branch was obtained by representation of magnetization as a function of the internal field H_{int} after measuring within a narrow range of external dc field at a temperature of 5 K. To correct for the demagnetizing effect, the expression: $H_{int} = H_{ext} - DM$ (H_{ext} – applied dc magnetic field, M – measured magnetization, D – demagnetizing factor) (fig. 4.4a). The demagnetizing factor D was experimentally estimated by fitting the Meissner line (depicted as the orange line in fig. 4.4a) and was determined to be 0.27. Calculated demagnetizing factor value remained valid for all the results presented in section IV since the sample was consistently measured in the same direction relative to the applied external dc field. The observed dependence itself clearly exhibits a distinct curvature. Evidently, this curvature corresponds to the transition from intergranular to intragranular screening at higher magnetic fields [111]. Similar to findings reported in [34], it can be inferred that there exists an intergranular lower critical field, denoted as $\mu_0 H_{c1}^*(T)$ of the approximate magnitude of 0.5 mT. As far as the transition occurs at a relatively low field of around 3 mT, subsequent magnetization experiments at high fields were conducted within the intragranular regime, where the individual grains are disconnected and behave independently.

IV.3.2b. H_{c1} defining

A series of magnetization measurements as a function of applied magnetic field were conducted under isothermal conditions to determine the lower critical field, $H_{c1}(T)$ (fig. 4.5a). Importantly, the dependences were corrected for the demagnetizing effect as well. By considering the deviation from linear diamagnetic behavior in these field dependences as an indication of the onset of Abrikosov vortices penetration in the sample [112]–[114], the corresponding data points were collected after subtracting the diamagnetic baseline (fig. 4.5a). These data points were then utilized to construct the phase diagram of $H_{c1}(T)$ (fig. 4.5b). The overall shape of the $H_{c1}(T)$ curve is irregular and can be roughly divided into two parts: a low-temperature region and a high-temperature region, with an inflection point occurring around 15 mT. However, neither of these regions exhibits a parabolic dependence. The lower critical field at 5 K was determined using the method described earlier and was found to be 44 mT.

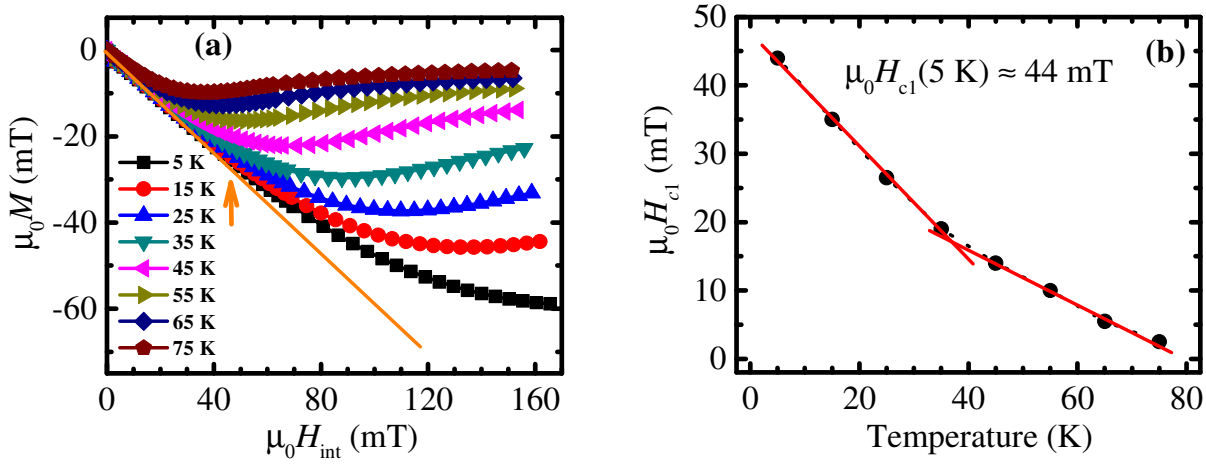

Figure 4.5. (a) Isothermal field dependences of magnetization. Orange arrow points the moment of deviation of 5 K magnetization curve from diamagnetism (orange straight line). (b) Phase diagram of lower critical field represented as a function of temperature. The results were published already [106].

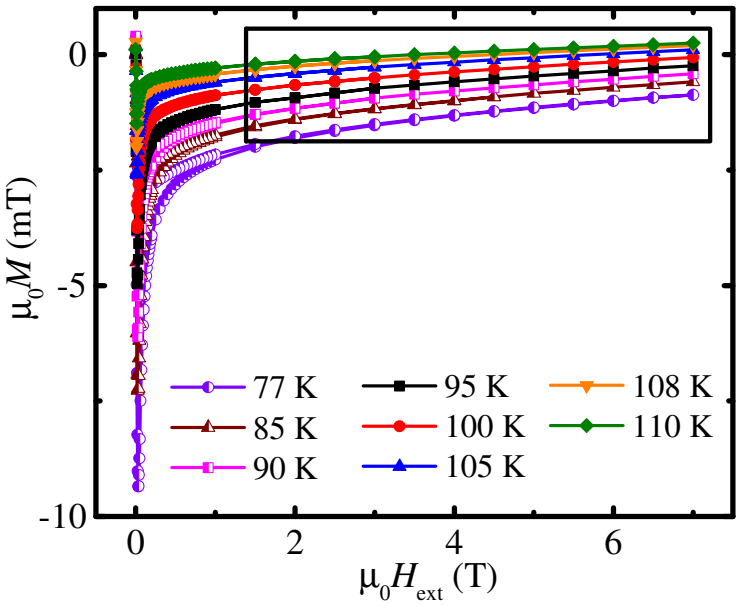

Figure 4.6. Field dependences of magnetization represented as halves of hysteresis loops at following temperatures: 77 K – for violet half-filled circles, 85 K – brown half-filled triangles, 90 K – magenta half-filled squares, 95 K – black squares, 100 K – red circles, 105 K – blue triangles, 108 K – orange inverted triangles, 110 K – green rhombi. The results were published already [106].

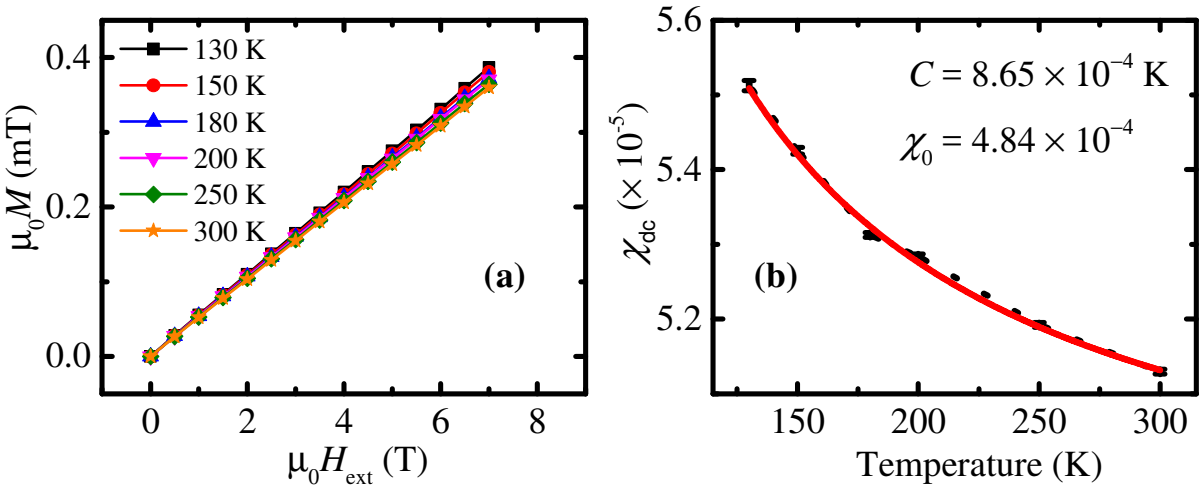

Figure 4.7. (a) Field dependences of magnetization recorded at $T > T_c^{onset}$: black squares for 130 K, red circles – 150 K, blue triangles – 180 K, magenta inverted triangles – 200 K, green rhombi – 250 K, orange stars – 300 K; (b) the approximation of temperature dependence of paramagnetic susceptibility χ_{dc}: red curve corresponds to fitting by considering both Curie and Van Vleck contributions, C and χ_0 – parameters of fitting. C has Kelvin units since the magnetization $\mu_0 M$ was recalculated in Tesla. The results were published already [106].

IV.3.2c. H_{c2} defining

Isothermal loops of magnetization were measured to investigate the irreversible properties of the material and to determine the upper critical field (fig. 4.6). Notably, these loops exhibit a remarkably narrow shape, where the ascending and descending branches closely overlap. This characteristic suggests relatively weak irreversible properties and consequently, relatively low values of the irreversibility fields, H_{irr}.

Since the expected values of the upper critical fields are high for Cu-1234 family, it turned out that their estimating from temperature dependences of magnetization is impossible. Then, $H_{c2}(T)$ was defined from the same field dependences of magnetization, but by considering the initial magnetization curve, which practically is almost merged with the fully reversible part of it i. e. where loop is completely closed – the region is embraced with black rectangular in fig. 4.6.

In order to eliminate the influence of possible paramagnetic inclusions, considered set of curves was obtained after the subtraction of corresponding paramagnetic contribution:

$$M(T) = \left(\frac{C}{T} + \chi_0\right) \mathrm{H}\,, \qquad (4.1)$$

where the first term of relation is responsible for temperature dependent Curie susceptibility, while the second one – for temperature independent Van Vleck susceptibility. For that purpose several isothermal magnetization dependences were measured up to 7 T within the temperature region above the transition temperature T_c^{onset} (fig. 4.7a). The dependences turned out to be straight lines of gradually rising slope with the increase of temperature. As far as those slopes represent in fact dc susceptibility χ_{dc} at corresponding temperatures, the $\chi_{dc}(T)$ can be plotted (fig. 4.7b). Each point of $\chi_{dc}(T)$ was plotted with marked deviation, calculated as an error during the approximation of $M(H_{ext})$ with straight lines. The approximation of $\chi_{dc}(T)$ was conducted by utilizing the equation (4.1). Assuming that parameters C and χ_0 obtained from fitting well enough describe paramagnetic behavior above T_c^{onset}, they might be also utilize for calculation of paramagnetic contribution below T_c^{onset}. By taking into account the above described, necessary intervals of $M(H_{ext})$ in fig. 4.8a were obtained after the subtraction of paramagnetic contribution calculated along the (4.1) at corresponding temperature.

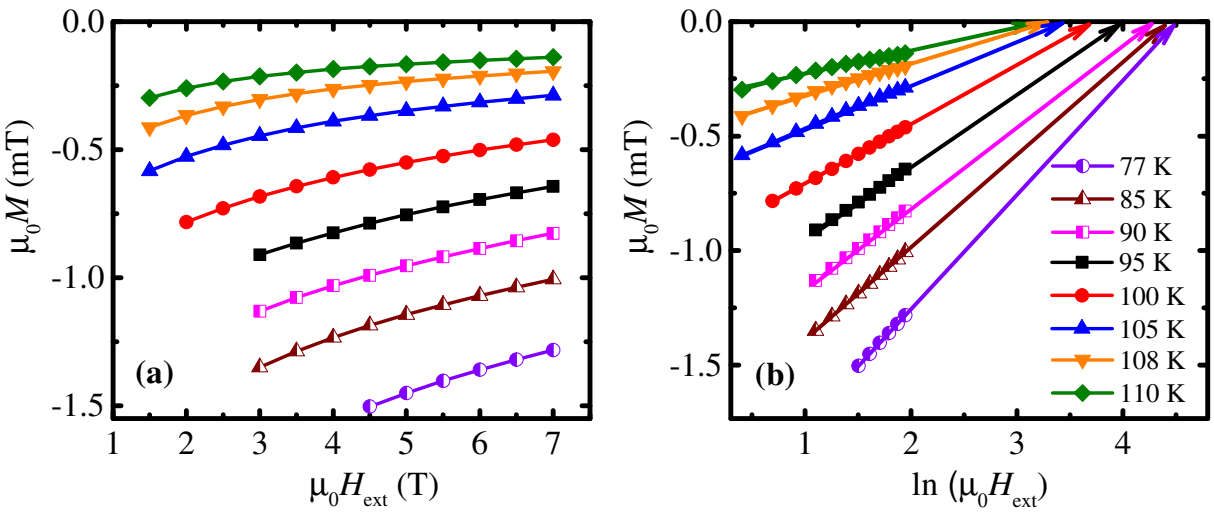

Figure 4.8. An upper critical field H_{c2} defining. (a) The reversible parts of hysteresis loops $M(H_{ext})$, which were obtained after the paramagnetic contribution subtraction. (b) The same parts of hysteresis loops, but represented in semi-logarithmic scale. Arrows point out the linear extrapolation of data to $\ln(\mu_0 H_{ext})$ axis. The results were shown in [106].

The estimation of upper critical field H_{c2} was realized according to London approach (relation 1.21) and layed in extrapolation of in fact linear high field hysteresis loop area till the intersection with the field axis. The fig. 4.8b illustrates a set of linear tails of hysteresis loops, which were plotted in semi-logarithmic scale.

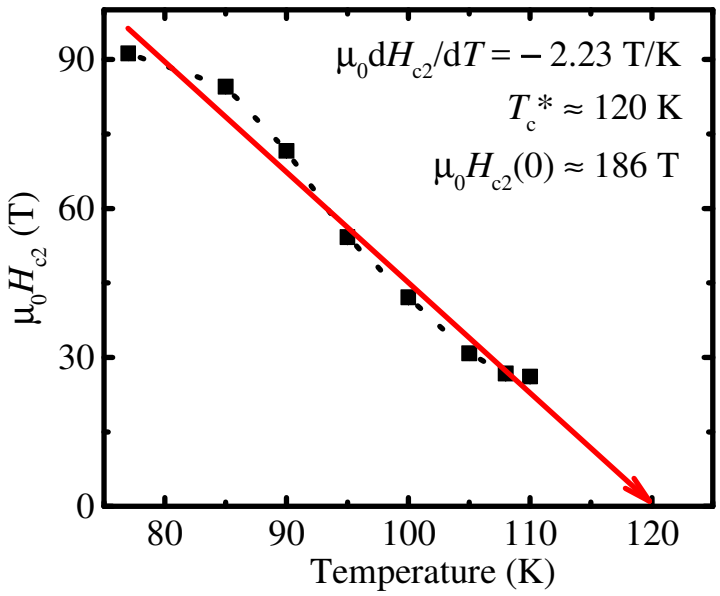

Figure 4.9. An upper critical field as a function of temperature. Red arrow points the critical temperature T_c* predicted by WHH theory. The calculated parameters of WHH equation, i.e. critical temperature T_c*, slope dH_{c2}/dT and zero-temperature upper critical field $\mu_0 H_{c2}$ (0) are placed directly on the figure. The results were published already [106].

The approximation and subsequent extrapolation of resulting curves yielded in reaching of intersection with the field axis and indicates destroying of superconductivity in the material, i.e. obtaining H_{c2} for specific temperature. Gathered points in turn formed the dependence of $H_{c2}(T)$, which is showed in fig. 4.9 for investigated Cu-1234 sample. It is important to admit that due to specificity of extrapolation process itself low-temperature points are estimated less accurately, simply because of higher distance between considered measured low-temperature curve and desired intersection with the field axis.

In order to determine the upper critical field at zero temperature, $H_{c2}(0)$, WHH equation [44] in the context of dirty limit approach was utilized by taking into account relations (1.15). The applicability of WHH theory for cuprate systems was verified in this studies – [59], [115]. The predicted transition temperature, T_c*, according to the WHH theory, was determined by linearly approximating the $H_{c2}(T)$ diagram (indicated by the red arrow in fig. 4.9) and was found to be 120 K, which is 2.5 K higher than the measured T_c^{onset}. Furthermore, the slope of the arrow provided the dH_{c2}/dT parameter. It is important to admit, that $H_{c2}(T)$ is rather *s*-shaped than linear. Nevertheless, using of linear approximation is supposed to be valid, since the diverged point at 77 K is related to imperfectness of the methodology described above, and curved tail in the region close to T_c^{onset} is associated with the influence of non-superconducting fluctuations. The last fact is also can be the cause of

overestimated T_c* with regard to T_c^{onset}. However, obtained value of H_{c2} is in a good agreement with literature data for related systems. Additionally, the zero-temperature coherence length, ξ, was determined by employing the Ginzburg-Landau expression (1.14), which establishes a connection between the upper critical field and the coherence length.

On the other hand, due to the impact of granularity, the $H_{c1}(T)$ diagram (fig. 4.5b) obtained from simple deviation of initial magnetization curves from diamagnetic straight line seems to be underestimated. The cause of it lays in non-neglegible contribution to magnetization caused by penetration of grain boundaries just below H_{c1}, leading to deviation from linear dependence of $M(H)$ in the vicinity of H_{c1} in the field range $H < H_{c1}$. Hence, lack of consistent and more or less predictable dependence of $H_{c1}(T)$ can be related to distorted response from the system, which possesses poor shielding abilities of grain boundaries. Therefore, calculated by means of (1.13) relation and by utilizing of $H_{c1}(5\ \mathrm{K})$ magnetic field penetration depth – $\lambda(5\ \mathrm{K})$ = 138.7 nm – can be treated as less accurate. Fortunately, it is possible to evaluate it immediately from $M(H)$ dependences (fig. 4.8), since the coefficient $-\frac{\Phi_0}{8\pi\mu_0\lambda^2}$ in (1.21) plays the role of a slope of the dependence and already contains λ. Extracted values of $\lambda(T)$ (fig. 4.10) were approximated by phenomenological relation (4.2) with parameters $a \approx 4.25$ and $b \approx 0.65$, which are close to two-fluid model parameters $a = 4$, $b = 0.5$ [3]. The fitting parameters are placed also directly in the main panel of fig. 4.10 for the sake of convenience.

$$\lambda(T) = \lambda_0 / \left[1 - \left(\frac{T}{T_c}\right)^a\right]^b . \tag{4.2}$$

The values of $H_{c1}(T)$ shown in the inset to fig. 4.10 were calculated by means of relation (1.13) using $\lambda(T)$ data from main panel of fig. 4.10. In that case $H_{c1}(T)$ data are well described by the parabolic-like equation:

$$\mu_0 H_{c1} = \mu_0 H_{c1}(0)\left[1 - \left(\frac{T}{T_c}\right)^2\right]. \tag{4.3}$$

Zero-temperature $H_{c1}(0)$ estimated as a result of approximation of newly evaluated $H_{c1}(T)$ dependence expressed two-times larger value with regard to $H_{c1}(0)$ obtained from low-field magnetization experiment and reached 102 mT.

It should be noticed here that $H_{c1}(0)$ can be also estimated by simply substituting of extrapolated value of $\lambda(0)$ (fig. 10) to relation (1.13). Calculated by last approach $H_{c1}(0)$ is of about 76.5 mT. That leads to discrepancy of about 25% between values of $H_{c1}(0)$ obtained by different approaches and points the ambiguity of extrapolations methods.

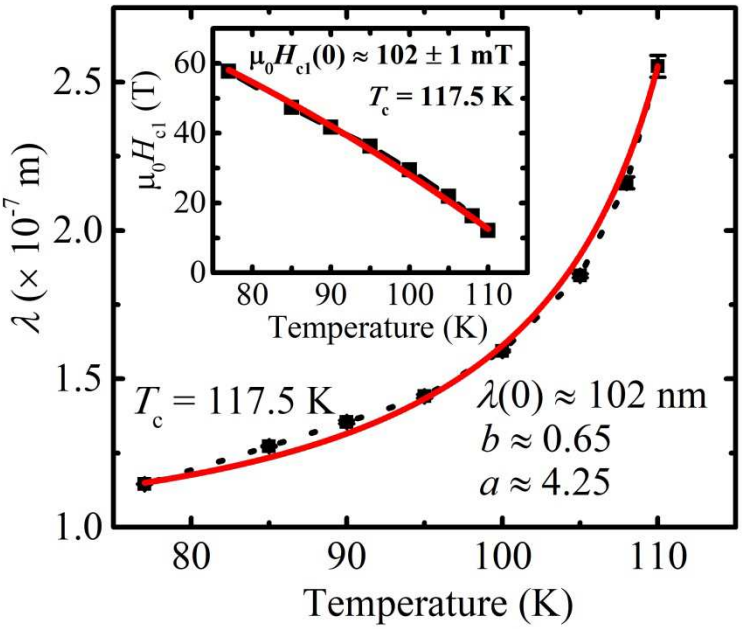

Figure 4.10. Calculated values of field penetration depth $\lambda(T)$ and related lower critical field $H_{c1}(T)$ (inset) by means of London approach to reversible magnetization (1.21) and relation (1.13) respectively. Red solid lines illustrate fitting, as described in the text. Fitted parameters are shown on corresponding figures. T_c was taken as fixed parameter during both fitting procedures. The results were published already [106].

Tab. 4.1 provides a comprehensive overview of the derived parameters for the investigated system.

Table 4.1. Measured and calculated superconducting state parameters of Cu-1234 system. Green color depicts parameters obtained from temperature dependence of magnetization, blue – from initial isothermal magnetization curves, brown – from high-field experiments.

T_c^{onset} (K)	$\mu_0 H_{c1}^*$ (5 K) (mT)	$\mu_0 H_{c1}$(5K) (mT)	λ (5K) (nm)	$\mu_0 H_{c1}(0)$ (mT)	λ (0) (nm)	$\mu_0 dH_{c2}/dT$ (T/K)	$\mu_0 H_{c2}$ (0) (T)	ξ (0) (nm)	$\mu_0 H_{c2}$ (77K) (T)
117. 5	0.5	44	138.7	102	102	–2.23	186	1.33	91

IV.3.2d. J_c and H_{irr} calculations

Aiming at evaluating of transport abilities of the material, required magnetization hysteresis loops were measured below the critical temperature T_c within the temperature range above liquid nitrogen temperature, specifically in a limited field range of [–1; 1] T (fig. 4.11a).

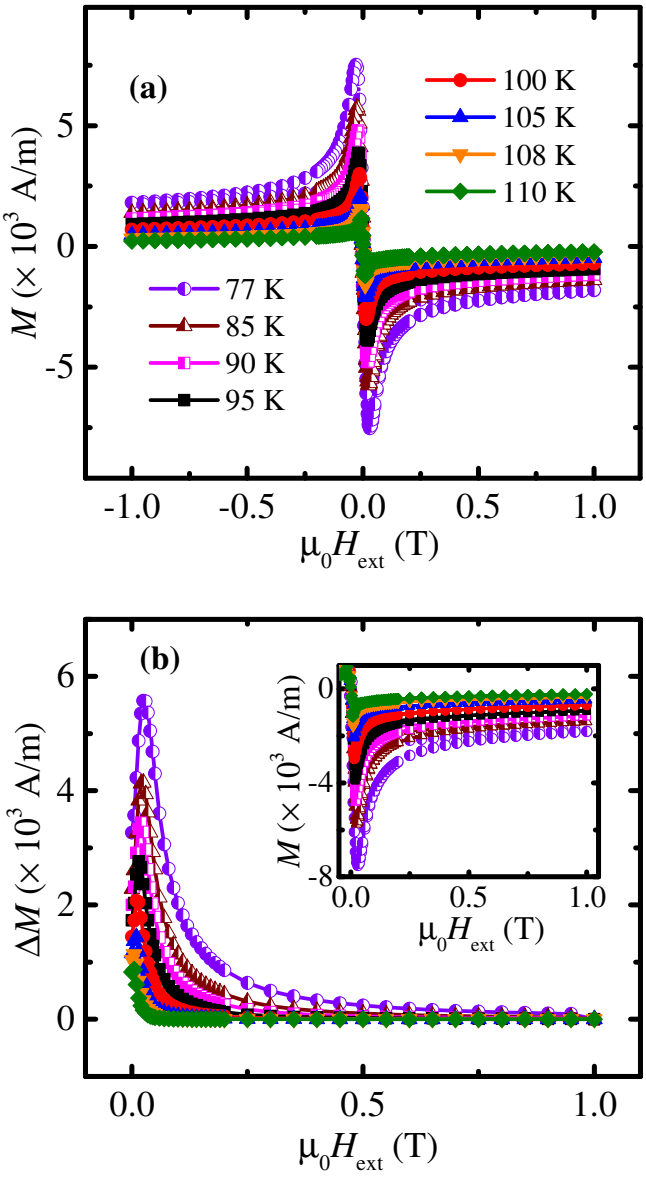

Figure 4.11. (a) Field dependences of magnetization recorded at following temperatures: 77 K – for violet half-filled circles, 85 K – brown half-filled triangles, 90 K – magenta half-filled squares, 95 K – black squares, 100 K – red circles, 105 K – blue triangles, 108 K – orange inverted triangles, 110 K – green rhombi, 112 K – violet stars. (b) Field dependences of ΔM obtained for corresponding temperatures. Inset shows the data, which were immediately used for $\Delta M(H_{ext})$ curves calculation. The results were published already [106].

Obtained magnetization values were represented in A/m units and analyzed from the perspective of the Bean's critical state model to determine the critical current density, j_c. For each isothermal curve, the corresponding parameter $\Delta M(H_{ext})$ was calculated (main panel, fig. 4.11b) as the difference between the ascending and descending branches of the magnetization-field dependence (inset, fig. 4.11b). According to the critical state model, the density of critical current is proportional to the width of the hysteresis loop (ΔM) [45], and expressed as (1.16).

In general, the parameter d is typically associated with the geometric size of the sample under investigation. However, in our particular case, d should be considered as the average grain size. This is because the hysteresis loops were measured at relatively high fields, where the grains are effectively decoupled based on previous observations (see IV.3.2a). Assuming an average grain shape approximated as a sphere, parameter $d = 2a$, where d is a diameter of a grain, hence a – radius.

Methodologically, grain radius can be evaluated by using the relation (applied e.g. here [116], [117]):

$$\frac{\chi}{\chi_{max}} = 1 - 3\frac{\lambda}{a}\coth\frac{a}{\lambda} + 3\frac{\lambda^2}{a^2}, \tag{4.4}$$

which describes loss of magnetization with diminishing of grain radius a to the value of field penetration depth λ and expressed as a ratio of dc susceptibilities. While χ_{max} is a maximal slope of magnetization via internal field $M(H_{int})$ curve recorded at 5 K and practically estimated from the Meissner line within the intergranular region of the curve (fig. 4.4a), χ – dc susceptibility of superconducting phase at intragranular regime – diamagnetic slope on fig. 4.5a estimated for 5 K magnetization dependence. In fact, the ratio χ/χ_{max} can be calculated experimentally as a dimensionless value of 0.588. By taking field penetration depth λ at 0 K as 102 nm (see tab. 4.1), estimated value of grain radius a is reaching 621 nm.

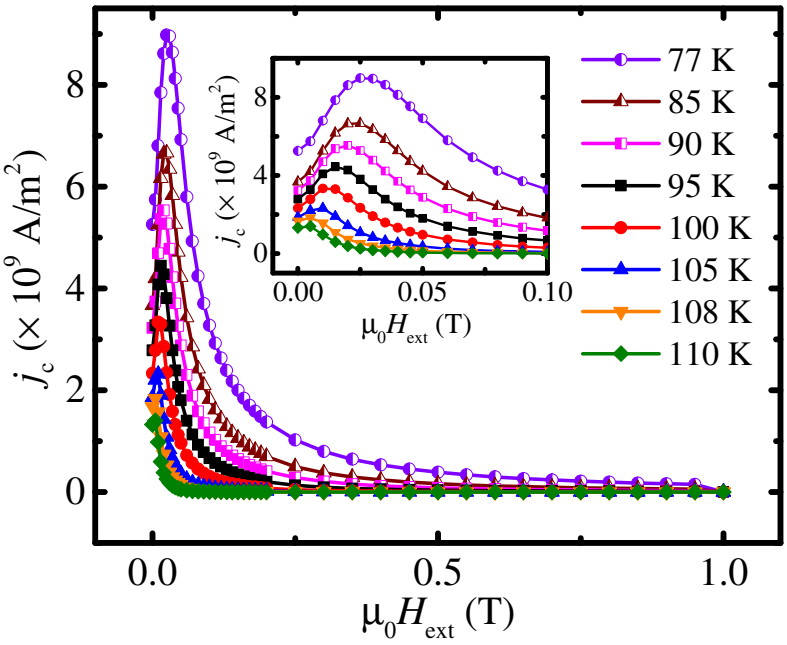

Figure 4.12. Field dependences of j_c obtained for corresponding temperatures: 77 K – for violet half-filled circles, 85 K – brown half-filled triangles, 90 K – magenta half-filled squares, 95 K – black squares, 100 K – red circles, 105 K – blue triangles, 108 K – orange inverted triangles, 110 K – green rhombi, 112 K – violet stars. Inset points out the presence of maximum on $j_c(\mu_0 H_{ext})$ curves. The results were published already [106].

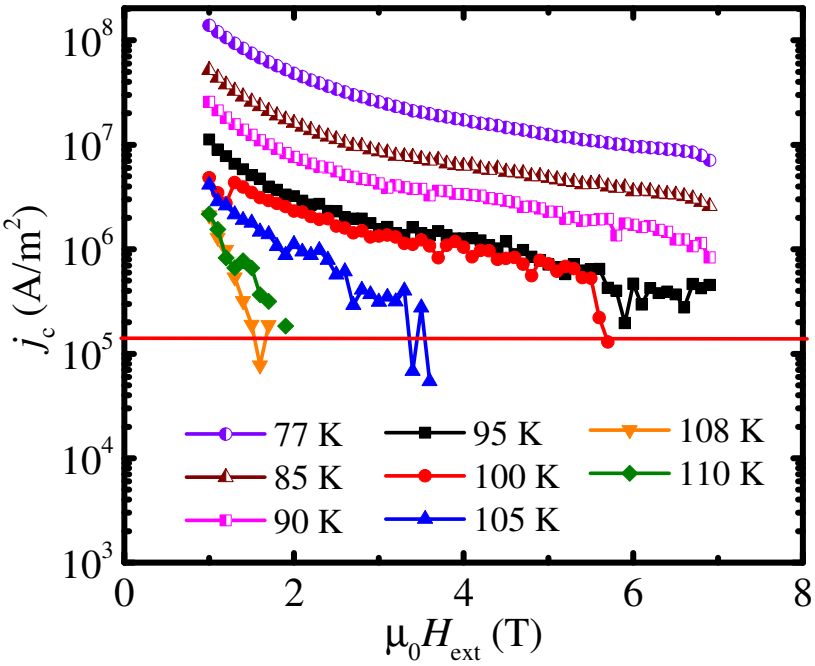

Figure 4.13. Field dependences of j_c calculated within the range of 1–7 T of external magnetic field H_{ext} and represented in semi-logarithmic scale. The legend is as same as for the previous figure. The results were published already [106].

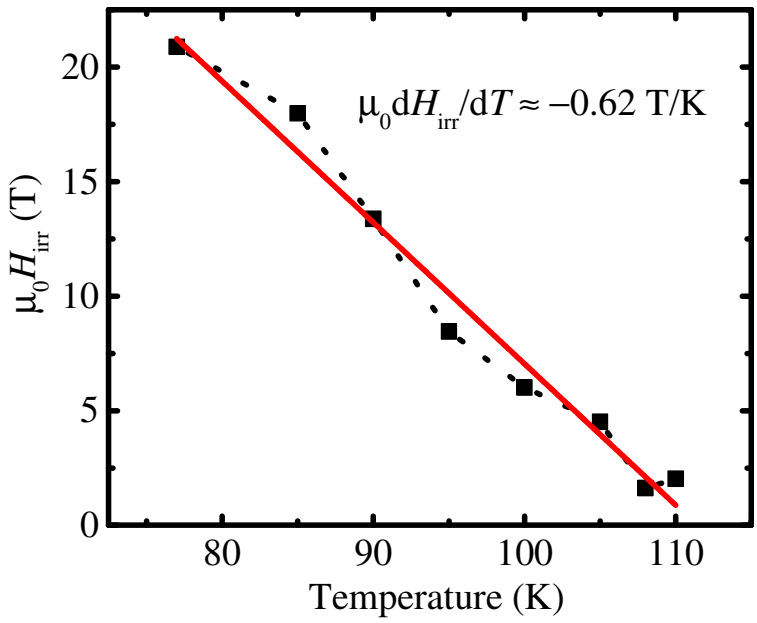

Figure 4.14. The irreversibility field line, calculated from high-field dependences of $j_c(H_{ext})$. The linear approximation (red line) of the dependence and its slope are depicted. The results were published already [106].

The critical current density j_c was calculated with regard to Bean's model from data presented on fig. 4.11 for corresponding temperatures and drawn as a function of external field H_{ext} as shown on fig. 4.12. The dependences express well-developed one-peak behavior with the maximum of rising magnitude on cooling. Simultaneously, peak shifts toward the higher fields. The maxima are formed from values of critical current density, which are sharply increased at first and fastly decay then. Although, a general appearance of $j_c(H_{ext})$ curves slightly resembles well-known fishtail character, the presence of maxima is related rather to shifting of the central peak of raw $M(H_{ext})$ hysteresis loops with regard to $\mu_0 H_{ext}$ axis. Such shift, probably, is a consequence of peculiarity of field distribution within the material due to sample shape and granularity as well [118], [119]. A rapid decrease of $j_c(H_{ext})$ after reaching the maximum indicates weak intragranular pinning abilities of investigating sample. That fact would be in a good agreement with narrow shape of hysteresis curves, which creates an optical illusion of low irreversibility field line. However, none of measured $j_c(H_{ext})$ curves exhibited crossing of field axis, i.e. the reaching of zero values. That's why in order to assess the irreversibility field line H_{irr}(T), the $j_c(H_{ext})$ dependences were obtained right up to 7 T, after measuring of $M(H_{ext})$ within the extended range of external dc field (fig. 4.13). The representation of resulting $j_c(H_{ext})$ curves in semi-logarithmic scale was used for the linearizing. As soon as the isothermal critical current densities remained relatively high values even at 7 T, criterion of 1.5×10^5 A/m^2 was utilized and $j_c(H_{ext})$ were linearly extrapolated up

to intersection with it (red benchmark on fig. 4.13). Gathered corresponding points of intersection were used to build the H_{irr}(T) (fig. 4.14). Obtained H_{irr}(T) diagram is of the magnitude, which far more exceeds expected from optical estimation, i.e. roughly by eye, from raw $M(H_{ext})$ data. The linear interpolation of scattered points of H_{irr}(T) gave the slope of the order of –0.62 T/K, which nonetheless much less than the slope of H_{c2}(T) ($\mu_0 dH_{c2}/dT \approx$ –2.23 T/K).

The validity of presented H_{irr}(T) calculations seem strongly limited by previously assessed $j_c(H_{ext})$. Since the $j_c(H_{ext})$ were estimated for a set of individual grains, the question of applicability of such approach for the entire material describing is rhetorical. As it was assumed above, granular material is constructed from high-quality superconducting part, i.e. grains itself, plus part of relatively poor superconducting properties – grain boundaries, through which grains are connected. Since such weak junctions are in fact different phase of substantial volume occupancy, grains from practical perspective can be treated as embedded in matrix. That's why if we consider transfer of superconducting charge carriers through the material as whole, $j_c(H_{ext})$ is overestimated and should be restricted in case of evaluation of the intergranular critical current density j_c^*, that corresponds to spatially averaged intergranular current density. Works of Chen et al. [120]–[122] thoroughly covered the issue of mutual cooperation of intra- and intergranular parts of a material, which is exposed to ac magnetic field. According to suggested scheme, critical current density can be calculated from temperature dependent imaginary component of ac susceptibility considering applied ac field H_{ac} and the loss peak position. Assuming that a loss peak happens when H_{ac} penetrates the center of a sample, j_c^* can be written as:

$$j_c^* = \frac{H_p}{x}, \tag{4.5}$$

where H_p is a field of full penetration, which equals to H_{ac} if we deal with the sample of square $2x \times 2x$ cross section in the direction perpendicular to applied ac field, x – half of geometrical dimension of cross section in the direction perpendicular to applied field. The necessary data of imaginary part $\chi''(T)$ were showed on fig. 4.3b. The results of j_c^* calculations are presented in tab. 4.2. Obtained values of j_c^* are at least of 4 orders lower than intragranular j_c for approximately same temperatures. Discussing the relation between j_c and j_c^* there should be emphasized the importance of application of different approaches, since both were calculated with some simplification. Although intragranular j_c gives general picture

of the behavior at high fields, utilizing of Bean's approach to its estimation is quite rough since the material is inhomogeneous. On the reverse side of the coin j_c^*, which gives more realistic quantitative vision and should reflect good enough a magnitude of transferring current through the sample, however the critical current obtained by transport measurements most likely turns out to be different. The causes of it consist in complicated percolation path of transport current, self-field influence and of course the nature of weak links, which can be metallic, insulating etc. [70].

Table 2. The values of critical current j_c^*, calculated from ac susceptibility measurements. T_m – temperature, which corresponds to the maximum on temperature dependence of out-of-phase component of ac susceptibility. H_p in that particular case is considered to be equal to applied ac field H_{ac}. The average geometrical size of the sample in the perpendicular to applied ac field direction: $2x \approx 4 \cdot 10^{-3}$ m.

H_p (A/m)	T_m (K)	j_c^* (kA/m^2)
8	110.5	4
80	103	40
160	98	80
240	94	120

Moreover, there were obtained evidences of vulnerability of such links to cyclic magnetization exposure. After the completion of magnetization measurements at high fields, there was proposed to repeat ac susceptibility experiment at the same conditions as in the description to fig. 4.3b. Nevertheless, peak on $\chi''(T)$ obtained at 0.3 mT of H_{ac} expressed drift to lower temperatures (fig. 4.15), which means that j_c^* obtained for 0.3 mT is no longer corresponds to T_m of 94 K. Concurrently, amplitudes of both $\chi''(T)$ and $\chi'(T)$ also reduced – a sign of worsening of shielding abilities. Such a degradation can be bounded with magnetostrictive properties of the sample and its intrinsic cracking after magnetizing at high dc field.

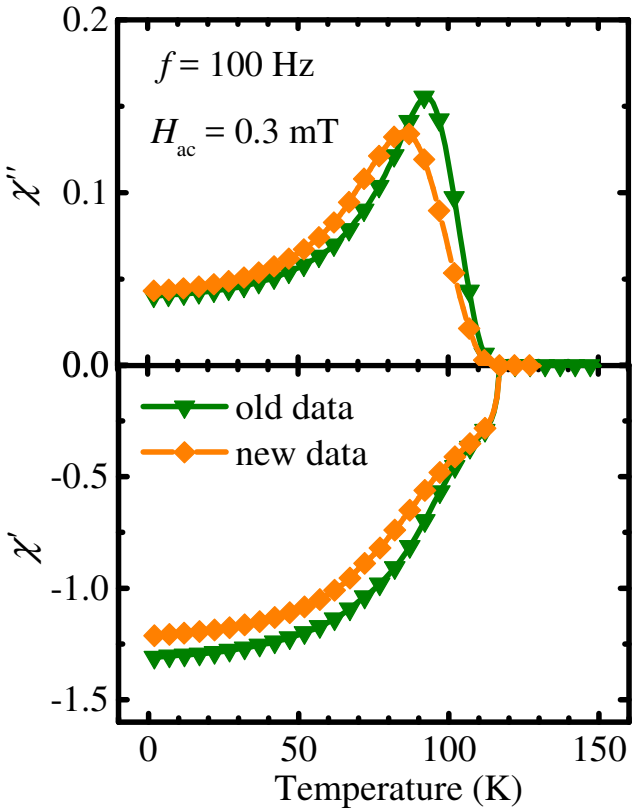

Figure 4.15. Temperature dependences of imaginary $\chi''(T)$ and real $\chi'(T)$ parts recorded at ac field by applying 0.3 mT of amplitude and 100 Hz of frequency. Green inverted triangles depict old data, orange rhombi – for new data.

IV.4. *Summary*

Obtained thermodynamic parameters of investigated sample are comparable to those of Cu-1234 family [111], [123], [124]: T_c is of about 117.5 K, H_{c2} and H_{irr} as high as 91 T and 21 T respectively at 77 K; which is in case of H_{irr} even higher than for related superconducting materials [125]. Moreover, intragranular critical current density j_c reached huge value of 5×10^9 A/m^2 at 77 K. In turn, large H_{c2} at 0 K of about 186 T, small related zero-temperature coherence length ξ of 1.33 nm and Ginzburg-Landau parameter κ of about 77 likely point out efficient pinning abilities of the material.

Nevertheless, it should be noticed that the nature of explored material is strongly inhomogeneous and practically can be considered as a combination of the influence of two subsystems: grains and grain boundaries, i.e. weak links. The origin of weak links can be explained from XRD study as the presence of incorporations of diamagnetic minor phases in the material, which can be a result of synthesis technique imperfection.

Despite the fact that the upper critical field line $H_{c2}(T)$ reached quite decent values and practically was estimated for set of individual grains, the narrow general pattern of hysteresis loops and calculated approximation of the experimental dependence of irreversibility field line point out that $H_{irr}(T)$ is much more lower than $H_{c2}(T)$. That stands for the existence of vortex liquid state (*unpinned state*) over a wide field range on the phase diagram. At the same time, H_{irr}(T) was assessed from intragranular critical current dependences $j_c(H_{ext})$ calculated by employing the Bean's critical state model and by considering circulating shielding currents on the grains.

The study of ac susceptibility allowed to track the dynamics of weak links behavior, which is related to imaginary (absorption) component $\chi''(T)$. Supposing that such dynamics correlates with values of flowing intergranular current, corresponding critical current density j_c^* was calculated and equaled to 2.9×10^5 A/m^2 at 77 K. Since j_c^* considers contribution of matrix (grain boundaries + inhomogeneities inclusions), which surrounds the grains, it can be treated as more close to transport critical current density comparing to j_c and turned out to be of 4 orders lower than j_c. Then, weak links factor is crucial in that type of material, since it strongly limits the transport abilities. Besides, degradation of the material was revealed from deterioration of measured values of j_c^*. The possibility of the influence of magnetostriction on integrity of the sample is supposed.

V. Superconducting state properties of intercalated $Li_x(C_2H_8N_2)(Fe_ySe_zS_{1-z})$ system

V.1. *Motivation*

V.1.1. What are IBSCs?

Iron-based superconductors (IBSCs) are investigated continuosly since superconductivity in pnictogen LaOFeP and $LaFeAsO_{1-x}F_x$ was found by Hosono group [21], [22]. The similarities to copper-based superconductors, i.e. cuprates, in terms of specific structure layering as well as peculiar co-existence of magnetic and superconducting phases [23], [24] and relatively high transition to superconducting state temperature T_c made IBSCs extremely attractive from scientific point of view and possibly promising for different applications [126]. Pure iron selenium $FeSe_{1-x}$, the most crystallographically simple among layered IBSCs, possesses the T_c of about 8 K [127], which can be drastically increased to 37 K by lattice geometry changing via applying high pressure [26], [27] or by chemical composition varying via substituting atoms in selenium sublattice [29]. Besides, the space between the FeSe layers is large enough for intercalation purposes. The last option opened a wide gate for plenty of synthesis techniques, which can be utilized for a layered material intercalation.

V.1.2 Why intercalated systems?

Intercalated 122-type of general composition $A_xFe_{2-y}Se_2$ (A – K, Rb, Cs, Rb/Tl, K/Tl) obtained by solid-state high-temperature reaction revealed T_c in the range 27–32 K depending on a type of intercalant [128]. However, enormous percentage of magnetic inhomogeneities, relatively low content of Meissner phase as well as mesoscale phase separation presence bring researches on low-temperature synthesis route. The biggest advantage of the last approach lies in sythesis conditions, which are far from phase separation area. A target material in such a case isn't obtained from a melted state, where all components are mixed together, but after chemical intercalation of parent compound in alkali/alkali-earth metal solution. It was reported co-intercalation of alkali/alkali-earth metal together with ammonia, alkali metal with plenty of different amines in iron selenium matrix [34], [129]. Apart from increasing of T_c to about 46 K, amount of screening fraction also was raised [33]. Nonetheless, weak crystallinity together with high risk of organic degradation under the air exposure make a challenge for their superconducting properties study.

Typically, probing of IBSCs by means of both magnetic moment and resistivity measurements provides comprehensive information about superconducting state. But specific character of organic intercalated FeSe morphology imposes additional limitations on transport measurements conducting. The magnetic moment measurements with regard to superconductors is a powerful instrument, which helps quilitatively estimate a presence of different phases and quantitatively define important parameters: transition temperature T_c, upper H_{c2} and lower H_{c1} critical fields. However, investigations of intercalated IBSCs don't go beyond the transition temperature (T_c) defining. Cause of it can be in magnetic inhomogeneities, which are still appeared in those materials.

Presented section is an attempt to obtain superconducting state parameters of intercalated FeSeS. In order to study superconducting properties magnetometry of both direct current (dc) and alternative current (ac) measurement techniques was applied.

V.2. *Synthesis and Measurements description*

The role of intercalant was played by cooperating alkali metal Li and ethylenediamine $C_2H_8N_2$ (for the sake of simplicity is also marked as EDA in the text). Choice of intercalant was dictaded strictly based on experimental results. It should be noticed though, that plenty of organic materials were tried as a dissolvent for Li. Nevertheless, only samples with co-intercalated Li-EDA showed more or less acceptable results from the perspective of magnetic measurements, i.e. showed distinct phase transition at relatively high temperatures.

V.2.1. Synthesis

The investigated intercalated materials were obtained within the three approaches of solvothermal method.

1) Intercalated materials were prepared by reacting iron chalcogenide polycrystalline precursors, which were synthesized separately using conventional solid-state methods (described elsewhere [130]), with aliquots of lithium metal dissolved in anhydrous ethylenediamine. The intercalation process was conducted for 48 hours at 40 °C in evacuated two-chamber Schlenk vessels filled with a 0.2 molar metal solution in the amine. Subsequently, the excess solution was decanted, and the samples were thoroughly washed with fresh anhydrous ethylenediamine until the filtrate became colorless. The samples were then vacuum dried for 30 minutes. After drying, the Schlenk vessels were opened in a glove bag filled with dry argon, and the resulting

intercalated black powders were transferred to airtight containers and sealed with Teflon.

2) For all of applied reactions synthesis was conducted in the airtight autoclave or Schottky bottle. Starting materials: elementary lithium, iron, selenium and sulfur along with NH_4Cl were weighted in molar ratio (given in tab. 5.1) under atmosphere of argon in glovebag and loaded in the autoclave/bottle along with 30 ml of anhydrous, dried under molecular sieves EDA. The reactor was tightly closed and taken out of the glovebag. Reaction was conducted at 160 °C for 14 days. Mixture was continuously stirred on the magnetic stirrer. After reaction, reactor was cooled to room temperature and transferred to the glovebag. Product was filtrated and washed with excess of EDA and dried for few minutes under dynamic vacuum (10^{-5} bar).
3) The steps were as same as for previous approach, but sulfur wasn't used as starting material, lithium nominally was taken two times more than iron and sulfur, the reaction was conducted at 180 °C for 7 days.

Table 5.1. The reactions, proportions of precursors and nominal chemical compositions. Violet color is for the samples synthesized by 1st approach, green – by 2nd, blue – by 3rd.

№	Proportion of starting materials	Reaction conditions	Nominal chemical composition of target material
1	Li:Fe:Se:S = 1:1:0.9:0.1	40 °C, 48 hours, EDA (0.2M solution)	$Li(EDA)(FeSe_{0.9}S_{0.1})$
2	Li:Fe:Se:S = 1:1:0.88:0.1	40 °C, 48 hours, EDA (0.2M solution)	$Li(EDA)(FeSe_{0.88}S_{0.1})$
3	Li:Fe:Se:S = 1:1:0.78:0.2	40 °C, 48 hours, EDA (0.2M solution)	$Li(EDA)(FeSe_{0.78}S_{0.2})$
4	$Li:Fe:Se:S:NH_4Cl$ = 1:1:0.95:0.05:1 + iron pieces	160 °C, 14 days, EDA (30 ml), stirring	$Li(EDA)(FeSe_{0.95}S_{0.05})$
5	$Li:Fe:Se:S:NH_4Cl$ = 1:1:0.85:0.15:1 + iron pieces	160 °C, 14 days, EDA (30 ml), stirring	$Li(EDA)(FeSe_{0.85}S_{0.15})$
6	$Li:Fe:Se:NH_4Cl$ = 2:1:1:1 + iron pieces	180 °C, 7 days, EDA (30 ml), stirring	$Li_2(EDA)(FeSe)$

The samples synthesized within the first approach will be marked as 1st subset in the text thereafter, within the second – as 2nd subset, within the third – as 3rd subset. Importantly, sample 6 from the 3rd subset was obtained without adding of sulfur and with double content of lithium (nominally), so it cannot be treated as a reference sample.

V.2.1. XRD technique

Bruker D8 Advance diffractometer with a Cu K_α (wavelength of 1.54060 Å) source was utilized to perform structural characterization and phase analysis. The room temperature measurements were realized in θ–2θ focusing conditions within the scan range of angles of 5–80 degrees. XRD spectrum was recorded with the step of 0.02 degree.

V.2.1. Magnetic measurements

Superconducting state properties were probed by means of Quantum Design Magnetic Property Measurement System (MPMS) *XL*7 with integrated Superconducting Quantum Interference Device (SQUID). All the measurements were carried out using Reciprocating Sample Option (RSO) regime, which yields the accuracy of about 10^{-8} emu and provides the low-frequency noise damping. The samples were packed under the vacuum conditions in quartz ampoules with a 5 mm diameter and a length of roughly 10 cm. They were held in place by two quartz cylinders that were each of about 5 cm length. The crystals' diameter was adjusted to match the quartz tube's inner diameter. Such a packing was utilized in order to prevent the investigated material from contact with atmosphere and subsequent degrading in air. A uniform environment for the studied crystals was provided by such sample mounting, which minimized amount of background signal during measurements.

A magnetic moment as a function of temperature was recorded subsequently during warming, in ZFC, and during cooling, in FCC, modes at fixed direct current (dc) magnetic field while measurements of field dependences of magnetic moment were performed at fixed temperatures after cooling at zero external dc magnetic field. Measurements of both real and imaginary part of ac susceptibility were performed in warming mode, i.e., with increasing temperature after cooling at zero dc field by applying oscillating magnetic field ac of specific H_{ac} and f. Where it was necessary superimposing of dc and ac fields was utilized.

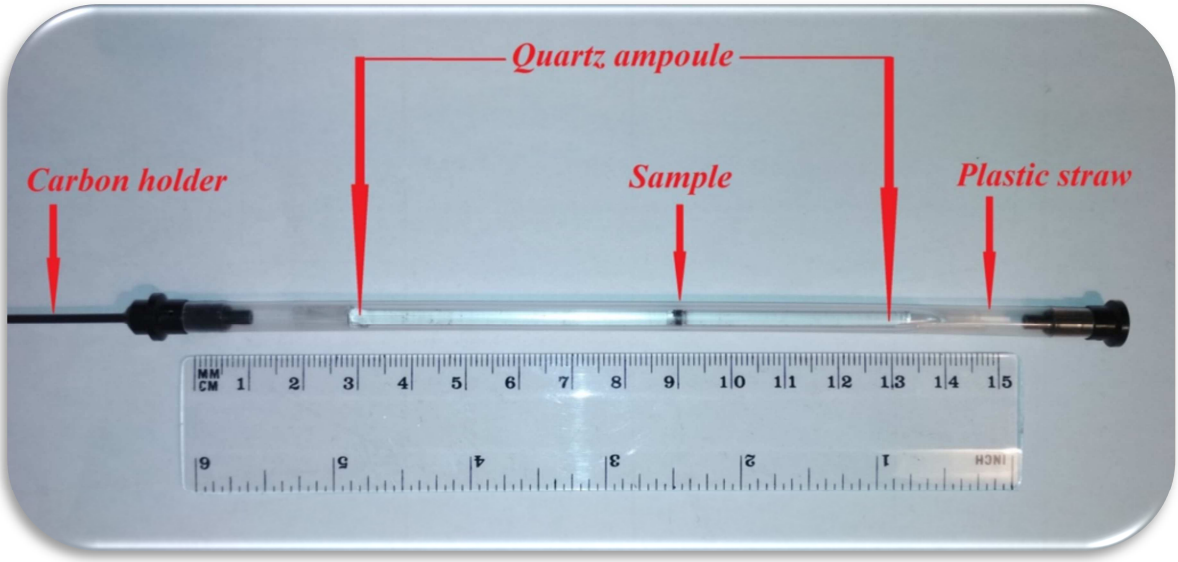

Figure 5.1. Mounting of ampoule packed intercalated sample for magnetic measurements.

V.3. *Results and discussion*

V.3.1. XRD results

XRD measurements were conducted for all of presented samples. Nevertheless, poor crystallinity of intercalated materials turned out to be a big barrier for exact identification of possible phases. More or less clean results were obtained for the sample Li(EDA)($FeSe_{0.88}S_{0.1}$) (fig. 5.2). Qualitative phase analysis of XRD spectrum conducted with regard to already obtained results [132] and using QualX software and Materials Project database revealed prevalence of the phase with $ThCr_2Si_2$ structure, i.e. with the space group of *I4*/*mmm*. The presence of body-centered tetragonal phase is usually associated with successfully realized intercalation. Hence, further probing of the material of Li_x(EDA)$Fe_{2-y}Se_2S_2$ is supposed. Obtained lattice parameters ($a = b = 3.42$ Å, $c = 20.81$ Å) were used for theoretical density calculation, which approximately equaled to 4.4–4.5 g/cm^3 depending on stoichiometry of the material. However, apart from dominant *I4*/*mmm* phase there were detected also: tetragonal FeSe with anti-PbO structure (known as β-FeSe [130], superconducting below the 8 K), hexagonal FeSe with NiAs structure (known as δ-FeSe [130], magnetic). Moreover, the reflection in the vicinity of $2\theta \approx 25.5$ degree may belong to Li_2Se phase with fluorite structure. That phase is non-magnetic itself, but can be a sign of the presence of small clusters formed by pure Fe [33], which weren't detected by the XRD technique though. Hence, the existence of magnetic inhomogeneities in the investigated material is supposed already from the XRD results. However, it is important to emphasize that

the peak assigned to Li_2Se can be also a trace of base-centered orthorombic *Amma* phase of $Li_x(EDA)Fe_{2-y}Se_2S_2$ [134]. That fact hints on ambiguity of XRD results interpretation.

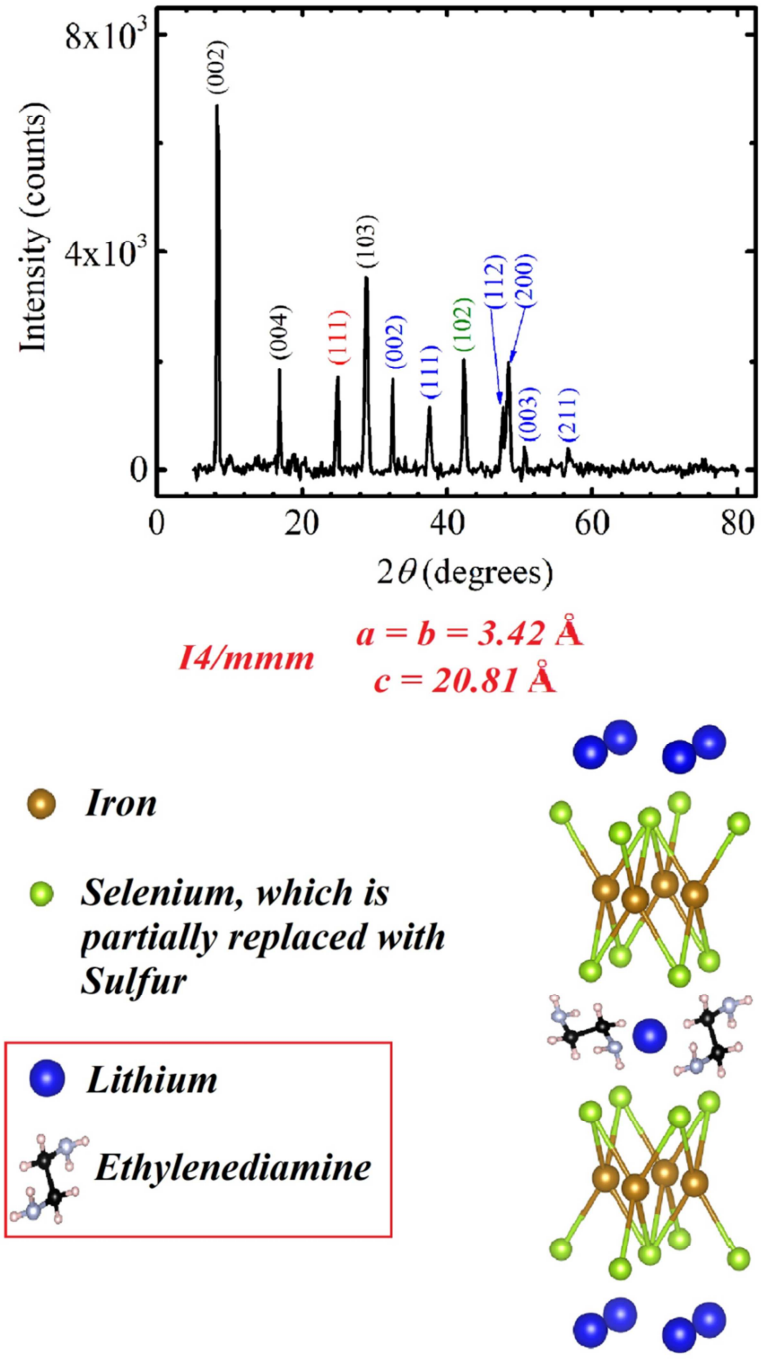

Figure 5.2. Upper panel – results of XRD measurements of $Li(EDA)(FeSe_{0.88}S_{0.1})$; the *hkl* indices of specific color are placed directly on the top of each peak as follows: black – for target $Li_x(EDA)Fe_{2-y}Se_2S_2$ phase, red – for Li_2Se, blue – for tetragonal FeSe, green – for hexagonal FeSe. Lower panel – tentative crystal structure of target intercalated material, which is reproduced by using crystallography materials database. Scaling of Li, Fe, Se sizes were taken from atomic size perspective. Since the structure wasn't solve, positions of lithium and EDA are rather schematic.

V.3.2a. Magnetometry results – dc measurements

In order to reveal the transition to superconducting state two types of preliminary measurements were conducted: magnetic moment as a function of temperature in ZFC and FCC conditions at 1 mT of external dc magnetic field as well as magnetic moment via small external dc field at the temperature as high as 2 K (fig. 5.3).

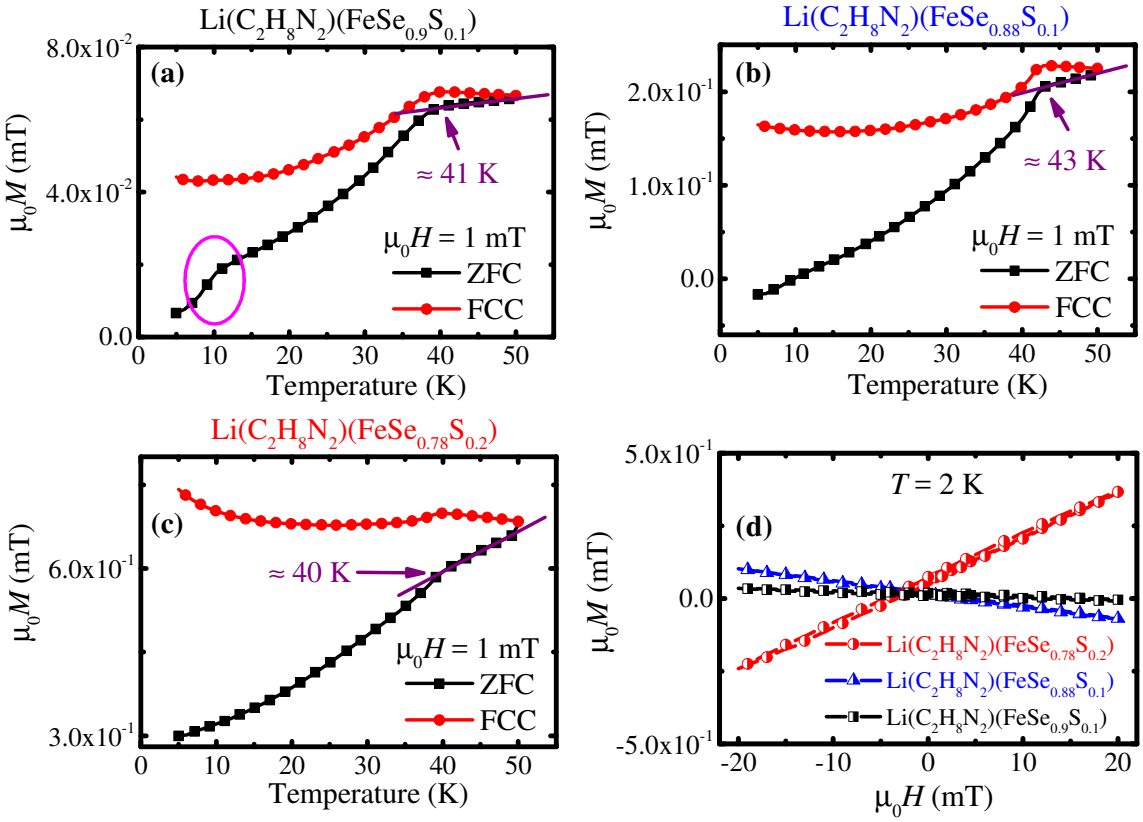

Figure 5.3. A magnetization as a function of temperature recorded in ZFC–FCC mode for: (a) $Li(C_2H_8N_2)(FeSe_{0.9}S_{0.1})$, (b) $Li(C_2H_8N_2)(FeSe_{0.88}S_{0.1})$, (c) $Li(C_2H_8N_2)(FeSe_{0.78}S_{0.2})$. Panel (d) shows the dependence of magnetization on external dc field.

A measured magnetic moment was converted to magnetization value and presented thereafter in SI [mT] units. Temperature dependences of magnetization clearly showed thermomagnetic irreversibility, which is quite typical behavior for FeSe intercalated with alkali atoms Li/Na and ammonia/amines [131], [132]. The most striking thing about the results presented in fig. 5.3a–5.3c is simultaneous presence of distinct transition point for all samples together with strong positive magnetization value. In fact, ZFC and FCC temperature curves show that only $Li(C_2H_8N_2)(FeSe_{0.88}S_{0.1})$ reached diamagnetic signal. A large positive magnetic moment, which is apparently generated by magnetic inhomogeneities and tending to mask superconducting phase existence is a characteristic feature of investigated materials. Moreover, the magnetic field dependences (fig. 5.3d) confirmed an ambiguous nature of

studied system: for the sample $Li(C_2H_8N_2)(FeSe_{0.9}S_{0.1})$, which has positive magnetization value even at the low temperatures (fig. 5.3a), diamagnetic behavior on field curves was detected. The onset of transition to superconducting state was defined from ZFC temperature dependences as a point where curve deviates from the straight line, which in turn is supposed to be a signature of phase transition. The values of T_c^{onset} depicted in fig. 5.3a–5.3c are in consistency with data obtained for relative materials [132]–[134]. Besides, the second curvature on ZFC in the vicinity of $T_c' \approx 10$ K for $Li(C_2H_8N_2)(FeSe_{0.9}S_{0.1})$ is clearly seen (fig. 5.3a), which is evidently a sign of pure FeSe or FeSeS phase presence, since the T_c of FeSeS is of about 8–10 K depending on stoichiometry [135]. It is worth to notice that sharpness of the transition to superconducting state is gradually decreased with the change of stoichiometry. The sample with nominal composition of $Li(C_2H_8N_2)(FeSe_{0.9}S_{0.1})$ has more sharp one compare to those with excessive content of iron: $Li(C_2H_8N_2)(FeSe_{0.88}S_{0.1})$ and $Li(C_2H_8N_2)(FeSe_{0.78}S_{0.2})$. The last one also contains bigger amount of sulfur and the weakest signal from superconducting phase.

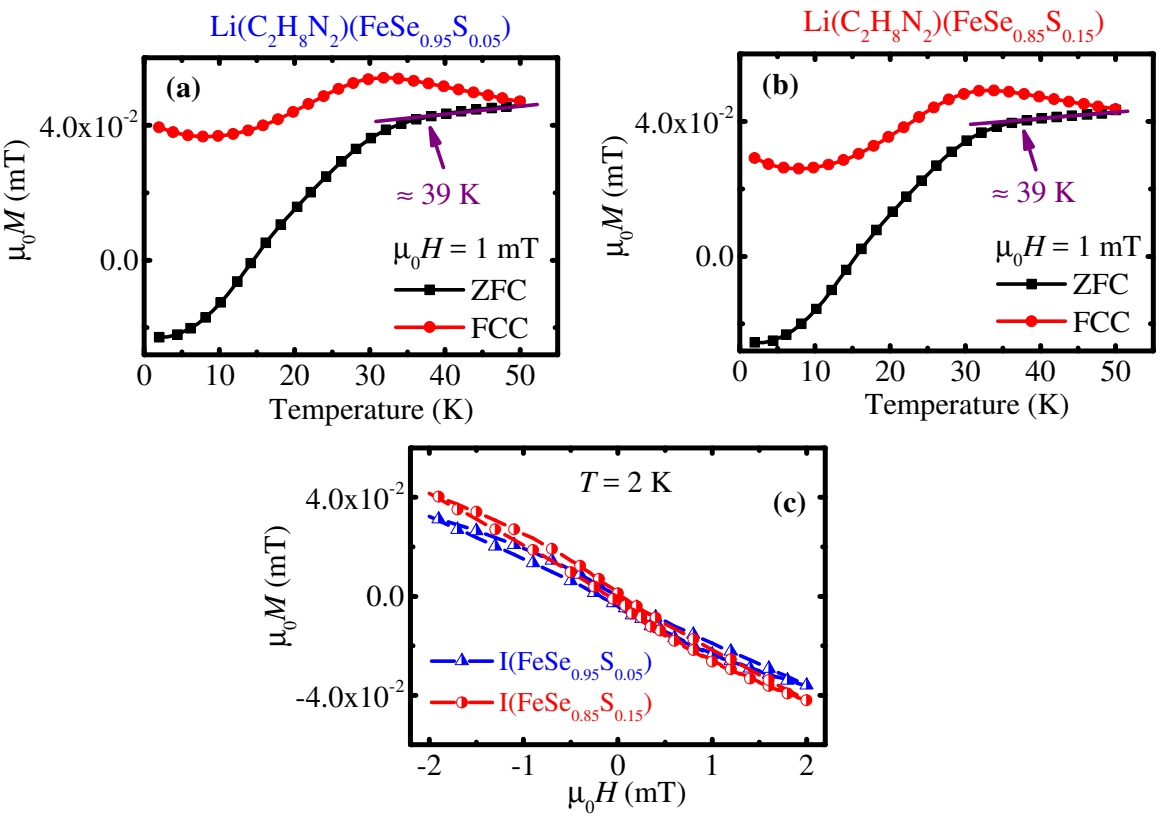

Figure 5.4. A magnetization as a function of temperature recorded in ZFC–FCC mode for: (a) $Li(C_2H_8N_2)(FeSe_{0.95}S_{0.05})$, (b) $Li(C_2H_8N_2)(FeSe_{0.85}S_{0.15})$, (c) $Li_2(C_2H_8N_2)(FeSe)$. Panel (d) shows the dependence of magnetization on external dc field, I – indicates intercalant – $Li(C_2H_8N_2)$.

Dc measurements of the 2nd subset as well as T_c^{onset} estimation were done in a way described above. The results are presented in fig. 5.4. A general appearance of temperature dependences of magnetization for samples $Li(C_2H_8N_2)(FeSe_{0.95}S_{0.05})$ and $Li(C_2H_8N_2)(FeSe_{0.85}S_{0.15})$ shown in figs. 5.4a–5.4b is much similar to each other than to that measured for samples with close stoichiometry but obtained by means of different synthesis route, i.e. from the 1st subset (see fig. 5.3). Despite a pronounced ZFC–FCC bifurcation, achieved negative values of magnetization indicate real shielding properties, i.e. all of the samples from the 2nd subset showed diamagnetic signal at the temperature of 2 K (fig. 5.4c).

While $Li(C_2H_8N_2)(FeSe_{0.95}S_{0.05})$ and $Li(C_2H_8N_2)(FeSe_{0.85}S_{0.15})$ appear rather like „twins", $Li_x(C_2H_8N_2)(Fe_ySe_z)$ with a double nominal content of lithium (x:y:z = 2:1:1) shows drastically different superconducting properties. Since the ZFC–FCC dependences start to diverge significantly at the temperatures lower than T_c^{onset} and taking into account diamagnetic character of both ZFC–FCC curves at the temperature range of 2–30 K, there can be supposed domination of superconducting phase in the sample (fig. 5.5).

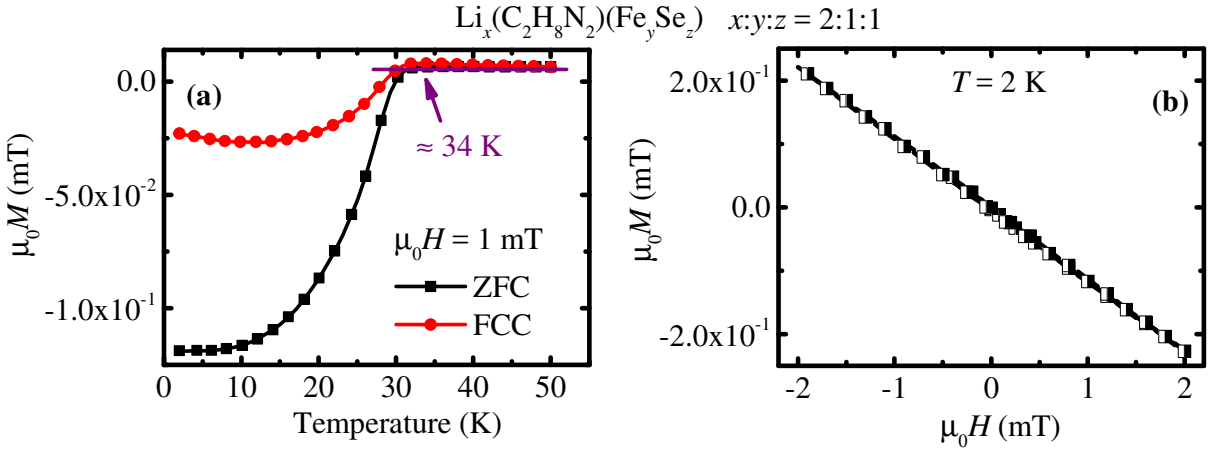

Figure 5.5. (a) Temperature dependences of magnetization measured at 1 mT of H_{ext} for $Li_2(C_2H_8N_2)FeSe$. (b) Minor hysteresis loop recorded at 2 K.

However, slight bifurcation between ZFC and FCC at the temperature range higher than T_c^{onset} as well as a visible curvature of FCC dependence at low temperature hint at the magnetic phase presence. The amount of superconducting volume fraction of $Li_2(C_2H_8N_2)(FeSe)$ attained a value of 14% at 2 K. The calculation was carried out without taking the demagnetizing effect into account and based on the assumption that a perfect superconductor in the Meissner state has a magnetic susceptibility equal to –1. For FeSe intercalated with $C_2H_8N_2$ molecules close values of critical temperature T_c and general pattern

of temperature dependences of magnetization was obtained in [136], [137]. The results of preliminary measurements are summarized in tab. 5.2.

Table 5.2. Defined transition temperatures T_c by means of dc technique. T_c' indicates the value of transiton temperatures of presented secondary phase.

№	Chemical composition	T_c^{onset}, K	T_c', K
1	$Li(EDA)(FeSe_{0.9}S_{0.1})$	41	10
2	$Li(EDA)(FeSe_{0.88}S_{0.1})$	43	—
3	$Li(EDA)(FeSe_{0.78}S_{0.2})$	40	—
4	$Li(EDA)(FeSe_{0.95}S_{0.05})$	39	—
5	$Li(EDA)(FeSe_{0.85}S_{0.15})$	39	—
6	$Li_2(EDA)(FeSe)$	34	—

There should be noted that apart from $Li_2(C_2H_8N_2)(FeSe)$ (fig. 5.5) all of measured samples possess quite small zero-temperature lower critical field H_{c1} – close to zero in fact. The effect is shown good enough on the ZFC curves, which exhibit significant enhance of magnetization already in low-temperature range. That indicates the easy penetration of the material's inner space by a magnetic field, since the ZFC dependences were recorded at small dc field of 1 mT. And that's why low-temperature flattening on ZFC magnetization curve for $Li_2(C_2H_8N_2)(FeSe)$ was supposed as a consequence of non-zero measurable H_{c1}.

The lower critical field $H_{c1}(T)$ for $Li_2(C_2H_8N_2)(FeSe)$ was studied from the set of magnetization via external field curves as points of deviation from linear diamagnetic behavior. Such points indicate the moment of penetration of the sample with a magnetic field in the form of Abrikosov vortices. To make a procedure of deviation points picking up more clear, signal from a Meissner state was subtracted and the square root of resulting magnetization drawn as it is illustrated with the inset to fig. 5.6. Such a procedure is very similar to described in [65]. Zero-temperature $H_{c1}(0)$ was estimated by the approximation of $H_{c1}(T)$ with the parabolic-like equation (4.3) and equals to 0.7 mT as it is presented in fig. 5.6.

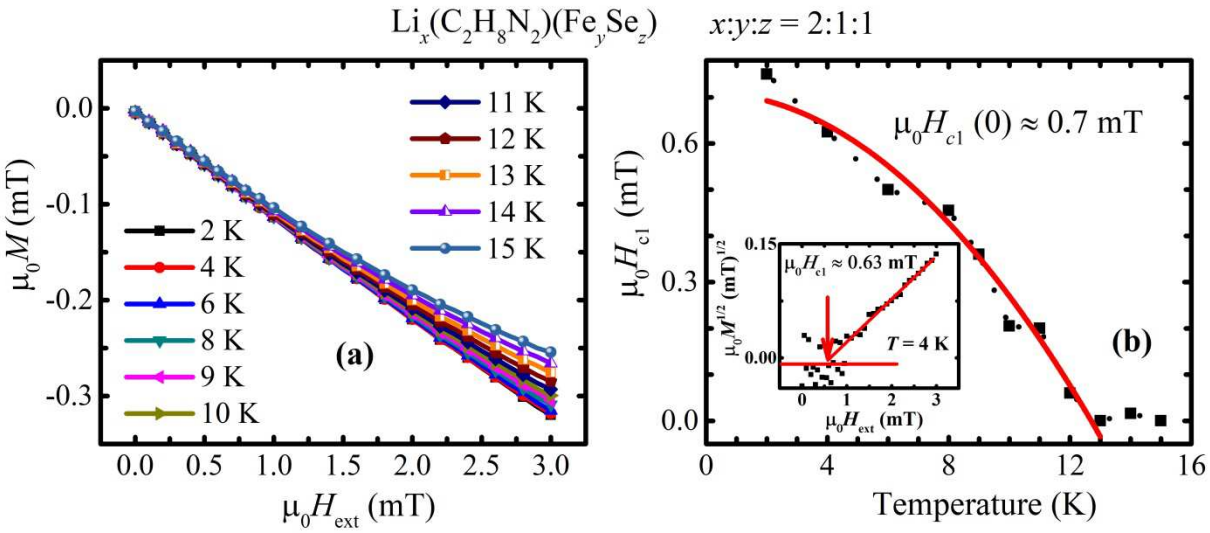

Figure 5.6. (a) Isothermal field dependences of magnetization obtained for Li_2(EDA)FeSe, the magnetization is represented as a function of applied dc field H_{ext}. (b) Phase diagram of the lower critical field H_{c1} represented as a function of temperature. The inset depicts an example of the procedure of defining the point where field dependence of magnetization deviates from diamagnetism – measurement was conducted at 4 K.

V.3.2b. Magnetometry results – ac measurements

In order to obtain the upper critical field H_{c2} ac susceptibility measurement technique was utilized. The ac susceptibility as a function of temperature for the 1st subset was measured in superimposed ac and dc fields. The parameters of applied ac field were chosen experimentally and supposed as optimal. Meanwhile, several bias dc fields up to 7 T were utilized.

The results of ac susceptibility investigations for the 1st subset are presented in figs. 5.7–5.9. Several common features in ac susceptibility behavior should be noticed. At first, transition to superconducting state which is revealed from the real part as well as a loss peak on the imaginary part gradually shift to lower temperature with dc field increase. Secondly, real part curve falls along the susceptibility axis with dc field increase and susceptibility values itself tend to become more negative. Meanwhile, the amplitude of the transition to superconducting state decreases which in turn indicates a degradation of shielding properties. Thirdly, minor hump on the real part and double loss peak on the imaginary part point out another phase presence. Since a second hump occurs within the temperature of 8–10 K there was supposed that it comes from FeSe/FeSeS phase, i.e. from matrix. The effect is clearly seen on dependences recorded at bias dc field up to 0.05 T.

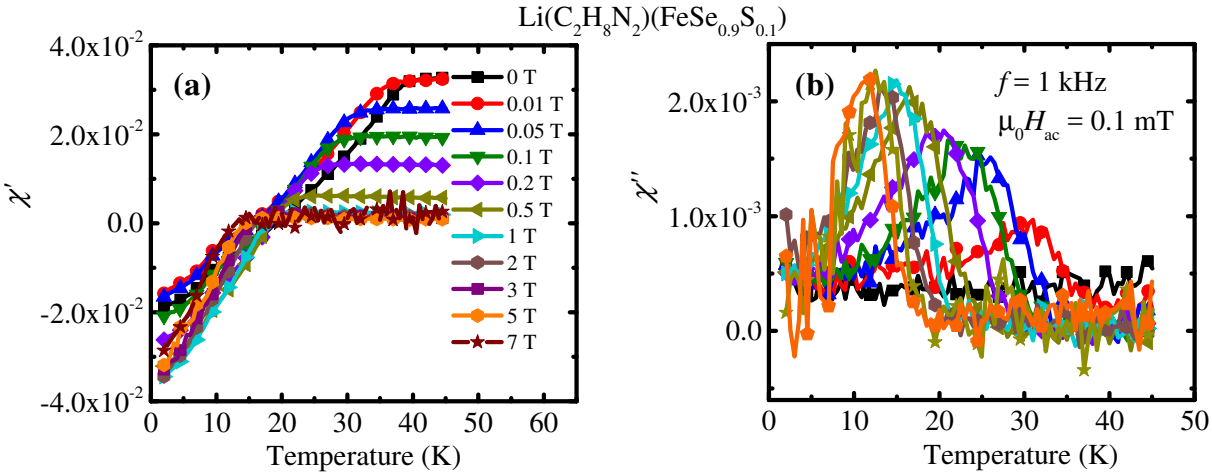

Figure 5.7. (a) A real part and (b) an imaginary part of ac susceptibility measured in dc bias field for $Li(C_2H_8N_2)(FeSe_{0.9}S_{0.1})$.

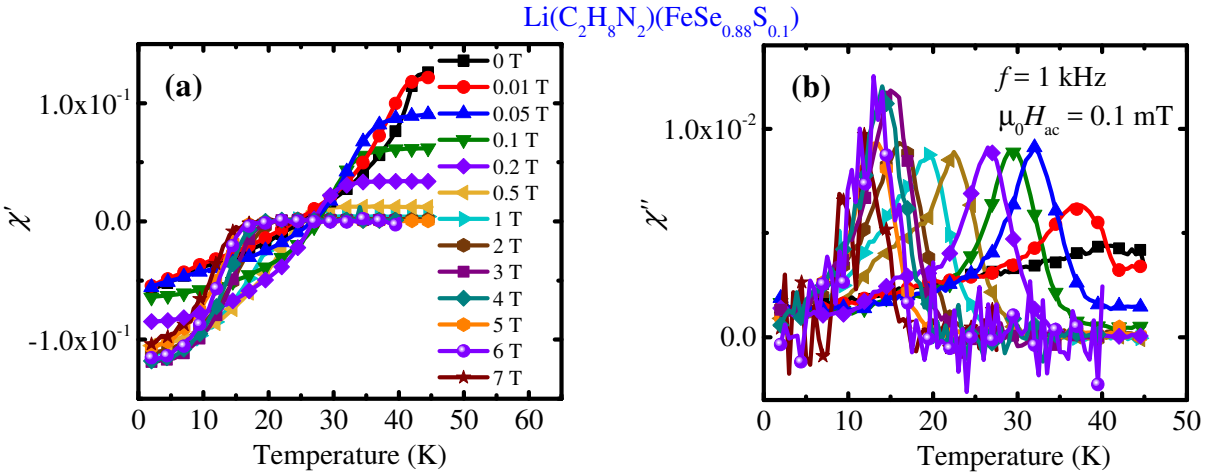

Figure 5.8. (a) A real part and (b) an imaginary part of ac susceptibility measured in dc bias field for $Li(C_2H_8N_2)(FeSe_{0.88}S_{0.1})$.

The common general character of the real part of ac susceptibility comes from highly inhomogeneous nature of the material. The positive values of in-phase component indicate magnetic phase existence. It is important to emphasize, that the ac measurements confirmed an important role of the stoichiometry influence on properties of a final product, which was obtained within the same synthesis framework. That was already suspected from ZFC–FCC study, i.e. iron-rich samples $Li(C_2H_8N_2)(FeSe_{0.88}S_{0.1})$ and $Li(C_2H_8N_2)(FeSe_{0.78}S_{0.2})$ demonstrate worse superconducting properties: smeared transition to superconducting state and small shielding fraction content.

Interestingly, $Li(C_2H_8N_2)(FeSe_{0.78}S_{0.2})$ at small bias dc field didn't reveal a diamagnetic nature at all, only tending to reach superconducting state. More typical behavior

of superconductors in superimposed ac-dc fields [67], [138], [139] $Li(C_2H_8N_2)(FeSe_{0.78}S_{0.2})$ started to show at the bias dc field higher than 1 T (fig. 5.9a). Besides, the supremacy of the low temperature loss peak which is come from FeSeS compare to high temperature one at the bias dc field up to 0.5 T is observed (fig. 5.9b). In fact, $Li(C_2H_8N_2)(FeSe_{0.78}S_{0.2})$ possesses highly inhomogeneous nature both from magnetic and superconducting sides of the material.

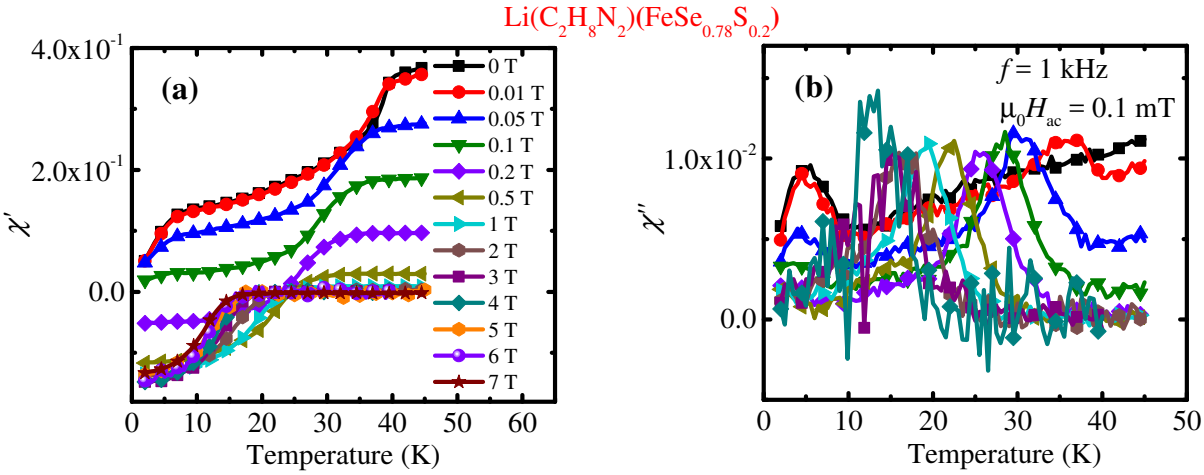

Figure 5.9. (a) A real part and (b) an imaginary part of ac susceptibility measured in dc bias field for $Li(C_2H_8N_2)(FeSe_{0.78}S_{0.2})$.

The ac susceptibility of $Li(C_2H_8N_2)(FeSe_{0.95}S_{0.05})$ and $Li(C_2H_8N_2)(FeSe_{0.85}S_{0.15})$ was studied in the similar way as for above 1st subset with the only difference: in order to avoid high-frequency noises and to catch transition points clearly it was decided to apply ac field with lower frequency of 0.1 kHz. With the purpose to verify if the frequency change affects on the transition point on real part of ac susceptibility curve, measurements were done also by utilizing of ac field of 1 kHz of frequency.

Shifting of the inflection on the real part dependence (fig. 5.10a–5.10b) with frequency change can be a signature of spin-glass state. In our case the transition point on the real part of ac susceptibility shifts toward higher temperatures. That effect was already described for iron-based superconductors and may be related to short-range spin-density wave (SDW) presence [140]. Since the spin-glass state is produced among other things by frustrated spins, it is logically correct to suspect co-existence of several competetive magnetic phases in the material. Nevetherless, there are also evidences, that such an effect can be a consequence of a thermally-activated flux motion [69]. Fig. 5.10c clearly illustrates the appearance of high-frequency noise under the ac field of 1 kHz of frequency. A tremendous spikes would be a huge obstacle during further analysis.

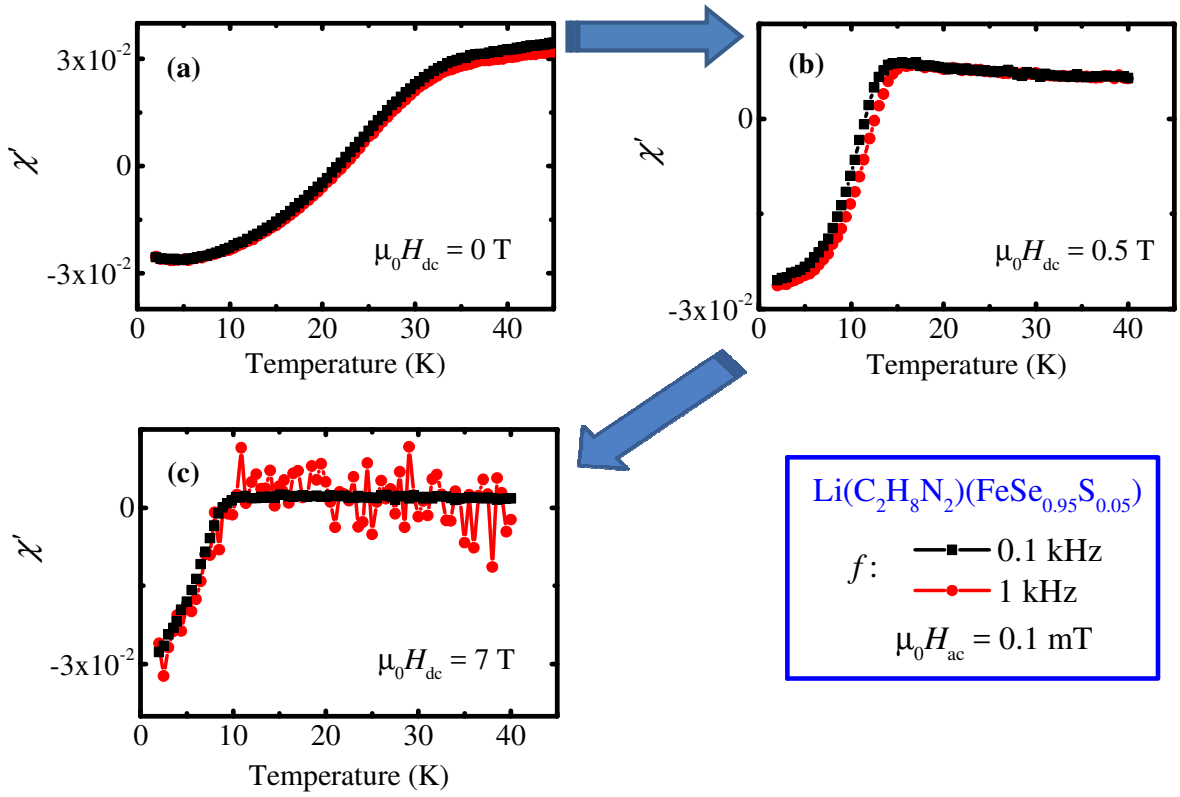

Figure 5.10. An evolution of the real part of ac susceptibility with increase of frequency of ac field for $Li(C_2H_8N_2)(FeSe_{0.95}S_{0.05})$. Results depicted on (a), (b), (c) – recorded at 0, 0.5, 7 T of bias dc field respectively.

Quite similar ac susceptibility dependences were obtained for both $Li(C_2H_8N_2)(FeSe_{0.95}S_{0.05})$ and $Li(C_2H_8N_2)(FeSe_{0.85}S_{0.15})$ samples (fig. 5.11). At first glance the in-phase component demonstrates a uniform transition since there is no jump in the vicinity of 8 K and the out-of-phase component expresses single loss peak character. But when we look closer at the real part curves we can notice an additional bendings on curves recorded at dc bias fields of 0.01 and 0.05 T (fig. 5.12). Results of the real part measurements in fig. 5.11 correlate with those obtained for the 1st subset since the presence of magnetic inhomogeneities was detected. The difference lays in a sharpness of the transition to superconducting state, which is evidently sharper for $Li(C_2H_8N_2)(FeSe_{0.95}S_{0.05})$ and $Li(C_2H_8N_2)(FeSe_{0.85}S_{0.15})$ samples.

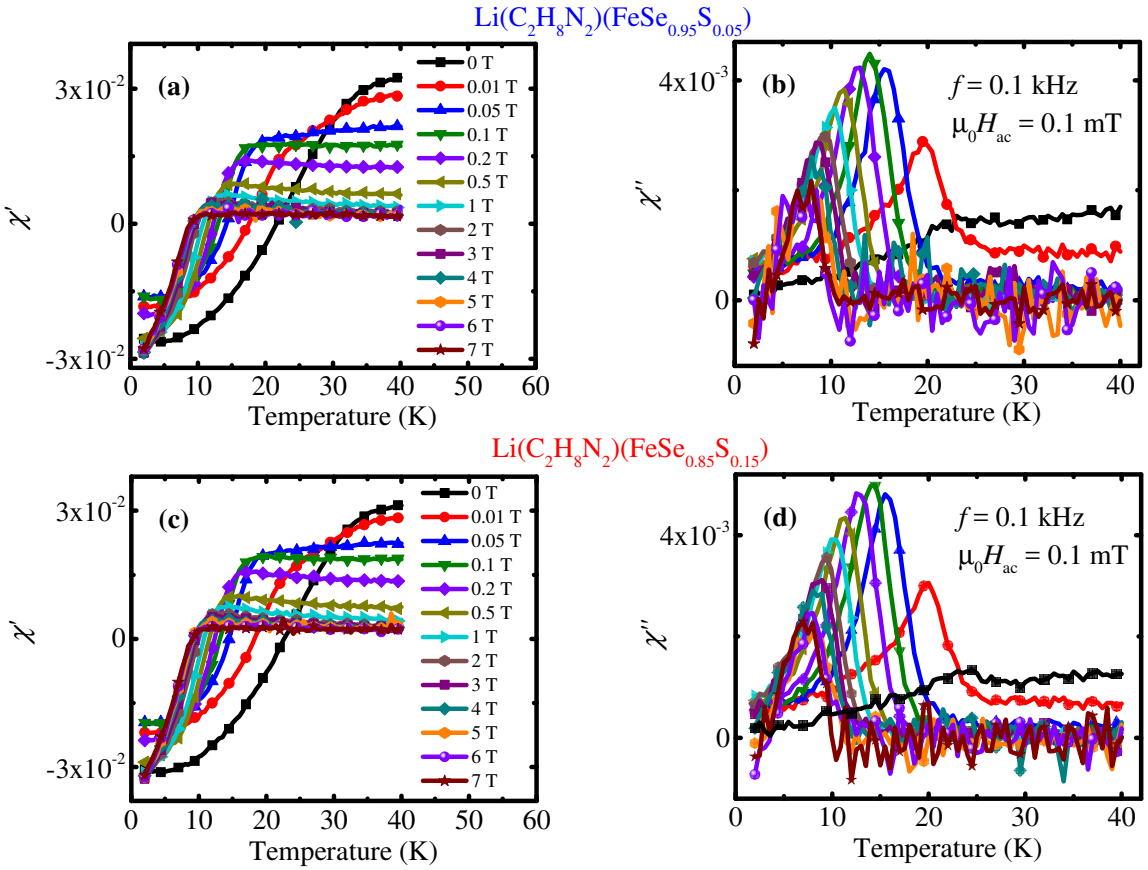

Figure 5.11. The real and imaginary parts of ac susceptibility recorded at 0.1 kHz of frequency with 0.1 mT of ac field amplitude for samples $Li(C_2H_8N_2)(FeSe_{0.95}S_{0.05})$ – (a), (b) and $Li(C_2H_8N_2)(FeSe_{0.85}S_{0.15})$ – (c), (d).

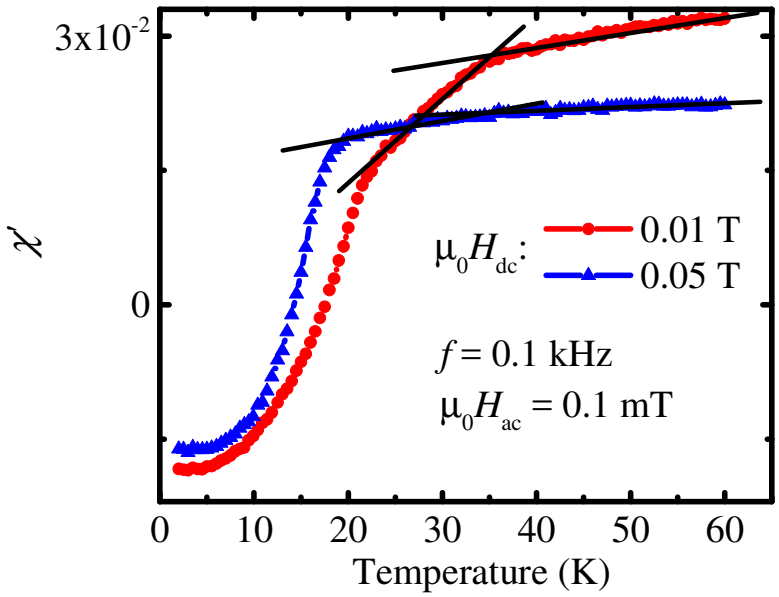

Figure 5.12. A real part of ac susceptibility measured at 0.01 T (red circles) and 0.05 T (blue triangles) of dc field for $Li(C_2H_8N_2)(FeSe_{0.95}S_{0.05})$. The results are also valid for $Li(C_2H_8N_2)(FeSe_{0.85}S_{0.15})$.

Besides, loss peak behavior is organized in absolutely other way. A peak goes to lower temperatures with dc field increasing while its amplitude grows until the 0.1 T of dc field is reached. Then peak amplitude gradually decreases at bias fields of 0.2 T up to 7 T.

The ac susceptibility of the sample from 3rd subset was measured in superimposed ac and dc fields as for above investigated. The conditions were as same as for the 1st subset, i.e. ac field of 1 kHz of frequency and with 0.1 mT of amplitude was applied (fig. 5.13). The range of external dc field remained unchanged. Remarkably for that type of composition is a demonstration of almost typical picture for ac susceptibility of superconductors placed in superimposed fields, i.e. possession of zero signal at the temperatures higher than T_c^{onset} together with gradual decreasing of the amount of shielding fraction while the dc field is raised [73], [75], [141]. Those dependences, which were recorded at 0.05, 0.1 and 0.2 T clearly revealed the double curvature within the range of 10–30 K on the real part of ac susceptibility and two peaks on the corresponding imaginary part. The effect is similar to that, which was obtained for described samples (fig. 5.11, 5.12).

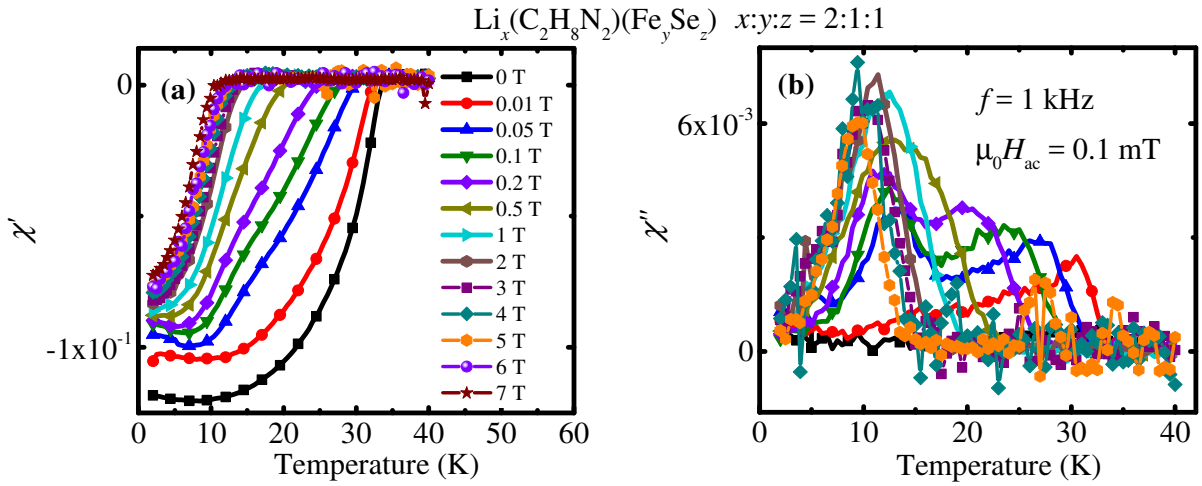

Figure 5.13. (a) A real part and (b) an imaginary part of ac susceptibility measured in dc bias field for $Li_2(C_2H_8N_2)(FeSe)$.

Both loss peaks are shifting equally and the amplitude of low-temperature one doesn't grow. Nevertheless, a conventional effect of the influence of weak links cannot be excluded from consideration. However, probably it is not related to the trace from parent FeSe compound as well, because low-temperature peak is not reached the vicinity of T_c^{onset} of FeSe.

V.3.2c. H_{c2} defining

In order to obtain phase diagrams in terms of the upper critical field as a function of temperature $H_{c2}(T)$, the results of ac susceptibility measurements were processed. Values of T_c^{onset} and corresponding values of H_{c2} were extracted from the real part of ac susceptibility. Methodologically, values of T_c^{onset} were defined exactly as described in section II.2 and depicted in fig. 5.3 for dc experiment. $H_{c2}(T)$ phase diagrams are shown in fig. 5.14 for the 1st and fig. 5.15 2nd and 3rd subsets respectively.

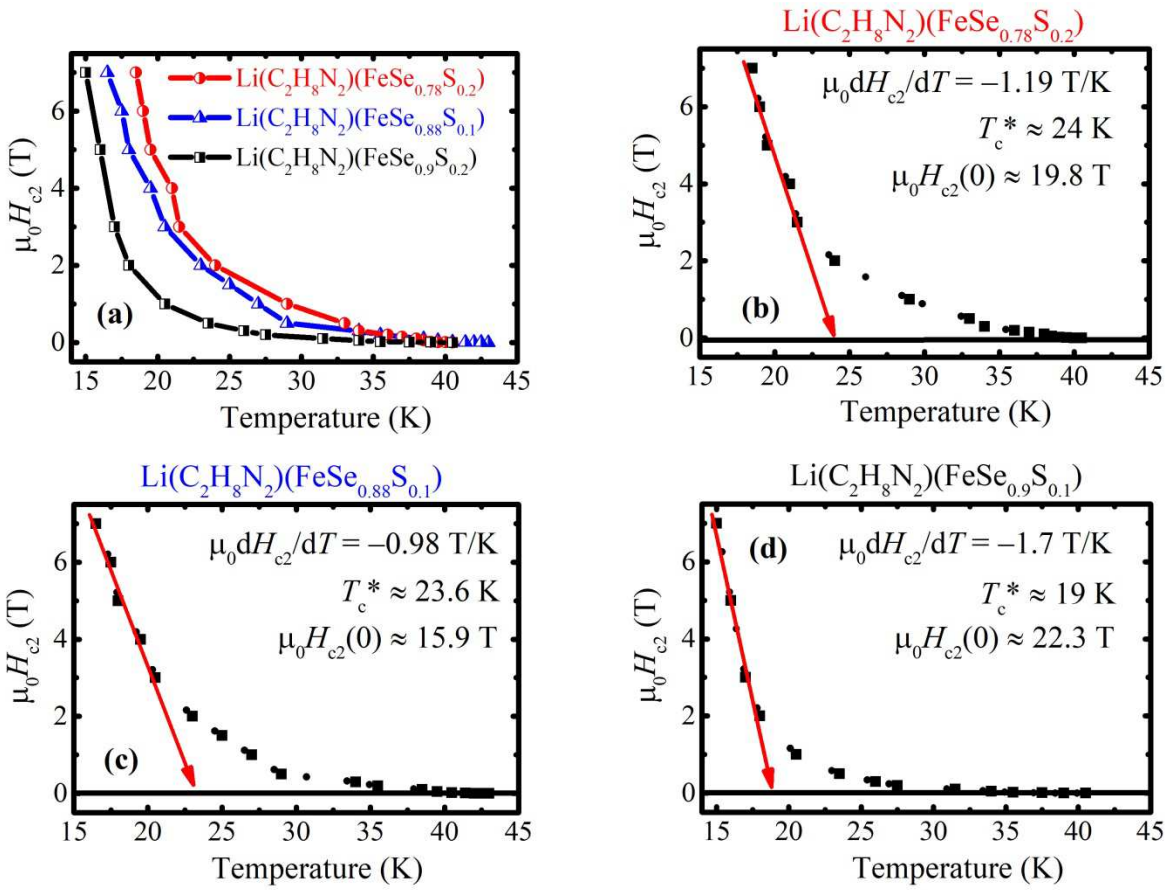

Figure 5.14. (a) Phase diagrams of the upper critical field H_{c2} builded up as a function of temperature for $Li(C_2H_8N_2)(FeSe_{0.78}S_{0.2})$, $Li(C_2H_8N_2)(FeSe_{0.88}S_{0.1})$, and $Li(C_2H_8N_2)(FeSe_{0.9}S_{0.1})$. Corresponding parameters of approximation and results of calculation of $H_{c2}(0)$ and zero-temperature coherence length $\xi(0)$ are presented straightforwardly on panels (b), (c), and (d).

Fig. 5.14a, 5.15a unambigously represent a differentiation of properties with stoichiometry change for samples obtained by the same synthesis approach. Meanwhile, phase diagrams for $Li(C_2H_8N_2)(FeSe_{0.95}S_{0.05})$ and $Li(C_2H_8N_2)(FeSe_{0.85}S_{0.15})$ almost coincide (fig. 5.15a), because they revealed quite similar character of ac susceptibility (fig. 5.11).

The upper critical field at zero temperature $H_{c2}(0)$ was calculated utilizing the Werthamer–Helfand–Hohenberg (WHH) equation (1.15) by approximation of linear parts of phase diagrams (fig. 5.14b-5.14d, fig. 5.15b-5.15d). The red arrows point out the transition temperature value T_c predicted by WHH theory. Importantly, the approximation was conducted for the points, which correspond to dc field higher than 2 T and treated as more reliable. The choice of approximation range was done with regard to behavior of $\chi'(T)$ dependences, since those recorded at high dc field did not exhibit high positive susceptibility values and transition to superconducting state seemed more sharp.

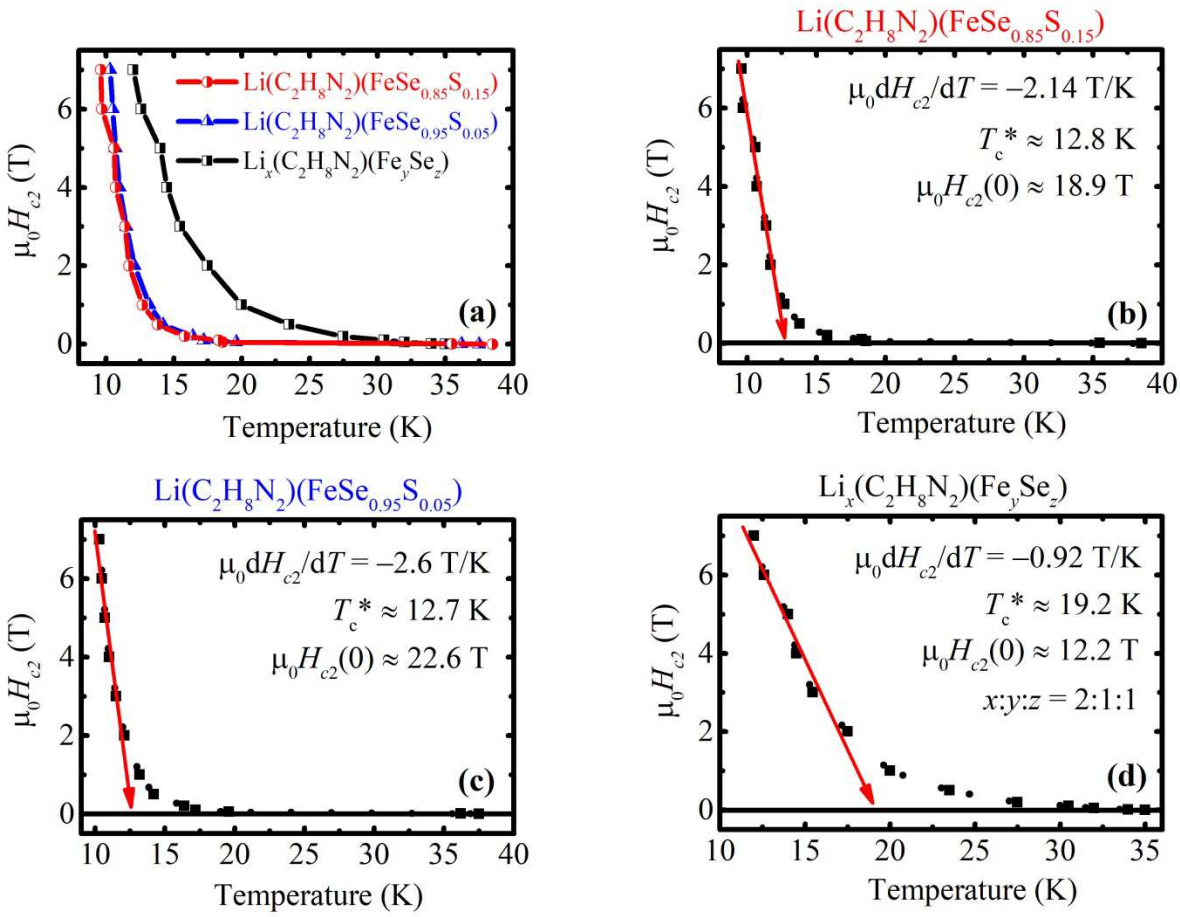

Figure 5.15. (a) Phase diagrams of the upper critical field H_{c2} builded up as a function of temperature for $Li(C_2H_8N_2)(FeSe_{0.85}S_{0.15})$, $Li(C_2H_8N_2)(FeSe_{0.95}S_{0.05})$, and $Li_2(C_2H_8N_2)(FeSe)$. Corresponding parameters of approximation and results of calculation of $H_{c2}(0)$ and zero-temperature coherence length $\xi(0)$ are presented immediately on panels (b), (c), and (d).

Ginzburg-Landau zero-temperature coherence length $\xi(0)$ was defined from the expression (1.14). Calculated values of $H_{c2}(0)$ and $\xi(0)$ for investigated materials are presented on corresponding graphs (fig. 5.14b-5.14d, fig. 5.15b-5.15d). The equation (1.13) has been applied to calculate a zero-temperature penetration depth, which turned out to be

equaled to 1171 nm. All obtained superconducting state parameters of investigated intercalated materials are summarized in tab. 5.3.

Table 5.3. The results of both dc and ac magnetic mesurements for intercalated materials.

№	Chemical composition	T_c^{onset}, K	T_c', K	$\mu_0 H_{c1}(0)$, mT	$\mu_0 dH_{c2}/dT$, T/K	T_c^*, K	$\mu_0 H_{c2}(0)$, T	$\xi(0)$, nm	$\lambda(0)$, nm
1	$Li(EDA)(FeSe_{0.9}S_{0.1})$	41	10	—	–1.7	19	22.3	3.84	—
2	$Li(EDA)(FeSe_{0.88}S_{0.1})$	43	10	—	–0.98	23.6	15.9	4.55	—
3	$Li(EDA)(FeSe_{0.78}S_{0.2})$	40	8	—	–1.19	24	19.8	4.08	—
4	$Li(EDA)(FeSe_{0.95}S_{0.05})$	39	—	—	–2.6	12.7	22.6	3.82	—
5	$Li(EDA)(FeSe_{0.85}S_{0.15})$	39	—	—	–2.14	12.8	18.9	4.18	—
6	$Li_2(EDA)(FeSe)$	34	—	0.7	–0.92	19.2	12.2	5.2	1171

Phase diagrams shown in fig. 5.14a, 5.15a illustrate absolutely unusual behavior of $H_{c2}(T)$. The positive curvature of $H_{c2}(T)$ dependence instead of negative parabolic like is observed for all of investigated samples. Similar deviation from classical pattern was studied before in layered intercalated systems [142] and in lead films [143] and considered as a consequence of dimensionality influence. Remarkably, in our case the dependence can be clearly divided into two parts: steep one with the slope of about 1–2 T/K in the temperature range below 13–24 K and flat one tail with much smaller slope of about 0.05–0.1 T/K. Since the zero-temperature H_{c2} was calculated from low-temperature region of $H_{c2}(T)$ phase diagram, it led to huge dicrepancy between the T_c^{onset} and T_c^*, two-times in fact. In order to understand the origin of such a difference, field dependences of magnetization at 30 K were measured (fig. 5.16). A developed hysteresis with distinct coercivity is observed up to 0.5 T for the samples with sulfur in chemical composition (fig. 5.16a). It stands for the existence of magnetic phases well below the T_c^{onset}. Meanwhile, $Li_2(C_2H_8N_2)FeSe$ from the 3rd subset demonstrated paramagnetic and almost completely reversible signal superimposed on superconducting Meissner effect in the small dc field range from approximately –15 mT to

15 mT. The exclusion in our specific case just confirmed the rule: ferro/paramagnetic phases are neighboring with superconducting one in the wide temperature range, specifically between the T_c^{onset} and T_c^*, where both are in close relation to each other.

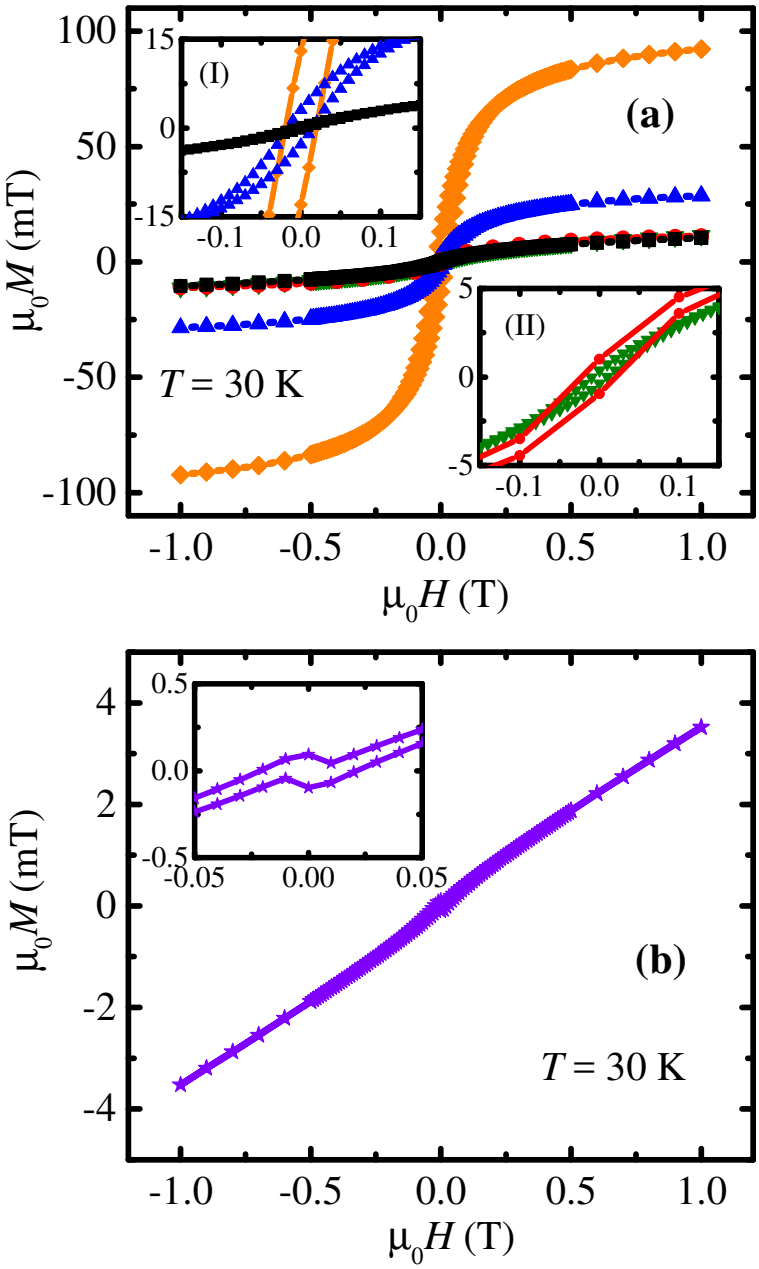

Figure 5.16. Panel (a) Magnetization loops at the temperature of 30 K. Black squares depict $Li(C_2H_8N_2)(FeSe_{0.95}S_{0.05})$, red circles – $Li(C_2H_8N_2)(FeSe_{0.9}S_{0.1})$, blue triangles – $Li(C_2H_8N_2)(FeSe_{0.88}S_{0.1})$, green inverted triangles – $Li(C_2H_8N_2)(FeSe_{0.85}S_{0.15})$, orange rhombi – $Li(C_2H_8N_2)(FeSe_{0.78}S_{0.2})$. (b) illustrates the results for $Li_2(C_2H_8N_2)FeSe$.

V.4. *Summary*

Intercalated $Li_x(C_2H_8N_2)(Fe_ySe_zS_{1-z})$ systems synthesized by solvothermal method within two different approaches were investigated by means of SQUID magnetometry. The superconducting transition temperature T_c^{onset} was defined by utilizing dc technique. Values of T_c^{onset} are close to those obtained for the iron-based systems intercalated with alkali metals and pyridine or alkali metals and ammonia [144]. Furthermore, the upper critical field $H_{c2}(T)$ investigations have been provided by means of ac susceptibility technique. Constructed phase diagrams allowed to calculate zero-temperature $H_{c2}(0)$ and related $\xi(0)$ (see tab. 5.3), which turned out to be two times smaller in case of $H_{c2}(0)$ with regard to iron-based materials without organic [145]. Although dry numbers say that the studied $Li_x(C_2H_8N_2)(Fe_ySe_zS_{1-z})$ systems expressed similar response with regard to magnetic field influence, it is necessary to admit several important details in their behavior:

1) High content of magnetic phases. The traces of magnetic phases were detected already from the dc experiment, i.e., from temperature dependences of magnetization, where the divergence between ZFC and FCC curves and big positive value of magnetization above the T_c^{onset} clearly point out their presence. Moreover, it turned out that the course of $H_{c2}(T)$ dependence obtained from the ac measurements is strongly distorted by the influence of magnetic inhomogeneities and reflected in huge difference between WHH T_c^* and T_c^{onset} values. It was proved that the region between T_c^* and T_c^{onset} corresponds to irreversible magnetization dependence, recorded as a function of dc magnetic field. Then, it can be concluded that co-existing magnetic and superconducting phases below the T_c^{onset} cooperate with each other on macroscopic level from the perspective of magnetic measurements.
2) Differentiation by synthesis approach. The materials from the 1st subset expressed higher T_c^{onset} with regard to materials from 2nd and 3rd subsets. Nevertheless, the transition to superconducting state is more smeared. Besides, visible signal from FeSe/FeSeS phase is observed only for samples from the 1st subset, which likely indicates less uniformly performed intercalation process.
3) Differentiation by stoichiometry. Although, the structure of investigated materials wasn't solved properly because of poor crystallinity, there important to admit unambiguous influence of nominal stoichiometry on superconducting properties performance. The samples with less amount of sulfur, i.e., $Li(C_2H_8N_2)(FeSe_{0.9}S_{0.1})$ from 1st subset and $Li(C_2H_8N_2)(FeSe_{0.95}S_{0.05})$ from 2nd subset expressed highest and

what more important comparable values of $H_{c2}(0)$. Interestingly, the sample completely without sulfur – $Li_2(C_2H_8N_2)(FeSe)$ from 3rd subset – exhibited least T_c^{onset} and $H_{c2}(0)$. However, neither secondary phases nor bifurcation between ZFC–FCC curves above the T_c^{onset} is observed. Small content of magnetic inhomogeneities in this sample, confirmed by field dependence of magnetization (fig. 5.16b), doesn't hide the signal from superconducting phase. That allowed to probe $H_{c1}(T)$ by means of dc magnetization technique, which obviously wasn't possible in case of other samples.

VI. Ultimate takeaways

The investigations by means of both dc and ac SQUID magnetometry techniques were carried out in order to probe the superconducting state of $CuBa_2Ca_3Cu_4O_{10+\delta}$ and $Li_x(C_2H_8N_2)(Fe_ySe_zS_{1-z})$ materials. With regard to obtained superconducting state parameters or to general response to magnetic field exposure those systems do not have much in common. The $CuBa_2Ca_3Cu_4O_{10+\delta}$, which turned out to possess strongly inhomogeneous nature from the perspective of structural composition and as a consequense weak interganular connections, exhibited good performance of superconducting target phase and its superconducting phase diagrams was studied by utilizing of conventional dc technique. Meanwhile, the $Li_x(C_2H_8N_2)(Fe_ySe_zS_{1-z})$ expressed highly inhomogeneous nature from both of structural (poor crystallinity) and superconducting (the presence of several superconducting phases, co-existence of ferro/paramagnetic inclusions below the T_c^{onset}) sides of the material. That inspired to utilize the combination of ac and dc techniques in order to analyze the underlying character of superconducting phase diagrams behavior.

References

[1] H. K. Onnes, "The Resistance of Pure Mercury at Helium Temperatures," *Commun. Phys. Lab. Univ. Leiden*, vol. 12, p. 1, 1911.

[2] G. W. Webb, F. Marsiglio, and J. E. Hirsch, "Superconductivity in the elements, alloys and simple compounds," *Phys. C Supercond. its Appl.*, vol. 514, pp. 17–27, Jul. 2015, doi: 10.1016/j.physc.2015.02.037.

[3] M. Tinkham, *Introduction to superconductivity*. Malabar FL: Krieger Publishing Company, 1975.

[4] W. Meissner and R. Ochsenfeld, "Ein neuer Effekt bei Eintritt der Supraleitfähigkeit," *Naturwissenschaften*, vol. 21, no. 44, pp. 787–788, Nov. 1933, doi: 10.1007/bf01504252.

[5] F. London, H. London, "The Electromagnetic Equations of the Supraconductor," *Proceedings of the Royal Society of London. Series A, Mathematical and Physical Sciences*, 1935. https://www.jstor.org/stable/96265 (accessed Jan. 27, 2023).

[6] L. D. Landau, V. L. Ginzburg, "On the Theory of Superconductivity," *Zh. Eksp. Teor. Fiz.*, vol. 20, p. 1064, 1950, doi: 10.1016/B978-0-08-010586-4.50078-x.

[7] J. Bardeen, L. N. Cooper, and J. R. Schrieffer, "Theory of superconductivity," *Phys. Rev.*, vol. 108, no. 5, pp. 1175–1204, Dec. 1957, doi: 10.1103/PhysRev.108.1175.

[8] K. H. Bennemann and J. B. Ketterson, "History of Superconductivity: Conventional, High-Transition Temperature and Novel Superconductors," *Superconductivity*, pp. 3–26, Apr. 2008, doi: 10.1007/978-3-540-73253-2_1.

[9] B. T. Matthias, "Chapter V Superconductivity in the Periodic System," *Prog. Low Temp. Phys.*, vol. 2, no. C, pp. 138–150, Jan. 1957, doi: 10.1016/s0079-6417(08)60104-3.

[10] K. Conder, "A second life of the Matthias's rules," *Supercond. Sci. Technol.*, vol. 29, no. 8, p. 080502, Jun. 2016, doi: 10.1088/0953-2048/29/8/080502.

[11] J. G. Bednorz and K. A. Müller, "Possible high T_c superconductivity in the Ba-La-Cu-O system," *Zeitschrift für Phys. B Condens. Matter*, vol. 64, no. 2, pp. 189–193, Jun. 1986, doi: 10.1007/bf01303701.

[12] M. K. Wu *et al.*, "Superconductivity at 93 K in a new mixed-phase Y-Ba-Cu-O compound system at ambient pressure," *Phys. Rev. Lett.*, vol. 58, no. 9, p. 908, Mar. 1987, doi: 10.1103/PhysRevLett.58.908.

[13] C. W. Chu, L. Z. Deng, and B. Lv, "Hole-doped cuprate high temperature superconductors," *Phys. C Supercond. its Appl.*, vol. 514, pp. 290–313, Jul. 2015, doi: 10.1016/j.physc.2015.02.047.

[14] G. F. Sun, K. W. Wong, B. R. Xu, Y. Xin, and D. F. Lu, "T_c enhancement of $HgBa_2Ca_2Cu_3O_{8+\delta}$ by Tl substitution," *Phys. Lett. A*, vol. 192, no. 1, pp. 122–124, Aug. 1994, doi: 10.1016/0375-9601(94)91026-x.

[15] D. Larbalestier, A. Gurevich, D. M. Feldmann, and A. Polyanskii, "High-T_c superconducting materials for electric power applications," *Nature*, vol. 414, no. 6861, pp. 368–377, 2001, doi: 10.1038/35104654.

[16] D. Larbalestier, "Critical currents and magnet applications of high-T_c superconductors," *Phys. Today*, vol. 44, no. 6, pp. 74–82, 1991, doi: 10.1063/1.881305.

[17] A. A. Khurram and N. A. Khan, "A Search for a Low Anisotropic Superconductor," *J. Electromagn. Anal. Appl.*, vol. 02, no. 02, pp. 63–74, 2010, doi: 10.4236/jemaa.2010.22010.

[18] C. Q. Jin, X. M. Qin, K. Shimizu, M. Nishiyama, T. Namiki, and Y. Yu, "The enhanced superconductivity of Cu-1234 under high pressure," *Int. J. Mod. Phys. B*, vol. 19, pp. 335–337, 2012, doi: 10.1142/S0217979205028530.

[19] X. Zhang *et al.*, "Atomic origin of the coexistence of high critical current density and high T_c in $CuBa_2Ca_3Cu_4O_{10+\delta}$ superconductors," *NPG Asia Mater.*, vol. 14, no. 1, pp. 1–8, 2022, doi: 10.1038/s41427-022-00396-2.

[20] B. I. Zimmer, W. Jeitschko, J. H. Albering, R. Glaum, and M. Reehuis, "The rate earth transition metal phosphide oxides LnFePO, LnRuPO and LnCoPO with ZrCuSiAs type structure," *J. Alloys Compd.*, vol. 229, no. 2, pp. 238–242, Nov. 1995, doi: 10.1016/0925-8388(95)01672-4.

[21] Y. Kamihara *et al.*, "Iron-Based Layered Superconductor: LaOFeP," *J. Am. Chem. Soc.*, vol. 128, no. 31, pp. 10012–10013, Jul. 2006, doi: 10.1021/ja063355c.

[22] Y. Kamihara, T. Watanabe, M. Hirano, and H. Hosono, "Iron-Based Layered Superconductor $La[O_{1-x}F_x]FeAs$ (x = 0.05−0.12) with T_c = 26 K," *J. Am. Chem. Soc.*, vol. 130, no. 11, pp. 3296–3297, Feb. 2008, doi: 10.1021/ja800073m.

[23] X. Zhao, F. Ma, Z.-Y. Lu, and T. Xiang, "$AFeSe_2$ (A = Tl, K, Rb, or Cs): Iron-based superconducting analog of the cuprates," *Phys. Rev. B*, vol. 101, no. 18, p. 184504, May 2020, doi: 10.1103/PhysRevB.101.184504.

[24] A. S. Sefat and D. J. Singh, "Chemistry and electronic structure of iron-based superconductors," *MRS Bull.*, vol. 36, no. 8, pp. 614–619, 2011, doi: 10.1557/mrs.2011.175.

[25] X. Chen, P. Dai, D. Feng, T. Xiang, and F. C. Zhang, "Iron-based high transition temperature superconductors," *Natl. Sci. Rev.*, vol. 1, no. 3, pp. 371–395, Sep. 2014, doi: 10.1093/nsr/nwu007.

[26] S. Medvedev *et al.*, "Electronic and magnetic phase diagram of β-$Fe_{1.01}Se$ with superconductivity at 36.7 K under pressure," *Nat. Mater.*, vol. 8, no. 8, pp. 630–633, 2009, doi: 10.1038/nmat2491.

[27] S. Margadonna *et al.*, "Pressure evolution of the low-temperature crystal structure and bonding of the superconductor FeSe (T_c = 37 K)," *Phys. Rev. B*, vol. 80, no. 6, p. 64506, Aug. 2009, doi: 10.1103/PhysRevB.80.064506.

[28] H. Okabe, N. Takeshita, K. Horigane, T. Muranaka, and J. Akimitsu, "Pressure-induced high-T_c superconducting phase in FeSe: Correlation between anion height and T_c," *Phys. Rev. B*, vol. 81, no. 20, p. 205119, May 2010, doi: 10.1103/PhysRevB.81.205119.

[29] Y. Mizuguchi, F. Tomioka, S. Tsuda, T. Yamaguchi, and Y. Takano, "Substitution Effects on FeSe Superconductor," *J. Phys. Soc. Jpn.*, vol. 78, no. 7, Jul. 2009, doi: 10.1143/jpsj.78.074712.

[30] Y. Mizuguchi, F. Tomioka, S. Tsuda, T. Yamaguchi, and Y. Takano, "Superconductivity in S-substituted FeTe," *Appl. Phys. Lett.*, vol. 94, no. 1, p. 012503, Jan. 2009, doi: 10.1063/1.3058720.

[31] K. W. Yeh *et al.*, "Tellurium substitution effect on superconductivity of the α-phase iron selenide," *Europhys. Lett.*, vol. 84, no. 3, p. 37002, Oct. 2008, doi: 10.1209/0295-5075/84/37002.

[32] M. H. Fang *et al.*, "Superconductivity close to magnetic instability in $Fe(Se_{1-x}Te_x)_{0.82}$," *Phys. Rev. B*, vol. 78, no. 22, p. 224503, Dec. 2008, doi: 10.1103/PhysRevB.78.224503.

[33] A. Krzton-Maziopa, "Intercalated Iron Chalcogenides: Phase Separation Phenomena and Superconducting Properties," *Front. Chem.*, vol. 9, p. 286, Jun. 2021, doi: 10.3389/fchem.2021.640361.

[34] H. K. Vivanco and E. E. Rodriguez, "The intercalation chemistry of layered iron chalcogenide superconductors," *J. Solid State Chem.*, vol. 242, pp. 3–21, Oct. 2016, doi: 10.1016/j.jssc.2016.04.008.

[35] A. Szewczyk, A. Wiśniewski, R. Puźniak, and H. Szymczak, *Magnetyzm i nadprzewodnictwo*, p. 286, 2012.

[36] G. Blatter and V. B. Geshkenbein, "Vortex Matter," *Superconductivity*, pp. 495–637, Apr. 2008, doi: 10.1007/978-3-540-73253-2_12.

[37] L. N. Cooper, "Bound Electron Pairs in a Degenerate Fermi Gas," *Phys. Rev.*, vol. 104, no. 4, p. 1189, Nov. 1956, doi: 10.1103/PhysRev.104.1189.

[38] L. P. Gor'kov, "Microscopic Derivation of the Ginzburg-Landau Equations in the Theory of Superconductivity," *J. Exptl. Theor. Phys.*, vol. 36, no. 9, pp. 1918–1923, 1959.

[39] L. P. Gor'kov, "The Critical Supercooling Field in Superconductivity Theory," *J. Exptl. Theor. Phys.*, vol. 37, no. 10, pp. 833–842, 1960.

[40] L. P. Gor'kov, "Theory of Superconducting Alloys in a Strong Magnetic Field Near the Critical Temperature," *J. Exptl. Theor. Phys.*, vol. 37, no. 10, pp. 1407–1416, 1960.

[41] L. P. Gor'kov, "An Estimate of the Limiting Values of the Critical Fields for Hard Superconductors," *J. Exptl. Theor. Phys.*, vol. 44, pp. 767–769, 1963.

[42] E. Helfand and N. R. Werthamer, "Temperature and purity dependence of the superconducting critical field, H_{c2}," *Phys. Rev. Lett.*, vol. 13, pp. 686–688, 1964.

[43] E. Helfand and N. R. Werthamer, “Temperature and purity dependence of the superconducting critical field, H_{c2}. II,” *Phys. Rev.*, vol. 147, pp. 288–294, 1966.

[44] N. R. Werthamer, E. Helfand, and P. C. Hohenberg, “Temperature and purity dependence of the superconducting critical field, H_{c2}. III. Electron spin and spin-orbit effects,” *Phys. Rev.*, vol. 147, no. 1, pp. 295–302, 1966, doi: 10.1103/PhysRev.147.295.

[45] G. Sharma, *Superconductivity: Basics and Applications to Magnets*, MRS Bulletin, vol. 40, no. 9. 2015, doi: 10.1557/mrs.2015.217.

[46] C. P. Bean, “Magnetization of High-Field Superconductors,” *Rev. Mod. Phys.*, vol. 36, no. 1, p. 31, Jan. 1964, doi: 10.1103/RevModPhys.36.31.

[47] C. P. Bean, “Magnetization of Hard Superconductors,” *Phys. Rev. Lett.*, vol. 8, no. 6, p. 250, Mar. 1962, doi: 10.1103/PhysRevLett.8.250.

[48] D. X. Chen and R. B. Goldfarb, “Kim model for magnetization of type-II superconductors,” *J. Appl. Phys.*, vol. 66, no. 6, pp. 2489–2500, Sep. 1989, doi: 10.1063/1.344261.

[49] T. Matsushita, *Flux pinning in superconductors*, Springer Berlin, Heidelberg, 2007, doi: 10.1007/978-3-540-44515-9.

[50] K. A. Müller, M. Takashige, and J. G. Bednorz, “Flux trapping and superconductive glass state in La_2CuO_{4-y}:Ba,” *Phys. Rev. Lett.*, vol. 58, no. 11, p. 1143, Mar. 1987, doi: 10.1103/PhysRevLett.58.1143.

[51] P. de Rango *et al.*, “The « irreversibility line » of $Bi_{2-x}Pb_xSr_2Ca_2Cu_3O_{10}$: a possible breakdown of an intrinsic proximity effect,” *J. Phys.*, vol. 50, no. 18, pp. 2857–2868, Sep. 1989, doi: 10.1051/jphys:0198900500180285700.

[52] P. M. Shirage, A. Iyo, D. D. Shivagan, Y. Tanaka, H. Kito, and Y. Kodama, “Irreversibility line and flux pinning properties in a multilayered cuprate superconductor of $Ba_2Ca_3Cu_4O_8(O,F)_2$ (T_c = 105 K),” *Supercond. Sci. Technol.*, vol. 21, no. 7, p. 075014, May 2008, doi: 10.1088/0953-2048/21/7/075014.

[53] F. M. Barros *et al.*, “Unconventional superconducting granularity of the $Y_{1-x}Pr_xBa_2Cu_3O_{7-\delta}$ compound,” *Phys. Rev. B - Condens. Matter Mater. Phys.*, vol. 73, no. 9, p. 094515, Mar. 2006, doi: 10.1103/PhysRevB.73.094515.

[54] A. Schilling, R. Jin, J. D. Guo, and H. R. Ott, “Irreversibility line of monocrystalline $Bi_2Sr_2CaCu_2O_8$: Experimental evidence for a dimensional crossover of the vortex ensemble,” *Phys. Rev. Lett.*, vol. 71, no. 12, p. 1899, Sep. 1993, doi: 10.1103/PhysRevLett.71.1899.

[55] P. G. de Gennes, *Superconductivity of Metals and Alloys*. Westview Press, 1999.

[56] V. G. Kogan, M. Ledvij, A. Y. Simonov, J. H. Cho, and D. C. Johnston, “Role of vortex fluctuations in determining superconducting parameters from magnetization data for layered superconductors,” *Phys. Rev. Lett.*, vol. 70, no. 12, pp. 1870–1873, Mar. 1993, doi: 10.1103/PhysRevLett.70.1870.

[57] V. Kogan *et al.*, "Nonlocal electrodynamics and low-temperature magnetization of clean high-κ superconductors," *Phys. Rev. B*, vol. 54, no. 17, p. 12386, Nov. 1996, doi: 10.1103/PhysRevB.54.12386.

[58] G. Fuchs *et al.*, "Upper critical field and irreversibility line in superconducting MgB_2," *Solid State Commun.*, vol. 118, no. 10, pp. 497–501, Jun. 2001, doi: 10.1016/S0038-1098(01)00157-0.

[59] R. Sultana, P. Rani, A. K. Hafiz, R. Goyal, and V. P. S. Awana, "An Intercomparison of the Upper Critical Fields (H_{c2}) of Different Superconductors — $YBa_2Cu_3O_7$, MgB_2, $NdFeAsO_{0.8}F_{0.2}$, $FeSe_{0.5}Te_{0.5}$ and Nb_2PdS_5," *J. Supercond. Nov. Magn.*, vol. 29, no. 6, pp. 1399–1404, Jun. 2016, doi: 10.1007/S10948-016-3507-1.

[60] R. Wesche, *High-Temperature Superconductors*, Springer Handbook of Electronic and Photonic Materials, S. Kasap and P. Capper, Eds. Cham: Springer International Publishing, 2017, doi: 10.1007/978-3-319-48933-9_50.

[61] W. R. Pudelko *et al.*, "Bismuth and oxygen valencies and superconducting state properties in $Ba_{1-x}K_xBiO_3$ superconductor," *Phys. B Condens. Matter*, vol. 591, p. 412226, Aug. 2020, doi: 10.1016/j,physb.2020.412226.

[62] F. Hayashi, H. Lei, J. Guo, and H. Hosono, "Modulation effect of interlayer spacing on the superconductivity of electron-doped FeSe-based intercalates," *Inorg. Chem.*, vol. 54, no. 7, pp. 3346–3351, Apr. 2015, doi: 10.1021/ic503033k.

[63] R. Puzniak, K. Isawa, R. Usami, and H. Yamauchi, "Superconducting-state thermodynamic parameters of $HgBa_2Ca_{n-1}Cu_nO_y$ (n=1, 2, and 3)," *Phys. C Supercond.*, vol. 233, no. 1–2, pp. 21–29, Nov. 1994, doi: 10.1016/0921-4534(94)00582-6.

[64] R. Puzniak, R. Usami, K. Isawa, and H. Yamauchi, "Superconducting-state thermodynamic parameters and anisotropy of $HgBa_2Ca_{n-1}Cu_nO_y$ by reversible magnetization measurements," *Phys. Rev. B*, vol. 52, no. 5, p. 3756, Aug. 1995, doi: 10.1103/PhysRevB.52.3756.

[65] M. Naito, A. Matsuda, K. Kitazawa, S. Kambe, I. Tanaka, and H. Kojima, "Temperature dependence of anisotropic lower critical fields in $(La_{1-x}Sr_x)_2CuO_4$," *Phys. Rev. B*, vol. 41, no. 7, pp. 4823–4826, Mar. 1990, doi: 10.1103/PhysRevB.41.4823.

[66] C. V. Topping and S. J. Blundell, "A.C. susceptibility as a probe of low-frequency magnetic dynamics," *J. Phys. Condens. Matter*, vol. 31, no. 1, Jan. 2019, doi: 10.1088/1361-648X/aaed96.

[67] M. K. Lee, E. V. Charnaya, C. Tien, L. J. Chang, and Y. A. Kumzerov, "Ac susceptibility studies of a superconducting gallium nanocomposite: Crossover in the upper critical field line and activation barriers," *J. Appl. Phys.*, vol. 113, no. 11, p. 113903, Mar. 2013, doi: 10.1063/1.4795789.

[68] C. S. Pande, R. A. Masumura, and C. R. Feng, "Thermally Activated Flux Creep in High T_c Superconductors," *Mater. Sci. Forum*, vol. 426–432, no. 4, pp. 3493–3498, 2003, doi: 10.4028/www.scientific.net/MSF.426-432.3493.

[69] M. Nikolo *et al.*, "Flux Dynamics, ac Losses, and Activation Energies in $(Ba_{0.6}K_{0.4})Fe_2As_2$ Bulk Superconductor," *J Low Temp Phys*, vol. 178, p. 189, 2015, doi: 10.1007/s10909-014-1237-y.

[70] S. Senoussi, "Review of the critical current densities and magnetic irreversibilities in high T_c superconductors," *J. Phys. III*, vol. 2, no. 7, pp. 1041–1257, Jul. 1992, doi: 10.1051/jp3:1992102.

[71] S. B. Namuco, M. L. Lao, and R. V. Sarmago, "Granular Responses of $GdBa_2Cu_3O_{7-\delta}$ Using ac Magnetic Susceptibility Measurement under ac and dc Magnetic Fields," *Phys. Procedia*, vol. 45, pp. 169–172, Jan. 2013, doi: 10.1016/j.phpro.2013.04.079.

[72] S. Çelebi, I. Karaca, E. Aksu, and A. Gencer, "Frequency dependence of the intergranular AC loss peak in a high-T_c Bi–(Pb)–Sr–Ca–Cu–O bulk superconductor," *Phys. C Supercond.*, vol. 309, no. 1–2, pp. 131–137, Dec. 1998, doi: 10.1016/S0921-4534(98)00531-0.

[73] J.L. Gonzalez, P. Muné, L. E. Flores, and E. Altshuler, "AC susceptibility study of the intergranular irreversibility line in BSCCO ceramic superconductors," *Phys. C Supercond.*, vol. 255, no. 1–2, pp. 76–80, Dec. 1995, doi: 10.1016/0921-4534(95)00585-4.

[74] M. K. Lee, E. V. Charnaya, S. Mühlbauer, U. Jeng, L. J. Chang, and Y. A. Kumzerov, "The morphologic correlation between vortex transformation and upper critical field line in opal-based nanocomposites," *Sci. Rep.*, vol. 11, no. 1, pp. 1–11, Feb. 2021, doi: 10.1038/s41598-021-84343-1.

[75] A. Wang and C. Petrovic, "Vortex pinning and irreversibility fields in $FeS_{1-x}Se_x$ (x = 0, 0.06)," *Appl. Phys. Lett.*, vol. 110, no. 23, Jun. 2017, doi: 10.1063/1.4985292.

[76] R. B. Flippen, "ac susceptibility measurements and the irreversibility line of high-temperature superconductors," *Phys. Rev. B*, vol. 45, no. 21, p. 12498, Jun. 1992, doi: 10.1103/PhysRevB.45.12498.

[77] S. Galeski, P. W. J. Moll, N. Zhigadlo, K. Mattenberger, and B. Batlogg, "Critical fields and fluctuations determined from specific heat and magnetoresistance in the same nanogram SmFeAs(O,F) single crystal," *Phys. Rev. B*, vol. 96, no. 10, p. 104511, Sep. 2017, doi: 10.1103/PhysRevB.96.104511.

[78] Z. Shermadini *et al.*, "Superconducting properties of single-crystalline $A_xFe_{2-y}Se_2$ (A=Rb, K) studied using muon spin spectroscopy," *Phys. Rev. B*, vol. 85, no. 10, p. 100501, Mar. 2012, doi: 10.1103/PhysRevB.85.100501.

[79] S. Rinott *et al.*, "Tuning across the BCS-BEC crossover in the multiband superconductor $Fe_{1+y}Se_xTe_{1-x}$: An angle-resolved photoemission study," *Sci. Adv.*, vol. 3, no. 4, Apr. 2017, doi: 10.1126/sciadv.1602372.

[80] P. Mangin and R. Kahn, *Superconductivity: An introduction*, Springer Cham, pp. 1–379, Jan. 2016, doi: 10.1007/978-3-319-50527-5.

[81] M. Buchner, K. Höfler, B. Henne, V. Ney, and A. Ney, "Tutorial: Basic principles, limits of detection, and pitfalls of highly sensitive SQUID magnetometry for nanomagnetism and spintronics," *J. Appl. Phys.*, vol. 124, no. 16, Oct. 2018, doi: 10.1063/1.5045299/1030088.

[82] *MPMS Software System Reference Manual*, Quantum Design, San Diego, 1990.

[83] S. Stefanowicz, “Magnetyczny Diagram Fazowy i Wykładniki Krytyczne w Izolatorze Magnetycznym (Ga,Mn)N,” Institute of Pysics PAS, PhD Thesis, 2016.

[84] D. Martien, “Introduction to AC Susceptibility”, Quantum Design, 2001.

[85] D. C. Rillo, F. Lera, A. Badia, L.A. Angurel, J. Bartolome, F. Palacio, R. Navarro, and A. J. van Duyneveldt, “Multipurpose cryostate for low temperature magnetic and electric measurements of solids,” in *Proceedings of the Office of Naval Research Workshop on Magnetic Susceptibility of Superconductors and Other Spin System*, Springer Science + Business Media, LLC, pp. 1–24, 1991.

[86] J. E. Hirsch, M. B. Maple, and F. Marsiglio, “Superconducting materials classes: Introduction and overview,” *Phys. C Supercond. its Appl.*, vol. 514, pp. 1–8, Jul. 2015, doi: 10.1016/j.physc.2015.03.002.

[87] C. P. Poole and F. J. Owens, “Cuprates,” *Handbook of Superconductivity*, Academic Press, pp. 251–265, Jan. 2000, doi: 10.1016/b978-012561460-3/50008-4.

[88] R. Gladyshevskii and P. Galez, “Crystal Structures of High-T_c Superconducting Cuprates,” *Handb. Supercond.*, pp. 267–431, Jan. 2000, doi: 10.1016/b978-012561460-3/50009-6.

[89] A. R. Schmidt *et al.*, “Electronic structure of the cuprate superconducting and pseudogap phases from spectroscopic imaging STM,” *New J. Phys.*, vol. 13, no. 6, p. 065014, Jun. 2011, doi: 10.1088/1367-2630/13/6/065014.

[90] J. Orenstein and A. J. Millis, “Advances in the physics of high-temperature superconductivity,” *Science*, vol. 288, no. 5465, pp. 468–474, Apr. 2000, doi: 10.1126/science.288.5465.468.

[91] J. L. Tallon and J. G. Storey, “Thermodynamics of the pseudogap in cuprates,” *Front. Phys.*, vol. 10, p. 1160, Nov. 2022, doi: 10.3389/fphy.2022.1030616.

[92] C. T. Chen *et al.*, “Electronic states in $La_{2-x}Sr_xCuO_{4+d}$ probed by soft-x-ray absorption,” *Phys. Rev. Lett.*, vol. 66, no. 1, p. 104, Jan. 1991, doi: 10.1103/PhysRevLett.66.104.

[93] L. Sederholm *et al.*, “Extremely Overdoped Superconducting Cuprates via High Pressure Oxygenation Methods,” *Condens. Matter*, vol. 6, no. 4, p. 50, Dec. 2021, doi: 10.3390/condmat6040050.

[94] Q. Q. Liu *et al.*, “Correlation of superconductivity with the ordering state at the apical oxygen layer in the $Sr_2CuO_{3+\delta}$ superconductor,” *Phys. C Supercond. its Appl.*, vol. 460–462, pp. 56–57, Sep. 2007, doi: 10.1016/j.physc.2007.03.297.

[95] G. A. Bordovskii, A. V. Marchenko, F. S. Nasredinov, and P. P. Seregin, “Charge states of atoms in ceramic superconductors $HgBa_2Ca_{n-1}Cu_nO_{2n+2}$, $Tl_2Ba_2Ca_{n-1}Cu_nO_{2n+4}$ and $Bi_2Sr_2Ca_{n-1}Cu_nO_{2n+4}$ (n = 1–3),” *Glas. Phys. Chem.*, vol. 36, no. 4, pp. 411–418, 2010, doi: 10.1134/s1087659610040048.

[96] S. Graser, P. J. Hirschfeld, T. Kopp, R. Gutser, B. M. Andersen, and J. Mannhart, “How grain boundaries limit supercurrents in high-temperature superconductors,” *Nat. Phys.*, vol. 6, no. 8, pp. 609–614, 2010, doi: 10.1038/nphys1687.

[97] C. Q. Jin, S. Adachi, X. J. Wu, H. Yamauchi, and S. Tanaka, "117 K superconductivity in the BaCaCuO system," *Phys. C Supercond. its Appl.*, vol. 223, no. 3–4, pp. 238–242, 1994, doi: 10.1016/0921-4534(94)91267-x.

[98] J. Akimoto, Y. Oosawa, K. Tokiwa, M. Hirabayashi, and H. Ihara, "Crystal structure analysis of $Cu_{0.6}Ba_2Ca_3Cu_4O_{10.8}$ by single-crystal X-ray diffraction method," *Phys. C Supercond.*, vol. 242, no. 3–4, pp. 360–364, Feb. 1995, doi: 10.1016/0921-4534(94)02417-0.

[99] H. W. Zandbergen and J. Jansen, "Accurate structure determinations of very small (4–20 nm) areas, using refinement of dynamic electron diffraction data," *J. Microsc.*, vol. 190, no. 1–2, pp. 222–237, Apr. 1998, doi: 10.1046/j.1365-2818.1998.3270880.x.

[100] A. Bhaumik, R. Sachan, and J. Narayan, "Magnetic relaxation and three-dimensional critical fluctuations in B-doped Q-carbon – a high-temperature superconductor," *Nanoscale*, vol. 10, no. 26, pp. 12665–12673, 2018, doi: 10.1039/c8nr03406k.

[101] Y. Li *et al.*, "Critical magnetic fields of superconducting aluminum-substituted $Ba_8Si_{42}Al_4$ clathrate," *J. Appl. Phys.*, vol. 117, no. 21, pp. 3–8, 2015, doi: 10.1063/1.4921702.

[102] Z. C. Wang *et al.*, "Superconductivity in $KCa_2Fe_4As_4F_2$ with separate double Fe_2As_2 layers," *J. Am. Chem. Soc.*, vol. 138, no. 25, pp. 7856–7859, 2016, doi: 10.1021/jacs.6b04538.

[103] D. Dimos, P. Chaudhari, and J. Mannhart, "Superconducting transport properties of grain boundaries in $YBa_2Cu_3O_7$ bicrystals," *Phys. Rev. B*, vol. 41, no. 7, p. 4038, Mar. 1990, doi: 10.1103/PhysRevB.41.4038.

[104] B. Mayer, L. Alff, T. Träuble, R. Gross, P. Wagner, and H. Adrian, "Superconducting transport properties of $Bi_2Sr_2CaCu_2O_{8+x}$ bicrystal grain boundary junctions," *Appl. Phys. Lett.*, vol. 63, no. 7, p. 996, Jun. 1998, doi: 10.1063/1.109818.

[105] G. Wang, M. J. Raine, and D. P. Hampshire, "The cause of 'weak-link' grain boundary behaviour in polycrystalline $Bi_2Sr_2CaCu_2O_8$ and $Bi_2Sr_2Ca_2Cu_3O_{10}$ superconductors," *Supercond. Sci. Technol.*, vol. 31, no. 2, p. 024001, Jan. 2018, doi: 10.1088/1361-6668/aaa1b8.

[106] A. Lynnyk, R. Puzniak, L. Shi, J. Zhao, and C. Jin, "Superconducting State Properties of $CuBa_2Ca_3Cu_4O_{10+\delta}$," *Materials,* vol. 16, no. 14, p. 5111, Jul. 2023, doi: 10.3390/ma16145111.

[107] P. Rani, R. Jha, and V. P. S. Awana, "AC susceptibility study of superconducting $YBa_2Cu_3O_7$:Ag_x bulk composites (x = 0.0–0.20): The role of intra and intergranular coupling," *J. Supercond. Nov. Magn.*, vol. 26, no. 7, pp. 2347–2352, Jul. 2013, doi: 10.1007/s10948-013-2203-7.

[108] P. Rani, A. K. Hafiz, and V. P. S. Awana, "Temperature dependence of lower critical field of YBCO superconductor," *AIP Conf. Proc.*, vol. 1953, no. 1, p. 120026, May 2018, doi: 10.1063/1.5033091.

[109] J. R. Clem, "Granular and superconducting-glass properties of the high-temperature superconductors," *Phys. C Supercond.*, vol. 153–155, pp. 50–55, Jun. 1988, doi: 10.1016/0921-4534(88)90491-1.

[110] A. I. Malik, S. Çelebi, and S. A. Halim, "AC susceptibility study in $Bi_{1.6}Pb_{0.4}Sr_2(Ca_{1-x}Nd_x)_2Cu_3O_\delta$ ceramic superconductors," *Phys. C Supercond.*, vol. 377, no. 4, pp. 421–430, Sep. 2002, doi: 10.1016/s0921-4534(02)01458-2.

[111] C.-Q. Jin, S. Adachi, X.-J. Wu, and H. Yamauchi, "A New Homologous Series of Compounds: Cu-12(n−1)n :P," *Adv. Supercond. VII*, vol. 12, no. 249, pp. 249–254, 1995, doi: 10.1007/978-4-431-68535-7_54.

[112] G. N. Rao, P. Molinie, M. Ganne, and D. S. Babu, "Magnetic relaxation, lower critical field and irreversibility line of W doped (Bi, Pb)-2223 superconductor," *Mod. Phys. Lett. B*, vol. 09, no. 21, pp. 1387–1396, Nov. 2011, doi: 10.1142/s0217984995001388.

[113] R. Goyal, A. K. Srivastava, M. Mishra, G. Gupta, R. Jha, and V. P. S. Awana, "X-ray Photoelectron Spectroscopy, Magnetotransport and Magnetisation Study of Nb_2PdS_5 Superconductor," *J. Supercond. Nov. Magn.*, vol. 31, no. 4, pp. 943–949, Apr. 2018, doi: 10.1007/s10948-017-4415-8.

[114] A. Galluzzi *et al.*, "Magnetic Vortex Phase Diagram for a Non-Optimized $CaKFe_4As_4$ Superconductor Presenting a Wide Vortex Liquid Region and an Ultra-High Upper Critical Field," *Appl. Sci.,* vol. 13, no. 2, p. 884, Jan. 2023, doi: 10.3390/app13020884.

[115] M. Salvato *et al.*, "Upper Critical Field and Irreversibility Line in $Bi_2Sr_2CuO_{6+\delta}/CaCuO_2$ Superconducting Superlattices Obtained by MBE," *Int. J. Mod. Phys. B*, vol. 14, no. 25–27, pp. 2767–2772, Jan. 2012, doi: 10.1142/s0217979200002879.

[116] M. C. Steele, "Magnetic Field Penetration in Superconducting Lead," *Phys. Rev.*, vol. 78, no. 6, p. 791, Jun. 1950, doi: 10.1103/PhysRev.78.791.

[117] R. Puźniak, Y. Zhang, K. V. Rao, and S. Tyagi, "Anomalous field-dependence of Meissner fraction in bulk and successively pulverized YBaCuO.," *Phys. C Supercond. its Appl.*, vol. 162–164, pp. 717–718, Dec. 1989, doi: 10.1016/0921-4534(89)91225-2.

[118] J. Hecher *et al.*, "Small grains: a key to high-field applications of granular Ba-122 superconductors?," *Supercond. Sci. Technol.*, vol. 29, no. 2, p. 025004, Dec. 2015, doi: 10.1088/0953-2048/29/2/025004.

[119] D. V. Shantsev, M. R. Koblischka, Y. M. Galperin, T. H. Johansen, L. Půst, and M. Jirsa, "Central Peak Position in Magnetization Loops of High-T_c Superconductors," *Phys. Rev. Lett.*, vol. 82, no. 14, p. 2947, Apr. 1999, doi: 10.1103/PhysRevLett.82.2947.

[120] D. X. Chen, J. Nogues, and K. V. Rao, "A.c. susceptibility and intergranular critical current density of high T_c superconductors," *Cryogenics*, vol. 29, no. 8, pp. 800–808, Aug. 1989, doi: 10.1016/0011-2275(89)90153-7.

[121] D. X. Chen, Y. Mei, and H. L. Luo, "Critical-current density in sintered high-T_c (Bi, Pb)-Sr-Ca-Cu-Oxide," *Phys. C Supercond.*, vol. 167, no. 3–4, pp. 317–323, May 1990, doi: 10.1016/0921-4534(90)90349-j.

[122] D. X. Chen and A. Sanchez, "Theoretical critical-state susceptibility spectra and their application to high-T_c superconductors," *J. Appl. Phys.*, vol. 70, no. 10, pp. 5463–5477, Nov. 1991, doi: 10.1063/1.350204.

[123] H. Ihara, Y. Sekita, H. Tateai, N. A. Khan, K. Ishida, E. Harashima, T. Kojima, H. Yamamoto, K. Tanaka, Y. Tanaka, N. Terada, and H. Obara, "Superconducting Properties of $Cu_{1-x}Tl_x$-1223 [$C_{1-x}Tl_x(Ba,Sr)_2Ca_2Cu_3O_{10-y}$] Thin Films," *Appl. Supercond.*, vol. 9, no. 2, pp. 1551–1554, 1999.

[124] C. Fischer, G. Fuchs, B. Holzapfel, B. Schüpp-Niewa, and H. Warlimont, *Superconductors*, Springer, Berlin, Heidelberg, 2005. doi: 10.1007/3-540-30437-1_10.

[125] C. P. Poole, J. F. Zasadzinski, R. K. Zasadzinski, and P. B. Allen, "Characteristic parameters," *Handb. Supercond.*, pp. 433–489, Jan. 2000, doi: 10.1016/b978-012561460-3/50010-2.

[126] H. Hosono, A. Yamamoto, H. Hiramatsu, and Y. Ma, "Recent advances in iron-based superconductors toward applications," *Mater. Today*, vol. 21, no. 3, pp. 278–302, Apr. 2018, doi: 10.1016/j.mattod.2017.09.006.

[127] H. Fong-Chi *et al.*, "Superconductivity in the PbO-type structure α-FeSe," *Proc. Natl. Acad. Sci.*, vol. 105, no. 38, pp. 14262–14264, Sep. 2008, doi: 10.1073/pnas.0807325105.

[128] K. Zhou, J. Wang, Y. Song, L. Guo, and J.-G. Guo, "Highly-Tunable Crystal Structure and Physical Properties in FeSe-Based Superconductors", doi: 10.3390/cryst9110560.

[129] G. Portalone, S. Clarke, D. Dini, and A. Krzton-Maziopa, "Intercalated Iron Chalcogenides: Phase Separation Phenomena and Superconducting Properties," *Front. Chem.* vol. 1, p. 640361, 2021, doi: 10.3389/fchem.2021.640361.

[130] A. Krzton-Maziopa, E. Pesko, and R. Puzniak, "Superconducting selenides intercalated with organic molecules: synthesis, crystal structure, electric and magnetic properties, superconducting properties, and phase separation in iron based-chalcogenides and hybrid organic-inorganic superconductors," *J. Phys. Condens. Matter*, vol. 30, no. 24, p. 243001, May 2018, doi: 10.1088/1361-648x/aabeb5.

[131] M. Burrard-Lucas *et al.*, "Enhancement of the superconducting transition temperature of FeSe by intercalation of a molecular spacer layer," *Nat. Mater.*, vol. 12, pp. 15–19, 2013, doi: 10.1038/nmat3464.

[132] T. Noji, T. Hatakeda, S. Hosono, T. Kawamata, M. Kato, and Y. Koike, "Synthesis and post-annealing effects of alkaline-metal-ethylenediamine-intercalated superconductors $A_x(C_2H_8N_2)_yFe_{2-z}Se_2$ (A = Li, Na) with T_c = 45 K," *Phys. C Supercond. its Appl.*, vol. 504, pp. 8–11, 2014, doi: 10.1016/j.physc.2014.01.007.

[133] X. Miao *et al.*, "Preparation of new superconductors by metal doping of two-dimensional layered materials using ethylenediamine," *Phys. Rev. B*, vol. 96, no. 1, p. 014502, Jul. 2017, doi: 10.1103/PhysRevB.96.014502.

[134] L. Zhao *et al.*, "Structural evolution and phase diagram of the superconducting iron selenides $Li_x(C_2H_8N_2)_yFe_2Se_2$($x$=0∼0.8)," *Phys. Rev. B*, vol. 99, no. 9, p. 094503, Mar. 2019, doi: 10.1103/PhysRevB.99.094503.

[135] M. Abdel-Hafiez *et al.*, "Superconducting properties of sulfur-doped iron selenide," *Phys. Rev. B*, vol. 91, no. 16, pp. 1–12, 2015, doi: 10.1103/PhysRevB.91.165109.

[136] Z. Gao *et al.*, "A FeSe-based superconductor $(C_2H_8N_2)_xFeSe$ with only ethylenediamine intercalated," *Science China Mater.*, vol. 61, no. 7, pp. 977–984, 2018, doi: 10.1007/s40843-017-9230-2.

[137] X. F. Lu *et al.*, "Coexistence of superconductivity and antiferromagnetism in $(Li_{0.8}Fe_{0.2})OHFeSe$," *Nature Mater.*, vol. 14, pp. 325–329, 2015, doi: 10.1038/nmat4155.

[138] M. Nikolo, X. Shi, E. S. Choi, J. Jiang, J. D. Weiss, and E. E. Hellstrom, "Inter- and Intra-Granular Flux Pinning Properties in $Ba(Fe_{0.91}Co_{0.09})_2As_2$ Superconductor in AC and DC Magnetic Fields," *J. Low Temp. Phys.*, vol. 178, no. 5–6, pp. 345–354, Mar. 2015, doi: 10.1007/s10909-014-1254-x.

[139] M. Nikolo, V. S. Zapf, J. Singleton, J. Jiang, J. D. Weiss, and E. E. Hellstrom, "Vortex Flux Dynamics and Harmonic ac Magnetic Response of $Ba(Fe_{0.94}Ni_{0.06})_2As_2$ Bulk Superconductor," *J. Supercond. Nov. Magn.*, vol. 29, no. 11, pp. 2745–2752, Nov. 2016, doi: 10.1007/s10948-016-3618-8.

[140] J. A. Mydosh, "Spin glasses: Redux: An updated experimental/materials survey," *Reports Prog. Phys.*, vol. 78, no. 5, 2015, doi: 10.1088/0034-4885/78/5/052501.

[141] M. F. Mostafa and A. Hassen, "AC susceptibility of the $Hg_{0.3}La_{0.7}Ba_2Ca_3(Cu_{0.95}Ag_{0.5})_4O_{10+\delta}$ superconductor," *Phys. C Supercond. its Appl.*, vol. 528, pp. 12–16, Sep. 2016, doi: 10.1016/j.physc.2016.06.021.

[142] J. A. Woollam, R. B. Somoano, and P. O'Connor, "Positive Curvature of the H_{c2}-versus-T_c Boundaries in Layered Superconductors," *Phys. Rev. Lett.*, vol. 32, no. 13, pp. 712–714, Apr. 1974, doi: 10.1103/PhysRevLett.32.712.

[143] M. M. Özer, J. R. Thompson, and H. H. Weitering, "Hard superconductivity of a soft metal in the quantum regime," 2006, doi: 10.1038/nphys244.

[144] A. Krzton-Maziopa, V. Svitlyk, E. Pomjakushina, R. Puzniak, and K. Conder, "Superconductivity in alkali metal intercalated iron selenides," *J. Phys. Condens. Matter*, vol. 28, no. 29, p. 293002, Jun. 2016, doi: 10.1088/0953-8984/28/29/293002.

[145] J. lei Zhang, L. Jiao, Y. Chen, and H. qiu Yuan, "Universal behavior of the upper critical field in iron-based superconductors," *Front. Phys.*, vol. 6, no. 4, pp. 463–473, Dec. 2011, doi: 10.1007/s11467-011-0235-7.

List of Publications and Conference Presentations

The current work is based on the results, which were either already published or are going to be as well in the following articles:

1. A. Lynnyk, R. Puzniak, L. Shi, J. Zhao, and C. Jin, „Superconducting State Properties of $CuBa_2Ca_3Cu_4O_{10+\delta}$," *Materials*, vol. 16, no. 14, p. 5111, Jul. 2023, doi: 10.3390/ma16145111.

2. A. Lynnyk, E. Pesko, A. Krzton-Maziopa, and R. Puzniak, „Upper critical field in FeSeS iron chalcogenides intercalated with lithium and ethylenediamine," 2023, (in preparation).

The publications, which fall out of the direct scope of the thesis:

3. Adam Pacewicz, Jerzy Krupka, Jan H. Mikkelsen, Artem Lynnyk, Bartlomiej Salski, „Accurate measurements of the ferromagnetic resonance linewidth of single crystal BaM hexaferrite spheres employing magnetic plasmon resonance theory", *J. Magn. Magn. Mater.* 580, 170902 (2023); doi: 10.1016/j.jmmm.2023.170902.

4. Md Shahin Alam, Amar Fakhredine, Mujeeb Ahmad, P. K. Tanwar, Hung-Yu Yang, Fazel Tafti, Giuseppe Cuono, Rajibul Islam, Bahadur Singh, Artem Lynnyk, Carmine Autieri, and Marcin Matusiak, „Sign change of anomalous Hall effect and anomalous Nernst effect in the Weyl semimetal CeAlSi", *Phys. Rev. B* 107, 085102 (2023); doi: 10.1103/PhysRevB.107.085102.

5. Leszek Gładczuk, Łukasz Gładczuk, Piotr Dłuzewski, Pavlo Aleshkevych, Artem Lynnyk, Gerrit van der Laan, Thorsten Hesjedal, „Cryogenic Temperature Growth of Sn Thin Films on Ferromagnetic Co(0001)", *Adv. Mater. Interfaces* 9, 2201452 (2022); doi: 10.1002/admi.202201452.

6. Z. Kurant, S. K. Jena, R. Gieniusz, U. Guzowska, M. Kisielewski, P. Mazalski, I. Sveklo, A. Pietruczik, A. Lynnyk, A. Wawro, A. Maziewski, „Magnetic ordering in epitaxial ultrathin Pt/W/Co/Pt layers", *J. Magn. Magn. Mater.* 558, 169485 (2022); doi: 10.1016/j.jmmm.2022.169485.

7. A. Nabiałek, O. Chumak, A. Lynnyk, J. Z. Domagała, A. Pacewicz, B. Salski, J. Krupka, T. Yamamoto, T. Seki, K. Takanashi, L. T. Baczewski, and H. Szymczak, „Anisotropy of magnetoelastic properties in epitaxial $Co_2Fe_xMn_{1-x}Si$ Heusler alloy thin films", *Phys. Rev. B* 106, 054406 (2022); doi: 10.1103/PhysRevB.106.054406.

8. A.S. Wadge, G. Grabecki, C. Autieri, B. J. Kowalski, P. Iwanowski, G. Cuono, M F Islam, C M Canali, K. Dybko, A. Hruban, A. Łusakowski, T. Wojciechowski, R. Diduszko, A. Lynnyk, N. Olszowska, M. Rosmus, J. Kołodziej and A. Wiśniewski, „Electronic properties of $TaAs_2$ topological semimetal investigated by transport and ARPES", *J. Phys.: Condens. Matter* 34, 125601 (2022);
doi: 10.1088/1361-648X/ac43fe.

9. E. Pęśko, A. Lynnyk, A. Zalewska, S. Kuś, R. Puźniak, A. Krztoń-Maziopa, „Electrochemical intercalation of alkali metal – Lewis bases adducts into layered structure of iron chalcogenides", *J. Solid State Chem.* 310, 123024 (2022);
doi: 10.1016/j.jssc.2022.123024.

10. J. Gosk, R. Puźniak and A. Lynnyk, „Magnetic Properties of Heavy Ion Implanted Monocrystalline ZnO", *Acta Physica Polonica A* 141, 2 (2022);
doi: 10.12693/APhysPolA.141.123.

11. O. M. Chumak, A. Pacewicz, A. Lynnyk, B. Salski, T. Yamamoto, T. Seki, J. Z. Domagala, H. Głowiński, K. Takanashi, L. T. Baczewski, H. Szymczak, and A. Nabiałek, „Magnetoelastic interactions and magnetic damping in $Co_2Fe_{0.4}Mn_{0.6}Si$ and $Co_2FeGa_{0.5}Ge_{0.5}$ Heusler alloys thin films for spintronic applications", *Sci. Rep.* 11, 7608 (2021);
doi: 10.1038/s41598-021-87205-y.

12. Sukanta Kumar Jena, Rajibul Islam, Ewelina Milińska, Marcin M. Jakubowski, Roman Minikayev, Sabina Lewińska, Artem Lynnyk, Aleksiej Pietruczik, Paweł Aleszkiewicz, Carmine Autieri, and Andrzej Wawro, „Interfacial Dzyaloshinskii–Moriya interaction in the epitaxial W/Co/Pt multilayers", *Nanoscale* 13, 7685 (2021);
doi: 10.1039/D0NR08594D.

13. A.N. Bludov, Yu.O. Savina, V.A. Pashchenko, S.L. Gnatchenko, T. Zajarniuk, A. Lynnyk, M.U. Gutowska, A. Szewczyk, I.V. Kolodiy, V.V. Mal'tsev, N.N. Kuzmin, N.I. Leonyuk, „Magnetic properties of $DyCr_3(BO_3)_4$"; *Low Temp. Phys.* 46, 697 (2020);
doi: 10.1063/10.0001367.

14. A. Bludov, Yu. Savina, M. Kobets, V. Khrustalyov, V. Savitsky, S. Gnatchenko, T. Zajarniuk, A. Lynnyk, M.U. Gutowska, A. Szewczyk, N. Kuzmin, V. Mal'tsev, N. Leonyuk, „Features of magnetic and magnetoelectric properties, H-T phase diagram of $GdCr_3(BO_3)_4$", *J. Magn. Magn. Mater.* 512, 167010 (2020);
doi: 10.1016/j.jmmm.2020.167010.

15. Asma Wederni, Mihail Ipatov, Eloi Pineda, Joan-Josep Suńol, Lluisa Escoda, Julián Maria González, Safa Alleg, Mohamed Khitouni, Ryszard Żuberek, Oleksandr Chumak, Adam Nabiałek, Artem Lynnyk, „Magnetic properties, martensitic and magnetostructural transformations of ferromagnetic Ni–Mn–Sn–Cu shape memory alloys", *Appl. Phys. A* 126, 320 (2020);
doi: 10.1007/s00339-020-03489-3.

16. Wojciech R. Pudelko, Anna Krzton-Maziopa, Artem Lynnyk, Roman Puzniak, Krystyna Lawniczak-Jablonska, Dariusz J. Gawryluk, Dorota Moszczynska, Jaroslaw Mizera, „Bismuth and oxygen valencies and superconducting state properties in $Ba_{1-x}K_xBiO_3$ superconductor", *Physica B* 591, 412226 (2020);
doi: 10.1016/j.physb.2020.412226.

Full list of publications can be found on Web of Science, ReseacherID: A-5921-2017.

Presentations at the conferences during the PhD studies:

1. „Superconducting State Properties of Intercalated $Li_x(C_2H_8N_2)(Fe_ySe_zS_{1-z})$ Systems", A. Lynnyk, A. Krzton-Maziopa, E. Pesko, and R. Puzniak, The Joint European Magnetic Symposia (JEMS) 2023, 27.08-01.09.2023, Madrid, Spain, poster presentation.

2. „Thermodynamic properties of superconducting $CuBa_2Ca_3Cu_4O_{10+\delta}$ (Cu1234) system", A. Lynnyk, R. Puzniak, C.W. Ren, J.F. Zhao, and C.Q. Jin, The European Conference Physics of Magnetism 2023 (PM'23), 26.06-30.06.2023, Poznań, Poland, poster presentation.

3. „Upper critical field in superconducting iron selenides intercalated with organic molecules", A. Lynnyk, A. Krzton-Maziopa, E. Pesko, and R. Puzniak, XIX National Conference on Superconductivity, 6.10-11.10.2019, Bronisławów, Poland, oral presentation.

4. „Superconducting properties of iron selenides FeSe(S, Te) intercalated with organic molecules", A. Lynnyk, A. Krzton-Maziopa, E. Pesko, and R. Puzniak, XI Symposium of PhD students, 28.05-30.05.2019, Serock, Poland, oral presentation.

5. „Superconducting properties of iron selenides intercalated with organic molecules", A. Lynnyk, A. Krzton-Maziopa, E. Pesko, and R. Puzniak, E-MRS Fall Meeting 2018, 17.09-20.09.2018, Warszawa, Poland, poster presentation.

6. „Upper critical field in $(Li\text{-}EDA)_y(FeSe_{0.88}S_{0.1})_x$ – superconducting selenide intercalated with organic molecules", A. Lynnyk, A. Krzton-Maziopa, E. Pesko, and R. Puzniak, The Joint European Magnetic Symposia (JEMS) 2018, 03.09-07.09.2018, Mainz, Germany, poster presentation.

7. „Superconducting properties of iron selenides FeSe intercalated with organic molecules", A. Lynnyk, R. Puzniak, X Symposium of PhD students, 28.05-30.05.2018, Białobrzegi, Poland, oral presentation.

8. „Magnetic and magnetocaloric properties of NiMnIn single crystals", A. Lynnyk, R. Szymczak, I. Radelytskyi, M. Berkowski, R. Diduszko, J. Fink-Finowicki, H. Szymczak, The European Conference Physics of Magnetism 2017 (PM'17), 26.06-30.06.2017, Poznań, Poland, poster presentation.